NANO-IN-MICRO MULTI-STAGE PARTICLES FOR PULMONARY DRUG DELIVERY

A Dissertation
Presented to
The Academic Faculty

by

Joscelyn Claraluz Mejías

In Partial Fulfillment
of the Requirements for the Degree
Doctorate of Philosophy in the
Wallace H. Coulter Department of Biomedical Engineering

Georgia Institute of Technology and Emory University
August 2019

Thesis Errata Sheet

Author Joscelyn C Mejias

Primary Dept. Biomedical Engineering

Degree PhD **Graduation date** August 2019

Thesis title

Nano-in-Micro Multi-Stage Particles for Pulmonary Delivery

Brief description of errata sheet

Figure 21 B-D data points have corrected color-coding to match the legend.

Page 65 nanoparticle ex/em has been corrected

Number of pages 3 (15 maximum, including this page)

Author: I request that the attached errata sheet be added to my thesis. I have attached two copies prepared as prescribed by the current *Specifications for Thesis Preparation*.

Signature of author [redacted] Date 11/13/2019

Thesis Advisor or **Dept. Chair**: I approve the attached errata sheet and recommend its addition to the student's thesis.

Signature _____ Date _____

Name _____ Thesis supervisor/Dept. Chair

VP for Graduate Education/Faculty Affairs: I approve the attached errata sheet and direct the Institute Archives to insert it into all copies of the student's thesis held by the Georgia Tech Libraries, both print and electronic.

Signature _____ Date 8/31/2020

Name Tatianna M. Richardson

The following is a correction for page 60: Figure 21 B-D color coding is corrected to match the legend.

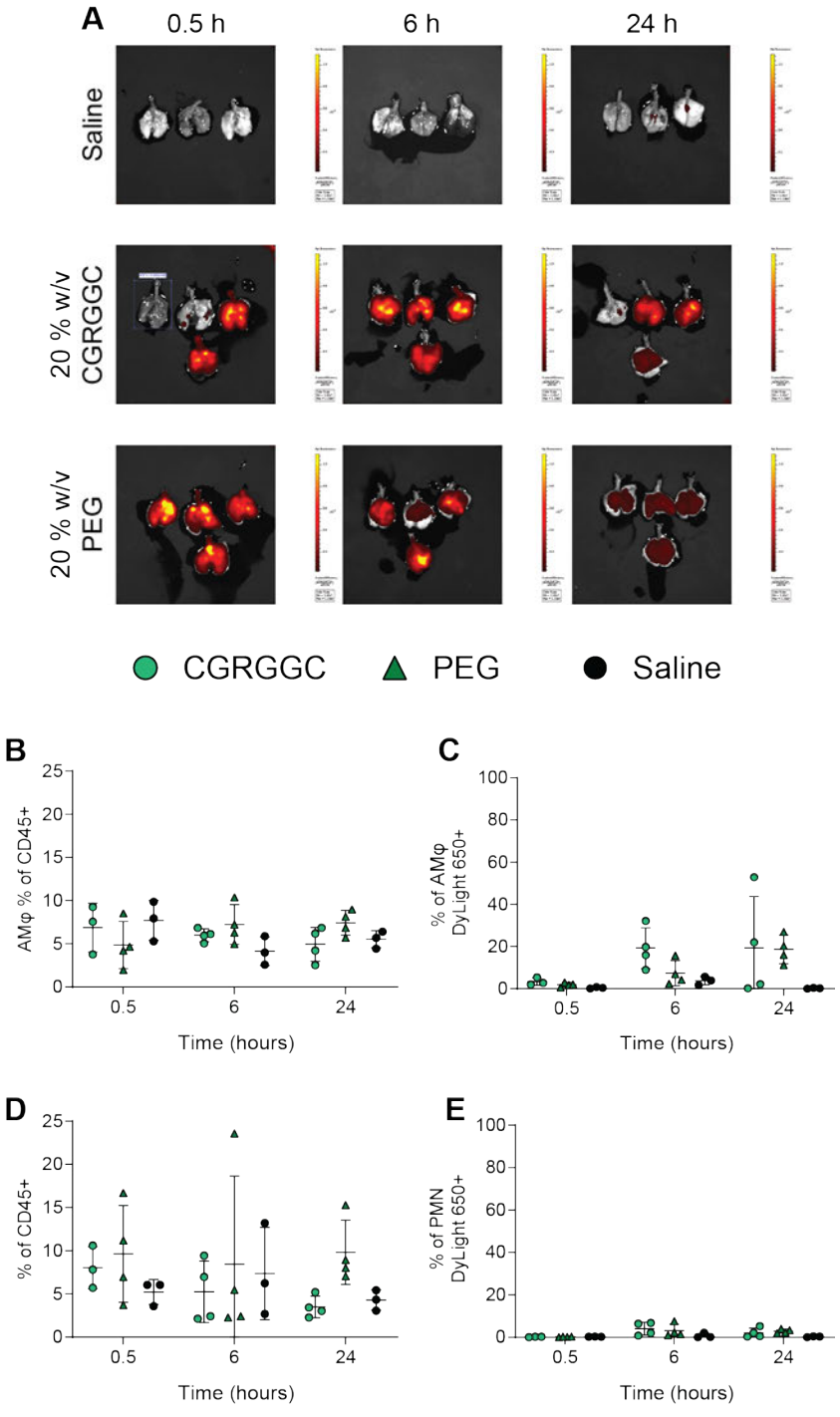

The following correction is to line 23 of page 65

Using microgels labeled with a near IR dye, DyLight 650, loaded with representative Blue (350/440) 100 nm Fluorosphere nanoparticles…

NANO-IN-MICRO MULTI-STAGE PARTICLES FOR PULMONARY DRUG DELIVERY

Approved by:

Dr. Krishnendu Roy, Advisor
Department of Biomedical Engineering
Georgia Institute of Technology & Emory University

Dr. Andrés J. García
School of Mechanical Engineering
Georgia Institute of Technology

Dr. Manu O. Platt
Department of Biomedical Engineering
Georgia Institute of Technology & Emory University

Dr. Ravi Kane
School of Chemical and Biomolecular Engineering
Georgia Institute of Technology

Dr. Rabindra Tirouvanziam
Department of Pediatrics
Emory University

Date Approved: May 08, 2019

For my family

ACKNOWLEDGEMENTS

There are many people without whom this thesis would not have been possible. First, Dr. Krish Roy for his years of guidance, directing my work, and mentoring me throughout my graduate career. To the members of the Roy Lab, especially Kirsten, Ingrid, and Michael who for the past six years have given countless ideas, help in lab, and reminders for me to write. Of course, the undergraduates whom I have had the pleasure of mentoring: Emily Chang, David Frey, Angela Jimenez, Blake Lash, Olivia Liseth, and Meghan Vierhilig. The many BME and BioE students, especially Linda Kippner, Marissa Ruehle, and Daryll Vanover. In addition, I would like to thank the EBB, Petit Institute, and Marcus Center Staff, in particular, Carol Mills, Carla Zachery, Andrea Soyland, Dr. Carolyn Yeago, Dr. Aaron Lifland, Sommer Durham, and Laura Paige. Finally, I would like to thank my family for their unconditional support and encouragement without which I could not have completed this work.

TABLE OF CONTENTS

ACKNOWLEDGEMENTS **iv**
LIST OF TABLES **vii**
LIST OF FIGURES **viii**
LIST OF SYMBOLS AND ABBREVIATIONS **x**
SUMMARY **xii**
CHAPTER 1. Introduction **1**
1.1 Overview **1**
1.2 Hypothesis **2**
1.3 Specific Aims **2**
1.3.1 Aim 1: Nano-in-Micro in vitro Characterization 2
1.3.2 Aim 2: Nano-in-Micro in vivo Characterization 3
1.3.3 Aim 3: Development of a vascularized lung-on-a-chip 4
1.4 Outline **4**
CHAPTER 2. Background **6**
2.1.1 Treating Pulmonary Disorders 6
2.1.2 Design Challenges in Pulmonary Drug Delivery 7
2.1.3 Polymers and Hydrogels 11
2.1.4 Current Models of Pulmonary Disease 12
2.1.5 Previous Work: Chitosan NP to Bypass Pulmonary Mucosa 14
CHAPTER 3. Aim 1: Nano-in-Micro *in vitro* Characterization **27**
3.1 Methods **29**
3.1.1 MADE Nano-in-Microgel Fabrication 29
3.1.2 Microscopy and Analysis 30
3.1.3 Rheometry 30
3.1.4 In-vitro Degradation 30
3.1.5 Pore Size Calculation 31
3.1.6 Macrophage Uptake Study 32
3.1.7 PLGA Nanoparticle Fabrication 32
3.1.8 PLGA Nano-in-Micro Fabrication 33
3.1.9 PMN in vitro Transmigration 33
3.1.10 Statistical Analysis 34
3.2 Results and Discussion **34**
3.2.1 Nano-in-Microgels for Aerodynamic and Geometric Size 34
3.2.2 Greater Than 95% of Microgels Degrade Within 30 Minutes in vitro 38
3.2.3 20-50% w/v Bulk Hydrogels are Relatively Soft 41
3.2.4 Increased Polymer Concentration Slows RAW 264.7 Phagocytosis 41
3.2.5 Therapeutic Loading into PLGA Nanoparticles 42
3.2.6 PLGA Loading into Nano-in-Micro 43
3.3 Conclusions **47**
CHAPTER 4. Aim 2: Nano-in-micro *in vivo* Characterization **49**
4.1 Methods **51**
4.1.1 Ethical Statement 51
4.1.2 Pulmonary Administration 51
4.1.3 LPS Induced Acute Neutrophilic Inflammation 52

4.1.4 Flow Cytometry 52
4.1.5 Extracellular vesicles (EV) analysis 55
4.1.6 ELISA 55
4.1.7 Statistical Analysis 56
Results 56
4.1.8 Microgels Begin Clearing Within 24h in Naïve Mice in vivo 56
4.1.9 Limited Phagocytosis in vivo Within 1 Hour of Administration 62
4.1.10 Nano-in-Micro in an Acute LPS-Induced Lung Injury Model 65
4.1.11 Delivering Therapeutics via Nano-in-Micro 68
4.2 Conclusion 77
CHAPTER 5. Aim 3: Microphsiologic Vascularized Lung-on-a-chip 78
5.1 Methods 79
5.1.1 Individual Microphysiologic Device Fabrication 79
5.1.2 96-well Plate Microphysiologic Device Fabrication 83
5.1.3 Cell Culture and Device Seeding 84
5.1.4 Fibroblast Screening 85
5.1.5 Fibrin-Collagen-PEG Hydrogels 85
5.1.6 Perfusion 86
5.1.7 Immunofluorescent Staining 86
5.1.8 Confocal Microscopy 87
5.1.9 Statistical Analysis 87
5.2 Results 88
5.2.1 Microphysiologic Device Overview 88
5.2.2 Fibroblast Screening 90
5.2.3 Fibrin/Collagen Hydrogels 92
5.2.4 Fibrin/Collagen/PEG Hydrogels for Vitrified Collagen Devices 94
5.2.5 0.4 µm PETE Fibrosis Model 97
5.2.6 0.4 µm PETE Devices Treated with Pirfenidone 100
5.3 Conclusions 104
CHAPTER 6. Conclusions and Future Work 106
6.1.1 Nano-in-Micro System 106
6.1.2 Vascularized Lung-on-a-Chip 108
REFERENCES 114

LIST OF TABLES

Table 1: Chitosan Nanoparticle Characterization 19
Table 2: 208kDa Chitosan Nanoparticle Size 25
Table 3: 100 nm Blue Fluosphere Encapsulation in Microgels 37
Table 4: Calculated Aerodynamic Diameters 38
Table 5: Theoretical Pore Size 40
Table 6: Antibodies Used for Microphysiologic Device Staining 87
Table 7: Fibroblast Lot Summary Information 90
Table 8: Fibrin/Collagen/Peg Hydrogel Formulations Tested 95

LIST OF FIGURES

Figure 1: Schematic Overview of Aims 5
Figure 2: Lung Schematic 7
Figure 3: Chitosan Nanoparticle SEM Images 19
Figure 4: Chitosan Nanoparticle Uptake by NuLi-1 in Liquid Culture 20
Figure 5: Chitosan Nanoparticle Uptake by hSAECs and CuFi-1 in Liquid Culture 21
Figure 6: Chitosan Nanoparticle Uptake in Air-Liquid-Interface Cultures 22
Figure 7: Chitosan nanoparticle formulation track velocity in CF ASN 24
Figure 8: 208 kDa Chitosan Nanoparticle Formulation Delivery 25
Figure 9: Nano-in-Micro Representative Schematic and Images 35
Figure 10: Flow Cytometry Characterization of Nano-in-Micro 36
Figure 11: Trypsin- and Elastase-Responsive Microgel Size Distribution 38
Figure 12: Trypsin- and Elastase-Responsive Microgel Proteolytic Degradation 40
Figure 13: Storage and Loss Moduli for Trypsin- and Elastase- Responsive gels 41
Figure 14: RAW 264.7 Macrophage Microgel Uptake 42
Figure 15: PLGA Nano-in-Micro 45
Figure 16: Elastase-Responsive Degradation and PMN Uptake 47
Figure 17: *in vivo* LSRFortessa Gating Schematic 54
Figure 18: PMN and Macrophage Flow Cytometry Gating Scheme 55
Figure 19: Microgel Deposition in naïve Mouse Lungs 57
Figure 20: 20% w/v Trypsin- and PEG- Microgel Clearance in Naïve Mice 59
Figure 21: IVIS and Flow for 20% w/v CGRGGC and PEG Nano-in-Micro 60
Figure 22: 20, 30% w/v Trypsin-Responsive Microgel Clearance in Naïve Mice 62
Figure 23: Naïve Balb/c and C57/BL6 Uptake of Nano-in-Micro Particles 64
Figure 24: Fluorescent Nano-in-Micro in an Acute Neutrophilic Inflammation Model 67
Figure 25: Nex20 and TIIA Nano-in-Micro PMN counts and DiR MFI 70
Figure 26: Bone Marrow PMN SiglecF and CD11b Expression 71
Figure 27: Nex20, TIIA Nano-in-Micro BAL and Lysate PMN Phenotype Modulation 73
Figure 28: MPO Tissue Staining 74
Figure 29: Nex20 Nano-in-Micro Cytokine Analysis 76

Figure 30: Vasculature Design Schematic 80
Figure 31: Single Device Fabrication Schematics 80
Figure 32: Airway-Media Reservoir Fabrication Methods 82
Figure 33: 96-well Plate Microphysiologic Device Fabrication 84
Figure 34: Microphysiologic Device Layout Schematics 89
Figure 35: Device Staining and Cross Section 89
Figure 36: Fibroblast Lot Effects on HUVEC Vasculogenesis and Perfusion 91
Figure 37: Fibroblast Lot Effects on Microphysiologic Lung-on-a-Chip Vasculature 92
Figure 38: Vitrified Collagen Device Fibrin/Collagen Hydrogel Failure 93
Figure 39: PETE Device Fibrin/Collagen Hydrogels 94
Figure 40: Fibrin/Collagen/PEG Vitrified Collagen Microvascularized Lung-on-a-Chip 97
Figure 41: NHLF and iPF Device Pro-Collagen I and α-SMA Staining 99
Figure 42: Pirfenidone Treated NHLF and iPF Microphysiologic Devices 101
Figure 43: TGFβ-1 and Pirfenidone Treated NHLF and iPF Devices 103
Figure 44: α-SMA Staining and Quantification 104

LIST OF SYMBOLS AND ABBREVIATIONS

α-SMA	Alpha Smooth Muscle Actin
ALI	Air Liquid Interface
AMφ	Alveolar Macrophage
Ang 1	Angiopoietin 1
APTES	(3-Aminopropyl)triethoxysilane
CF	Cystic Fibrosis
CFTR	Cystic Fibrosis Transmembrane Receptor
CGAAPVRGGGGC	Neutrophil elastase-responsive peptide sequence
CGRGGC	Trypsin-responsive peptide sequence
COPD	Chronic Obstructive Pulmonary Disorder
CuFi-1	Cystic Fibrosis University of Iowa
Da	Aerodynamic Diameter
DAPI	4’,6-diamidino-2-phenylindole
Dg	Geometric Diameter
DiR	Lipophilic carbocyanine $DiOC_{18}(7)$
HNE	Human Neutrophil Elastase
hSAECs	Primary Human Small Airway Epithelial Cells
HUVECs	Primary Pooled Human Umbilical Vein Endothelial Cells
IAA	Imidazole Acetic Acid
iPF	Idiopathic Pulmonary Fibrosis
LPS	Lipopolysaccharide
LTB4	Leukotriene B4
MADE	Michael Addition During water-in-oil Emulsion
Mal	Maleimide
MPO	Myeloperoxidase
MSCs	Primary Human Mesenchymal Stem Cells
MSD	Mean Squared Displacement
Mφ	Macrophage
Nex20	Neutrophil Exocytosis Inhibitor 20 (Nexinhib20)

NHBEs	Primary Human Bronchial Epithelial Cells
NHLFs	Primary Human Normal Lung Fibroblasts
NuLi-1	Normal Lung University of Iowa
PDMS	Polydimethyl siloxane
PEG	Poly(ethylene glycol)
PETE	Polyester Track Etched
PGP	N-acetyl-proline-glycine-proline
PLGA	Poly(lactic-co-glycolic acid)
PMN	Polymorphonuclear neutrophil
PVA	Polyvinyl alcohol
SG	Succinimidyl Glutarate
SVA	Succinimidyl Valerate
TEER	Trans Epithelial Electrochemical Resistance
TGFβ-1	Transforming Growth Factor Beta 1
TPP	Tri-polyphosphate
VEGF	Vascular Endothelial Growth Factor

SUMMARY

Pulmonary drug delivery is a non-invasive method for targeted delivery of therapeutics for the treatment of respiratory diseases such as asthma, idiopathic pulmonary fibrosis, or cystic fibrosis. Although the lung appears to be an "easy" target for site-specific delivery, there are several physiologic barriers hindering its effectiveness. For particle deposition in respiratory airways, the aerodynamic diameter of particles should fall between 0.5-5 μm, however, alveolar macrophages rapidly clear particles within this geometric range. Additionally, nano-scale particles are required for efficient transport through the pulmonary mucosa and to facilitate efficient endocytosis for intracellularly targeting therapeutics. These design parameters suggest a two-stage system is necessary for efficient therapeutic delivery; a microparticle for aerodynamic properties and a nanoparticle for drug delivery.

A nanoparticle-inside-microgel multi-stage formulation could provide efficient, intracellular delivery of nanoparticles to target cells of interest. The microgel carriers are designed for (a) protease-triggered release of drug loaded nanoparticles, (b) avoiding rapid clearance by alveolar macrophages, and (c) appropriate aerodynamic properties, while the nanoparticles are designed to (a) carry small hydrophobic molecules. The overall objective is to test this delivery system by investigating (i) how the microgels and nanoparticles interact with the phagocytic immune cells *in vitro* (Aim 1) and *in vivo* (Aim 2) and (ii) how we can recapitulate the vascular pulmonary environment to study these interactions in an *in vitro* setting (Aim 3).

CHAPTER 1. INTRODUCTION

1.1 Overview

Asthma, chronic obstructive pulmonary disorder (COPD), and cystic fibrosis (CF) are chronic inflammatory diseases characterized by an influx of innate immune cells to the lungs, including macrophages [1–3], neutrophils [3–5], and eosinophils [2,3,6,7]. These cells impose a heavy enzymatic burden through proteases such as matrix metalloproteinases and elastase that ultimately promote significant tissue damage. Pulmonary delivery is a potentially non-invasive administration route for treating these diseases; however, the anatomy and physiology of the lung present several design challenges for achieving efficient and effective drug delivery. Nanoparticles can inherently provide protection for encapsulated biologic therapeutics (proteins, RNAs) from high levels of exogenous proteases present in lung diseases, but they must be smaller than 300 nm to provide efficient cellular endocytosis [8–11] and transport across the mucosal barrier to target epithelial cells [12–14]. However, nanoparticles alone cannot efficiently aerosolize and deposit within the lung via inhalation; particles with aerodynamic diameters less than 1 μm are predominantly exhaled, and greater than 5 μm are impacted in the mouth or throat [15]. While those between 1-5 μm are deposited more efficiently into the deep lung, alveolar macrophages rapidly phagocytose particles with geometric diameters within the 1-5 μm range [16,17], making efficient delivery difficult.

Additionally, pre-screening therapies for diseases such as idiopathic pulmonary fibrosis (iPF) and CF are further complicated by the lack of accessible representative animal models. iPF's cause and pathogenesis are poorly understood, but the hallmark fibroblastic foci and irreversible scarring lead to severe pulmonary damage [18]. Mouse

models often used to “mimic” iPF use small molecules (e.g. bleomycin) to induced lung damage and scarring rather than underlying physiology [19]. CF is a relatively well understood etiology caused by mutations to the cystic fibrosis transmembrane conductance regulator (CFTR). However, CFTR knockout and mutant mice lack the severe human lung pathology and do not replicate the lower airway extracellular barriers present in human CF diseases [20,21]—preventing the study of particle or drug transport in relevant models.

Thus, this thesis addresses pulmonary delivery with a multi-stage particle nanoparticle-inside-microgel and develops an *in vitro* human microphysiologic model.

1.2 Hypothesis

The central hypothesis is that a nanoparticle-inside-microgel (Nano-in-Micro) multi-stage formulation could provide efficient, intracellular delivery of nanoparticles to target cells of interest. The overall objective is to test this delivery system by investigating (i) how the microgels and nanoparticles interact with the phagocytic immune cells *in vitro* (Aim 1) and *in vivo* (Aim 2) and (ii) how we can recapitulate the vascular pulmonary environment to study these interactions in an *in vitro* setting (Aim 3).

1.3 Specific Aims

1.3.1 Aim 1: Nano-in-Micro in vitro Characterization

The overall goal of this aim was to characterize the multi-stage delivery system *in vitro.* A maleimide-thiol based Michael Addition During water-in-oil Emulsion (MADE) method was used to fabricate the Nano-in-Microgels. The working hypothesis was that the size and elastic properties of the microgel could help reduce the rapid clearance by macrophages to prolong microgel presence in the lung from minutes to hours.

A. Nano-in-Micro particles were fabricated with two peptide crosslinkers, a CGRGGC (trypsin-responsive) or a CGAAPVRGGGGC (elastase-responsive) peptide were incorporated into the microgels; the initial macromer concentration (20-50% w/v) was varied to determine the effects on size distribution, degradation rate, and *in vitro* macrophage phagocytosis.

B. Nanoparticles for targeting neutrophilic (PMN) inflammation were fabricated and characterized. Fibrosis Relevant drugs (R)-Roscovitine, Nexinhib-20, and Tanshinone IIA were incorporated into PLGA nanoparticles and loaded into elastase-responsive Nano-in-Microgels. PLGA encapsulation, microgel degradation, and *in vitro* PMN uptake were measured.

1.3.2 Aim 2: Nano-in-Micro in vivo Characterization

The overall goal of this aim was to characterize the multi-stage delivery system *in vivo.* Naïve mice were used to characterize the impact of the microgel formulation on phagocytosis and clearance, while an acute neutrophilic inflammation model was used to test the efficacy of the system in targeting neutrophils.

A. Nano-in-Micro trypsin- and elastase- responsive particles were delivered to naïve mice to characterize the biodistribution, phagocytosis, and clearance.

B. Nano-in-Micro loaded with fluorescent reporter nanoparticles and therapeutic PLGA nanoparticles were used in an LPS induced acute neutrophilic inflammation mouse model to determine whether the system could target neutrophilic inflammation.

1.3.3 Aim 3: Development of a vascularized lung-on-a-chip

The purpose of this aim was to develop a microphysiologic device that replicates three key features of the respiratory airways (1) primary human lung epithelial cells at an air-liquid interface (2) interstitial space for healthy or diseased fibroblasts and (3) a network of perfusable blood vessels to recapitulate both healthy and fibrotic pulmonary environments.

1.4 Outline

This work focuses on the design of protease-responsive biomaterials for site specific delivery to lung diseases. Background information on pulmonary drug delivery design challenges, biomaterials used throughout this thesis, and current pulmonary testing models can be found in Chapter 2. In Chapter 3 we investigate how perturbations of the starting polymer concentration during the fabrication of both a trypsin- and elastase-responsive Nano-in-Micro system effects the size and *in vitro* macrophage phagocytosis. Additionally, we encapsulated small molecule drugs that appear promising for fibrosis into water-soluble PLGA nanoparticles. We then encapsulated these drug-loaded PLGA nanoparticles into the elastase-responsive microgel formulation. In Chapter 4, to understand how the Nano-in-Micro system interacts with the innate immune phagocytes, we investigated the biodistribution, phagocytosis and clearance of the microgels in naïve mice. We then investigated the use of fluorescent and drug-loaded elastase-responsive Nano-in-Micro particles to deliver therapeutic cargo to neutrophils in an LPS acute neutrophilic inflammation model. While there are numerous mouse models that use small molecules to create acute and chronic pulmonary inflammation, due to the poor ability of mouse models to mimic human pulmonary diseases, in Chapter 5, we designed and

fabricated a microphysiologic device to incorporate microvasculature surrounded by healthy or diseased fibroblasts underneath a thin film membrane that supported lung epithelial cells and their differentiation at an air-liquid interface. The schematic overview of these aims is detailed in Figure 1.

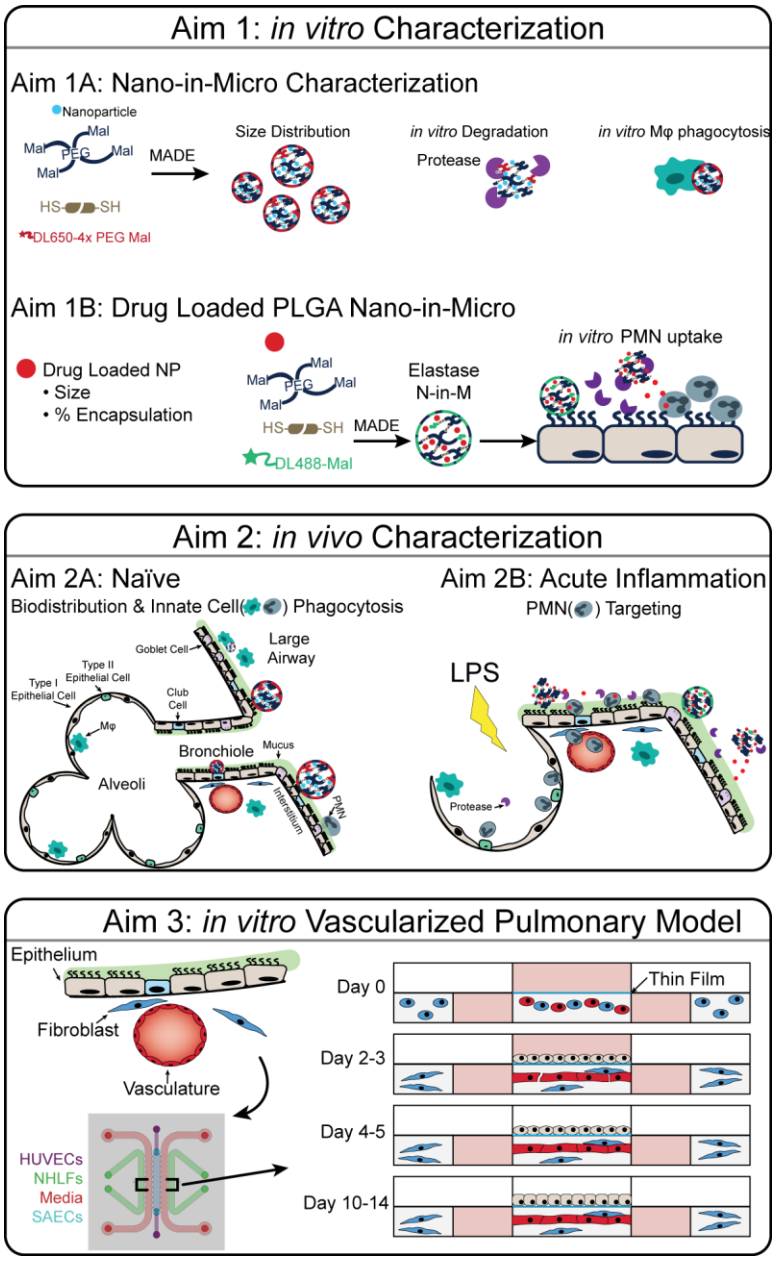

Figure 1: Schematic Overview of Aims

CHAPTER 2. BACKGROUND

2.1.1 Treating Pulmonary Disorders

While traditional systemic drug delivery through oral or injection routes is convenient and widely used, it is inefficient and the optimal therapeutic dose is often missed. Too low of a concentration renders the therapy ineffective, and too high of a concentration can lead to off-target toxicity. Site-specific delivery can reduce the off-target toxicity of therapeutics while also delivering a relevant dose to the specified tissue. Noncommunicable diseases are responsible for 70% of deaths worldwide, with chronic respiratory diseases accounting for the third highest global mortality rate [22]. Inhalation therapy has the potential to be the optimal mode of delivery for respiratory diseases such as asthma, chronic obstructive pulmonary disorder (COPD), idiopathic pulmonary fibrosis (iPF), and cystic fibrosis (CF). Inhaled therapeutics such as corticosteroids are common and have proven beneficial in controlling and maintenance of asthma and COPD [23–29]. However many pulmonary therapeutics are still delivered orally; iPF has two available therapeutics, Pirfenidone and Nintedanib, that are delivered orally and while tolerable, cause adverse side effects such as nausea, abdominal discomfort, and fatigue [29–36]. Pulmonary delivery is a potentially non-invasive administration route for both systemic delivery of therapeutics and site-specific targeting therapies. Although lung delivery appears to be an easy target for non-invasive administration of both systemic delivery of therapeutics and site-specific targeting therapies, the lung has several physiologic barriers to consider for particle design.

2.1.2 Design Challenges in Pulmonary Drug Delivery

The lung branches from large to small conducting airways down to smaller respiratory bronchioles and alveoli. The larger airways are characterized by ciliated pseudostratified columnar epithelium and goblet cells which, as the airways branch, transition into a simple ciliated cuboidal epithelium with club cells and eventually branch into squamous epithelium of the alveoli which are a mixture of type I and II epithelium and an abundance of alveolar macrophages (schematic in Figure 2). The high surface area of the respiratory airways and thin barrier that allows for efficient gas exchange between the respiratory epithelium and vascular endothelium also allows for efficient drug absorption into systemic circulation. For diseases such as idiopathic pulmonary fibrosis (iPF), chronic obstructive pulmonary disorder (COPD), asthma, tuberculosis and lung cancers, pulmonary delivery offers site-specific targeting of drugs while lowering off-target therapeutic side effects.

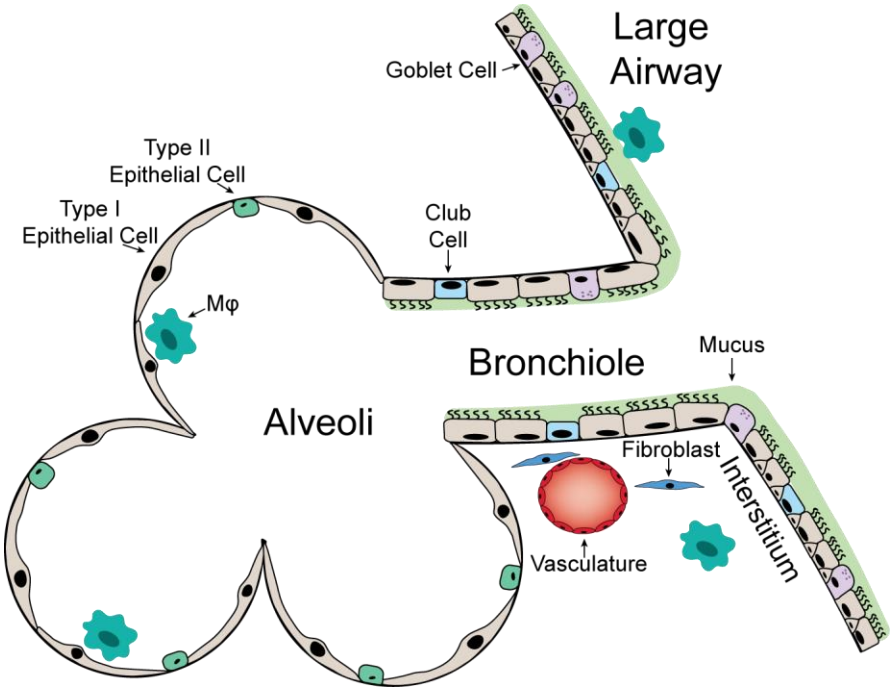

Figure 2: Lung Schematic

2.1.2.1 Pulmonary Particle Deposition

The anatomy and physiology of the lung present several design challenges for achieving efficient and effective drug delivery. The deposition of particles in the lungs is primarily dependent on particle size and shape [37–39]. Considering size, the mechanism for particle deposition is inertial impaction, sedimentation, and diffusion. For small particles (< 0.5 μm), diffusion is dependent on Brownian motion and can be described by Stokes-Einstein, while sedimentation relies on gravity and time for particles to settle and can be influenced by breath-holding. Larger particles often deposit by inertial impaction as the particle's momentum allows the particle to maintain trajectory as air flow changes directions as the airways branch. Generally, the anatomical structure of the lung dictates particles with an aerodynamic diameter less than 0.5 μm will be exhaled, between 0.5-5 μm will be deposited in respiratory airways, and greater than 5 μm will be impacted in the mouth/throat [37–42].

2.1.2.2 Pulmonary Mucosa and Innate Immunity

Additionally, the lung has several barriers once particles deposit. Pulmonary secretions of mucus and surfactants are necessary for homeostasis, vital in trapping and removing foreign particulate through mucociliary clearance (through beating of cilia), and important in immune regulation [43–46]. The mucosa is a viscoelastic material described as a "gel-on-brush" model where it is compartmentalized into two distinct regions: a more viscous layer composed of secreted mucins on top of the less viscous periciliary layer which contains membrane-tethered mucins [47]. Goblet cells and sub mucosal glands in the upper airways secrete mucins such as MUC5AC and MUC5B. The dysregulation of these mucins has been shown to be important in asthma, iPF, and CF [48–51]. Tethered

mucins such as MUC1, MUC4, and MUC16, are a direct host barrier to the epithelial surface, play a role in intracellular signal transduction and have been shown to modulate the immune response to pathogens [52,53]. Club cells secrete additional proteins into the mucosa such as glycosaminoglycans and uteroglobin, a potent immunomodulator [54–57]. In diseased states there is often impaired mucociliary transport, overexpression of mucin, higher viscosity mucus, increased exogenous proteases, and abnormal osmolarity [46,48,58,59]. This complex network of mucins and surfactants must be bypassed to target lung epithelial cells or interstitial fibroblasts, and nanoparticles smaller than 300 nm are needed for efficient endocytosis [5,12,60–64].

Furthermore, phagocytic innate immune cells such as dendritic cells and macrophages line the airways and are important first responders in immune surveillance. Pulmonary macrophages can be subdivided into at least three distinct populations: bronchial, interstitial, and alveolar macrophages. Each population occupies different compartments of the lungs and they have different developmental pathways (fetal vs bone marrow) [65–67]. Interstitial macrophages function in tissue remodeling and maintenance, antigen presentation, influence dendritic cell function, and have differential immunomodulatory reactions than alveolar macrophages [65–70]. Tissue-resident alveolar macrophages are efficient at initiating and resolving pulmonary inflammation, communicating with alveolar epithelium, and regulating neutrophilic response [71–73]. One of the primary roles of alveolar macrophages is to phagocytose foreign particulate; while targeting of alveolar macrophages for therapeutic purposes is possible [17,74], delivery of therapeutics to other cells of interest (e.g. epithelial) is made more difficult by their phagocytic ability. This poses a difficult challenge for pulmonary delivery, as alveolar

macrophages can rapidly phagocytose particles with geometric diameters within the optimal 0.5-5 μm range aerodynamic [17,40,75,76].

2.1.2.3 Strategies for Pulmonary Delivery

These pulmonary barriers dictate that for efficient particle delivery, the particle requires an aerodynamic diameter between 0.5-5 μm and a geometric diameter greater than 6 μm. Additionally, a nano-scale size is necessary for efficient cellular endocytosis and to pass the mucosal barrier. Current strategies for addressing these conflicting design criteria for aerodynamic and geometric size include the use of porous polymers and swellable microparticles. By lowering the density of the microparticles, large porous particles provide an aerodynamic diameter between 1-5 μm and a geometric diameter greater than 6 μm, thus increasing residence time after deposition in the lungs [40,77,78]. While swellable microparticles in their relaxed, dry state provide the correct aerodynamic size for lung delivery, they swell in the humid lung environments to a size capable of avoiding rapid macrophage clearance [79–82]. However, once these microscale carriers reach the deep lung, intracellular delivery and transport across mucosal surfaces remain significant challenges.

Nano-in-Micro particles have been previously reported for intestinal [83,84] and lung delivery [79–82], and the Roy Lab has previously reported a proof-of-concept trypsin-responsive crosslinker with 60% w/v microgels for pulmonary delivery [79]. Poly(ethylene glycol) based hydrogels with protease responsive backbones have been widely used to respond and degrade to the cellular microenvironment [85–87]. Including an enzyme-responsive peptide allows the microparticles to degrade rapidly in diseased airways with high enzymatic burden and thus release encapsulated therapeutic nanoparticles. These

nanoparticles are physically entrapped in the hydrogel network allowing the nanoparticle formulations to be easily exchanged for the desired therapeutic target. Microparticles in airways with low enzymatic burden typical of heterogenous diseases, should be cleared without releasing the nanoparticles – thus lowering side effects. Here, we study the impact of reducing starting polymer concentrations for the microgel formulation to avoid rapid clearance using two different crosslinkers, trypsin-responsive (CGRGGC) and neutrophil elastase-responsive (CGAAPVRGGGGC) adapted from the Anseth Lab by incorporating cysteine groups [88]. A neutrophil elastase responsive peptide was chosen as this protease is well known to be involved in various acute and chronic pulmonary inflammatory diseases [4,89–92]. We report an improved Michael Addition During (water-in-oil) Emulsion (MADE) method, which provides faster reaction kinetics during fabrication while avoiding degradative conditions caused by factors such as UV light, high temperatures, and organic solvents that could denature biologic drugs or sensitive therapeutics.

2.1.3 Polymers and Hydrogels

Polymers are large molecules composed of repeating subunits and can be derived from natural or synthetic sources. Hydrogels are constructed from a network of crosslinked hydrophilic polymers allowing the three-dimensional network to hold large amounts of water in their swollen state—with the mass fraction of water in the hydrogel higher than the mass fraction of the polymer. Hydrogels can be fabricated with either natural or synthetic polymers. Many natural hydrogels are inherently bioactive, allowing cells to recognize and respond to the hydrogel (e.g. cellular adhesion) without additional modifications; however, they can be mechanically weak and have inconsistent batch-to-

batch variability [93,94]. Synthetic polymers offer a high degree of control over properties such as manufacturing quality control, chemical functionality, and hydrogel mechanical properties; however, they are not inherently bioactive requiring modification for cellular interactions [93–96].

Natural polymers include chitosan, collagen, and fibrinogen. Chitosan is a cationic polymer created by deacetylation of chitin, found in crustacean exoskeletons, and has been used in applications ranging from bone and cartilage repair to microparticle drug release [97–102]. Collagen and fibrin are both animal derived polymers; collagen is an abundant mammalian extracellular matrix components and fibrinogen is a blood circulating glycoprotein that is enzymatically cleaved by thrombin to spontaneously polymerize creating a fibrin network. Collagen and fibrin-based hydrogels have been used for multiple applications including vasculogenesis, chondrogenesis, therapeutic assays, and drug release [103–110].

Synthetic polymers such as polyvinyl alcohol (PVA), poly(lactic-co-glycolic acid) (PLGA), and polyethylene glycol (PEG). PVA, PLGA, and PEG have all been used for similar applications as natural polymers as well as in combination as natural/synthetic hydrogels [111–114]. PEG is a particularly useful platform as it can be modified with different functional groups allowing for a high degree of flexibility in the design and easy incorporation of biologics and biologically relevant peptides [105,115–118].

2.1.4 Current Models of Pulmonary Disease

Although site-specific drug delivery with polymeric particles to the lung may be beneficial, pre-screening effective therapeutics for pulmonary fibrosis disorders such as iPF and CF is complicated by the lack of representative *in vitro* and *in vivo* models. These

diseases cause severe lung damage that eventually leads to respiratory failure and patient death. iPF is estimated to affect 3 million people with a life expectancy of 2.5-5 years after diagnosis [33,119]. CF is a genetic disorder with approximately 30,000 people diagnosed in the US and an estimated 10 million carriers of one of 1800 different mutations to the cystic fibrosis transmembrane conductance regulator (CFTR); CF has a median age of death of 30.7 years [120].

Mouse models are often used for preclinical testing of pulmonary therapeutics. Small molecules such as lipopolysaccharide (LPS), N-acetylated proline-glycine-proline (PGP), and bleomycin are delivered directly to the mouse lungs to induce acute (LPS) or chronic (PGP) neutrophilic inflammation and fibrosis (bleomycin) [19,73,121,122]. While these models can replicate some aspects of inflammation, they do not recapitulate the underlying physiology. Although some genetic based models exist, such as CFTR knockout and mutant mice for CF, these models lack the severe human lung pathology since a compensatory mouse epithelial anion channels prevents CF knockout/mutant mice from replicating the lower airway extracellular barriers present in human CF diseases [20,21]. Ferret and piglet CF knockout models and dog, cat, donkey and horse pulmonary fibrosis resemble aspects of human disease, but these models are less accessible [19–21].

Current three-dimensional *in vitro* models for the respiratory airways include decellularized tissue scaffolds, spheroid/organoid cultures, and air-liquid interface (ALI) cultures. Lung organoids refer to self-assembling structures generated from basal epithelium. These organoid cultures are useful as medium to high throughput models for screening the effects of modulators on epithelial cells; however, they lack lung-relevant extracellular barriers and do not recapitulate all of the complex structures such as the highly

vascularized respiratory airways [58,123–129]. ALI cultures are commonly used as they replicate relevant epithelial morphology (pseudostratified, ciliary movement, mucus production, polarity, and tight junctions) and are even commercially available (Epithelix). ALI cultures have been developed to replicate the neutrophil extravasation and activation in inflammation and CF using CF patient airway supernatant [130]. Microfluidic based ALI models have been able to recapitulate the pseudostratified epithelium and monolayer endothelium or smooth muscle cells separated by a thing film polyester track etched or polydimethylsiloxane membrane; however, to recapitulate neutrophilic extravasation larger 10 μm porous membranes are used [131–134] and the microvasculature and interstitial environment are not replicated.

2.1.5 Previous Work: Chitosan NP to Bypass Pulmonary Mucosa

2.1.5.1 Introduction

Chitosan is a mucoadhesive polysaccharide. Its cationic nature allows it to be easily coupled to negatively charged payloads including nucleic acids and certain proteins. Because of its mucoadhesive properties, chitosan nanoparticles have been formulated for delivery to mucosal surfaces such as ocular, intestinal, and pulmonary [100,102,135–138]. By entrapping into the mucus, the nanoparticles are able to increase their residence time and can act as a drug depot, increasing the time available for therapeutic release and nanoparticle efficacy [136,139]. However, for intracellular epithelial targets, mucus penetrating particles may be more appropriate to efficiently bypass the mucus and be endocytosed by the epithelium [9,12,64,114]. Chitosan modified with 2-3% imidazole acetic acid (IAA) has been shown to have increased buffering capacity, higher solubility at physiologic pH, and improved nucleic acid delivery *in vitro* and *in vivo* [140,141]. Here,

we adjusted the modification protocol to increase the IAA modification of chitosan that appears to adjust the mucoadhesivity of the chitosan nanoparticles and show increased epithelial uptake of fluorescent nanoparticles in *in vitro* air-liquid interface models.

2.1.5.2 Materials and Methods

Imidazole Modification of Chitosan: Imidazole modified chitosan (Chitosan-IAA) was synthesized by utilizing sulfo-NHS/EDC chemistry to link 4-imidazole acetic acid (IAA, Sigma Aldrich) to the primary amines of 83% de-acetylated chitosan (Protasan UP-CL113, MW 83kDA, Novamatrix). Briefly, IAA was dissolved at 10 mg/mL in 0.1 M MES buffer and brought to a pH of 4.5-6. 1-Ethyl-3-(3-dimethylaminopropyl) carbodiimide (EDC, Sigma Aldrich) was added to the solution in a 5 M excess to the IAA along with sulfo-NHS (Sigma Aldrich) to a concentration of 5 mM. This is reacted for 15 minutes before being quenched with 2-mercaptoethanol. The solution pH was then raised to 7. Chitosan dissolved in PBS at 10 mg/mL was then added to this solution and allowed to react while rotating for 2 hours. The Chitosan-IAA solutions were dialyzed against 5mM HCl for 2 hours twice and DI water twice for 6-12 h, then lyophilized for 48 hours. The imidazole to chitosan ratio was adjusted to produce chitosan-IAA polymers with different levels of modification at 20 and 40%. For the 83% deacetylated chitosan, 208 kDa chitosan (Chitoceuticals GMP Compliant Chitosan, Heppe Medical Chitosan, Halle Germany) formulation, the reaction of chitosan with the IAA solution was reduced to 1 hour.

IAA Modification Characterization: In order to characterize the degree of modification of chitosan-IAA, the strong UV absorbance of IAA at 230 nm was measured. Briefly, a standard curve of IAA was created in acetate buffer and compared to known concentrations of chitosan, chitosan-IAA, and acetate buffer at 230 nm. The standard curve

was used to determine the IAA concentration in the known chitosan concentration to approximate percent modification.

Nanoparticles Fabrication: Nanoparticles were prepared by complexing chitosan with tri-poly phosphate via electrostatic interactions. Chitosan or chitosan-IAA was dissolved in acetate buffer (pH 4.5) at a concentration of 2 mg/mL. TPP was also dissolved in acetate buffer and added at a ratio of 5:1 (TPP:Chitosan) to the chitosan solution. This was vortexed in a 15 mL conical on high for 30 seconds and left rotating at room temperature for 30 minutes. The resulting particles underwent buffer exchange into PBS via centrifugation in 10K MWCO Amicon Ultra 4 centrifugal filters (AMD Millipore). Particles were resuspended in a 1M KCL solution and size and zeta were measured using a Malvern Nano ZS (Malvern Instruments) and used immediately after preparation. For fluorescently tagged particles, the particles solution was exchanged into a 0.2 M sodium bicarbonate buffer, pH 8.3, and VivoTag 645 (NEV11174, Perkin Elmer) was added to the new solution according to manufacturer's instructions. After one hour of coupling, the nanoparticles were separated from unreacted dye by either dialyzing repeatedly in HCl and DI water for 24 hours in 40K MWCO Float-A-Lyzers (Spectrum Laboratories) or by using 7k MWCO Zeba Spin Desalting Columns (Thermo Scientific). Chitosan nanoparticles were air dried on carbon tape and imaged using a Hitachi SU8230. Chitosan nanoparticle concentrations used for the experiment were the theoretical max concentration of chitosan mass resuspended in 1 mL of media/buffer.

NuLi-1 and CuFi-1 Cell Culture: A vial of NuLi-1 was gifted by the Emory University Experimental Models Core (EMC) and CuFi-1 was graciously gifted by Dr. J. Zabner (University of Iowa). For liquid culture, cell lines were expanded in BEBM

supplemented with BEGM Single Quots (Lonza) with the Single Quots' gentamycin/amphotericin B stocks substituted with 0.01% v/v gentamycin (Sigma), 0.05% v/v amphotericin B (Amresco), and 0.5% penicillin-streptomycin (Gibco). Culture surfaces were coated for 48 h to 1 week in 60 µg/mL human placental collagen IV (Sigma) before cell seeding. For ALI cultures, transwells were collagen coated, cells were seeded at 60,000 cells per 24-well transwell in DMEM-F12 (Gibco) supplemented with 5% v/v FBS (HyClone), 0.1% v/v gentamycin, 0.05% v/v amphotericin B, and 0.5% v/v penicillin-streptomycin. Media was added to both the apical and basal chambers. On day 2, media was exchanged for DMEM-F12, 2% Ultroser G (Emory University Experimental Models Core), and on day 7 the cultures were airlifted by removing the apical media. Transwells were fed every two days and the apical surface was rinsed with PBS at least once per week while trans-epithelial electrical resistance (TEER) was measured with an EVOM 2 (World Precision Instruments).

hSAEC Culture: Primary human small airway epithelial cells (hSAECs) guaranteed for differentiation were purchased from Lonza (CC-2547S, lot #0000501938). Cells were expanded in PneumaCult-Ex Plus (STEMCELL Technologies), seeded, and differentiated according to manufacturer's instructions in PneumaCult-ALI Media (STEMCELL Technologies).

Fluorescent Immunostaining: Transwells were fixed in 4% paraformaldehyde (ThermoFisher Sci), the membrane and cells were then carefully excised from the transwell and washed in 1x TBS for 5 minutes. The membrane was then blocked for 2 h at room temperature in 5% goat serum with 0.5% triton X, incubated at 4C overnight with the antibodies in 5% goat serum, washed 2x in blocking buffer then, if needed, incubated in

secondary at 37C for 1 hour and mounted between coverslips using Prolong Gold with DAPI (ThermoFisher Sci.) Antibodies used included: 1:100 dilution ZO-1-Alexa Fluor 488 (ThermoFisher Sci, clone 1A12) and 1:100 Tubulin Beta 4 (LSBio, TUBB4-clone 6C2) with 1:250 Goat anti-Mouse Alexa Fluor 647.

Microscopy: Fluorescent images were collected on a PerkinElmer UltraVIEW VoX spinning disk confocal with a Hamamatsu C9100-23b back-thinned EM-CCD or Hamamatsu FLASH 4 sCMOS version 2 and Nikon 60x NA-1.49 TIRF oil objective; SAECs were imaged with the Nikon 40X NA-1.3 oil objective and the resulting picture is an extended focus Z-stack.

Track Velocity Measurements: Images were captured on a PerkinElmer UltraVIEW VoX spinning disc confocal with a Hamamatsu C9100-23b back-thinned EM-CCD and Nikon 60x NA-1.49 TIRF oil objective at a rate of 15.07 timepoints per second for 1 minute. Data were analyzed using Volocity software (PerkinElmer); track lengths less than 5 were removed.

Statistical Analysis: Data were analyzed using GraphPad with a Shapiro-Wilk test for normality ($\alpha = 0.05$). A two-way Anova ($\alpha = 0.05$) (mixed model with variable n) with Tukey post hoc analysis was used with Chitosan nanoparticle data that passed Shapiro-Wilk. Else, Kruskal-Wallis ($\alpha = 0.05$) with Dunn's multiple comparison test (with adjusted P value) was used for data within each timepoint that failed the normality test.

2.1.5.3 Results and Discussion

Chitosan Characterization: Chitosan was modified with imidazole acetic acid (IAA) up to 20 and 40% modification by adjusting the amount of IAA added during the EDC/NHS chemistry. Higher modification than the previously reported 2-3% was

achieved by including an NHS reaction step. Nanoparticles were fabricated from unmodified chitosan, chitosan:IAA 20%, and chitosan:IAA 40% by electrostatic interactions with the small molecule tripolyphospate (TPP). Chitosan:TPP, ChitosanIAA20:TPP, or ChitosanIAA40:TPP nanoparticles were then imaged by SEM, Figure 3. Nanoparticles were found to have mean sizes between 71-85 nm and a positive Zeta potential from 10-15 mv, Table 1. The nanoparticle size suggests that these particle formulations should be able to bypass the mucosal layer.

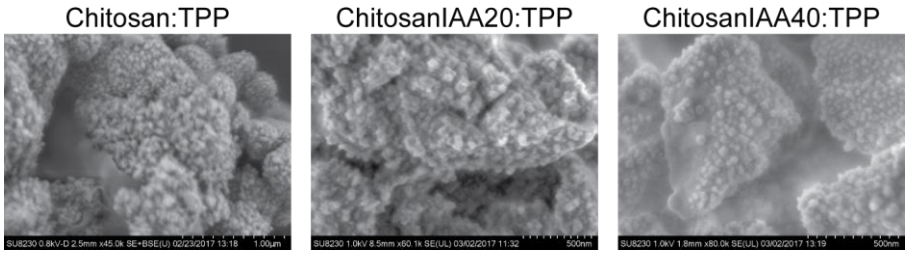

Figure 3: Chitosan Nanoparticle SEM Images Chitosan nanoparticle formulations imaged by SEM

Table 1: Chitosan Nanoparticle Characterization

	Mean ± SD (nm)	PDI ± SD	Zeta (mv)
Chitosan:TPP	74.89 ± 4.63	0.19 ± 0.02	11.83 ± 1.37
ChitosanIAA20:TPP	71.73 ± 1.39	0.20 ± 0.04	12.78 ± 2.37
ChitosanIAA40:TPP	81.55 ± 7.07	0.22 ± 0.01	13.63 ± 0.63

Chitosan Nanoparticle Uptake by Human Epithelial Cells: To determine whether these particles would be endocytosed by lung epithelial cells, standard submerged liquid cultures of NuLi-1, a cell line derived from human airway epithelial cells with a normal-non-CF genotype [142], were treated with VivoTag 645 fluorescently tagged chitosan nanoparticles at 1, 5, and 10 µg/mL and at 6, 12, and 24 hours the cells harvested and run on a flow cytometer to measure VivoTag positive cells. Gates were set using an FMO control. For all three concentrations the un-modified chitosan had rapid increase in

the percentage of cells positive for the nanoparticle dye followed by a slower increase in the percentage of cells positive for the ChitosanIAA20:TPP or ChitosanIAA40:TPP IAA modified chitosan nanoparticles, Figure 4. At 10 µg/mL all three formulations had greater than 20% increase at 6 hours; this concentration was chosen for the rest of the particle delivery experiments.

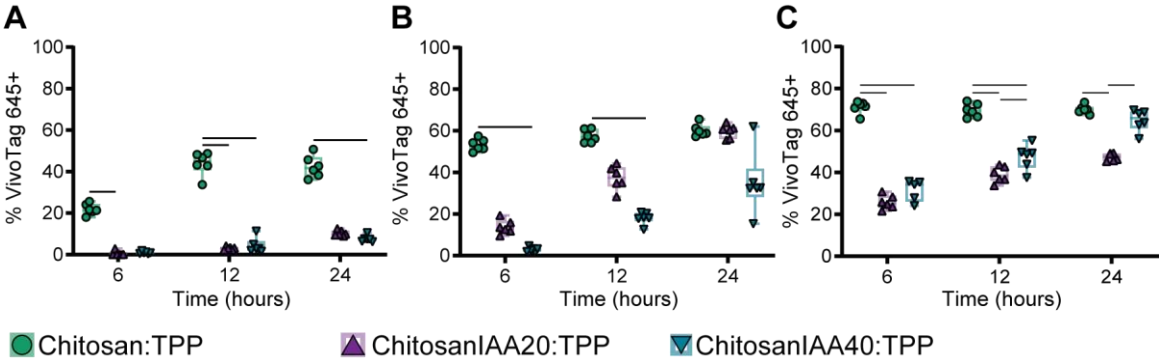

Figure 4: Chitosan Nanoparticle Uptake by NuLi-1 in Liquid Culture Dose dependent uptake in standard liquid cultures of NuLi-1 cells at (A) 1 µg/mL (B) 5 µg/mL (C) 10 µg/mL (n = 6) at 6, 12, and 24 hours. Bars indicate statistical significance ($\alpha = 0.05$)

Chitosan Nanoparticle Uptake in Air-Liquid Interface Cultures: The uptake of particles was then tested on primary human small airway epithelial cells (hSAECs) and the cystic fibrosis cell line CuFi-1. CuFi-1 is a human immortalized cell line developed from a ΔF508/ΔF508 genotype [142]. The hSAECs showed the opposite response of the NuLi-1 cells, with all 3 nanoparticle formulations greater than 20% at 6 hours and higher percentages of fluorescent cells for the IAA modified chitosan nanoparticles. These cells do not appear to endocytose the chitosan:TPP particles well, with the mean at 24 hours of 33% while the 20 and 40% IAA modified particles were at 90 and 95% respectively, Figure 5A. The CuFi-1 cells appeared impartial to any nanoparticle formulation and at 6 hours had the highest percentage of cells positive for VivoTag 645, which was over 80% for all three formulations, Figure 5B.

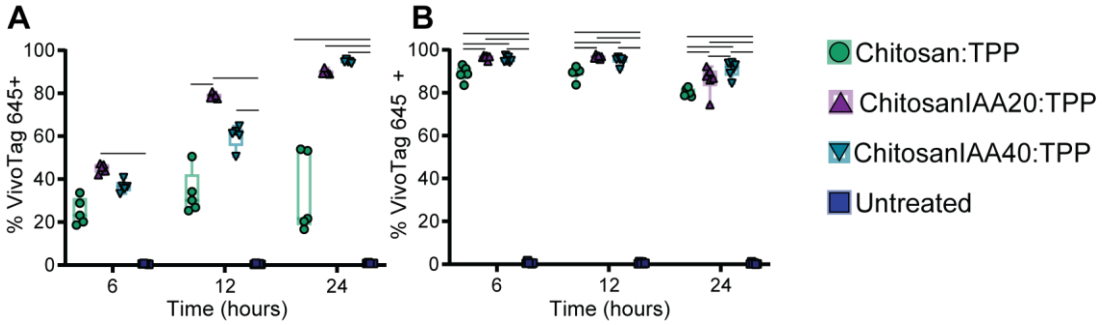

Figure 5: Chitosan Nanoparticle Uptake by hSAECs and CuFi-1 in Liquid Culture (A) hSAEC uptake of Chitosan nanoparticles (n=5) and (B) CuFi-1 uptake of particle formulations (n = 6). Bars indicate statistical significance ($\alpha = 0.05$).

Culture of epithelial cells at an air-liquid interface is a simple model of the human respiratory system that can recapitulate tight junction formation, mucus secretions, and cuboidal or columnar epithelium depending on the starting cell source. These cultures were used to understand how the nanoparticles might transport across the mucosal barrier. hSAECs, NuLi-1 and CuFi-1 were grown at an air-liquid interface for 5-6 weeks, with TEER measured weekly, then treated with VivoTag 645 tagged Chitosan:TPP, ChitosanIAA20:TPP, or ChitosanIAA40:TPP nanoparticles. hSAECs cultures were a cuboidal layer that formed tight junctions (Z01) and cilia with an adjusted TEER mean over 400 Ω*cm^2 week 5, Figure 6A-B. NuLi-1 and CuFi-1 were not expected to form cilia [142] and were only stained for tight junctions (Z01) and nuclei (DAPI). NuLi-1 formed a monolayer with mean adjusted TEER just 100 Ω*cm^2, which was lower than expected [142] but not uncommon for this cell line [143], Figure 6C-D; however, the cultures still visually produced mucus-like secretions on top of the cells. CuFi-1 formed more of a pseudostratified epithelium, with overlapping cells visible by the overlapping nuclei and tight junction formation, mean adjusted TEER 1800 Ω*cm^2, Figure 6E-F. Like the NuLi-1, CuFi-1 also produced secretions visible when inspecting the transwells.

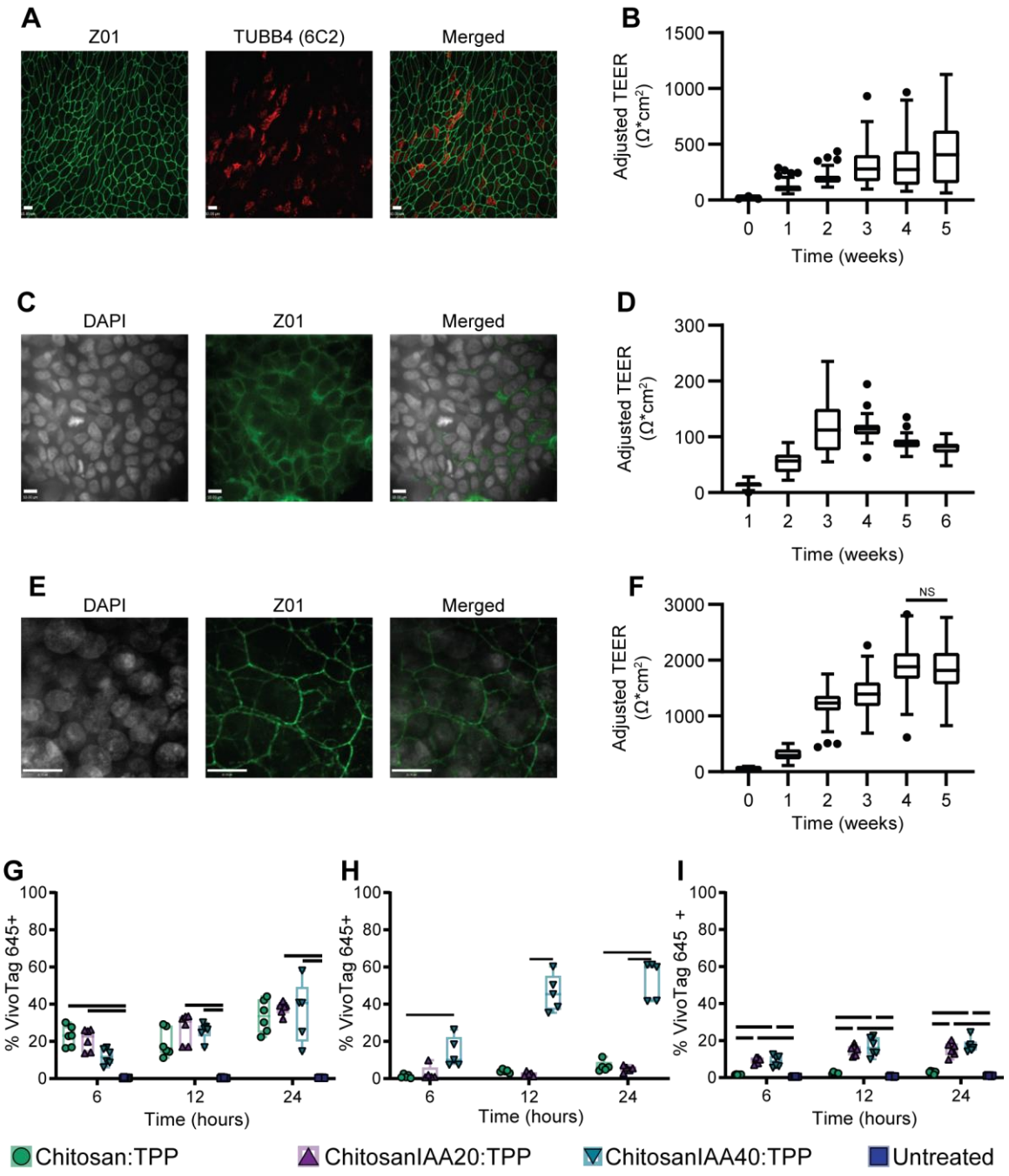

Figure 6: Chitosan Nanoparticle Uptake in Air-Liquid-Interface Cultures (A) Tight junction (Z01) and Cilia (TUBB4) staining of hSAECs and (B) corresponding TEER measurements (n = 80). (C) Nuclear (DAPI) and tight junction (Z01) staining of 6-week NuLi-1 cells cultured at ALI; image contrast was linearly adjusted for clarity, scale bar = 10 µm. (D) corresponding TEER measurements (n = 85). (E) Nuclear (DAPI) and tight junction (Z01) staining of 5-week CuFi-1 cells cultured at ALI, scale bar = 20 µm and (F)

corresponding TEER measurements (n = 80). ALI culture at 6, 12, 24 h for (G) hSAECs (H) NuLi-1, and (I) CuFi-1 (n = 5-6). 2-way-Anova ($\alpha = 0.05$).

VivoTag 645 tagged Chitosan:TPP, ChitosanIAA20:TPP, or ChitosanIAA40:TPP nanoparticles were delivered to the apical side of the transwell cultures on week 5 (hSAEC and CuFi-1) or 6 (NuLi-1) of culture. All 3 nanoparticle formulations were able to transport across the hSAEC mucus layer and be taken up by approximately 36% of the cells at 24 hours, Figure 6G. However, for the NuLi-1 at ALI, at 24 hours the cells were only positive for the Chitosan40IAA:TPP nanoparticle formulation, 53%, while the unmodified Chitosan:TPP and Chitosan20IAA:TPP were 7% and 6%, respectively, Figure 6H. In the CuFi-1 cultures, both IAA modified nanoparticles had percentage uptake at 15% and 17% relative to 3% for unmodified chitosan, Figure 6I. The final percentages for the CuFi-1 uptake were lower than for the hSAEC and NuLi-1 cultures. However, these transwells were the only cultures that appeared to be pseudostratified, which suggests that the nanoparticles were only endocytosed by the top layer of epithelial cells. These results suggest the IAA modified chitosan is able to transport more quickly through CF-like mucosa.

To determine whether the nanoparticle transport was representative of transport in human CF airway supernatant (ASN) nanoparticles were mixed with pooled patient CF ASN to measure track velocity changes between nanoparticle formulations, representative tracks Figure 7A. Track velocities increased with the higher modified IAA chitosan nanoparticles, Figure 7B,suggesting the IAA modified chitosan may be successful in transporting in human CF airways.

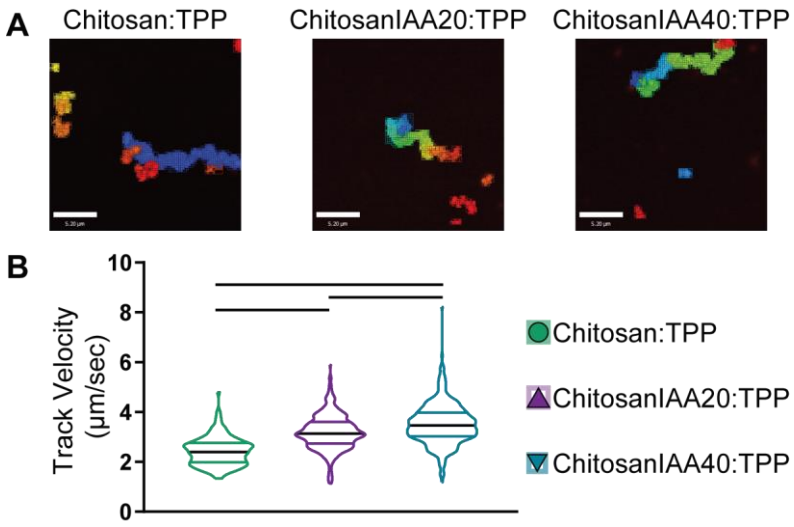

Figure 7: Chitosan nanoparticle formulation track velocity in CF ASN (A) Representative images of nanoparticle tracks, colors reference specific tracks picked up by Volocity, scale bar = 5.2 µm (B) Violin plots of the measured track velocities in CF ASN bars indicate statistical significance, Kruskal-Wallis with Dunn's multiple comparison ($\alpha = 0.05$, $n > 100$)

208 kDa Chitosan Nanoparticles: To determine whether any of the trends would replicate with a higher molecular weight chitosan, nanoparticles were fabricated with an 83% deacytelated 208 kDa chitosan. Nanoparticle formulations made with the higher molecular weight chitosan formulations doubled in size, Table 2. Nanoparticle formulations were then delivered to submerged hSAEC cultures since the 83 kDa nanoparticles had distinct differences in epithelial cell endocytosis. Similar trends in nanoparticle positive cells were seen compared to the smaller nanoparticles (Figure 5A), except at 24 hours, the unmodified Chitosan:TPP nanoparticles and Chitosan20IAA:TPP had higher percentages of nanoparticle positive cells, 68% and 92%, than the ChitosanIAA40:TPP nanoparticles, 45%, Figure 8A. For the air-liquid-interface culture, NuLi-1 were chosen since this culture formed a monolayer and showed distinct mucosal transport with the 83 kDa nanoparticles. The higher molecular weight chitosan IAA modified nanoparticles do not appear to be as efficient as the lower molecular weight

particles in transporting across the mucus secretions of the NuLi-1 cultures with percentage uptake at 7%, 6%, and 4% for Chitosan:TPP, Chitosan20IAA:TPP, and Chitosan40IAA:TPP. This clearly shows the transport of these larger particles are inefficient, Figure 8B-C.

Table 2: 208kDa Chitosan Nanoparticle Size

	Mean ± SD (nm)	PDI ± SD
Chitosan:TPP	152.9 ± 0.93	0.22 ± 0.01
ChitosanIAA20:TPP	131.1 ± 0.81	0.26 ± 0.00
ChitosanIAA40:TPP	142.9 ± 2.71	0.28 ± 0.01

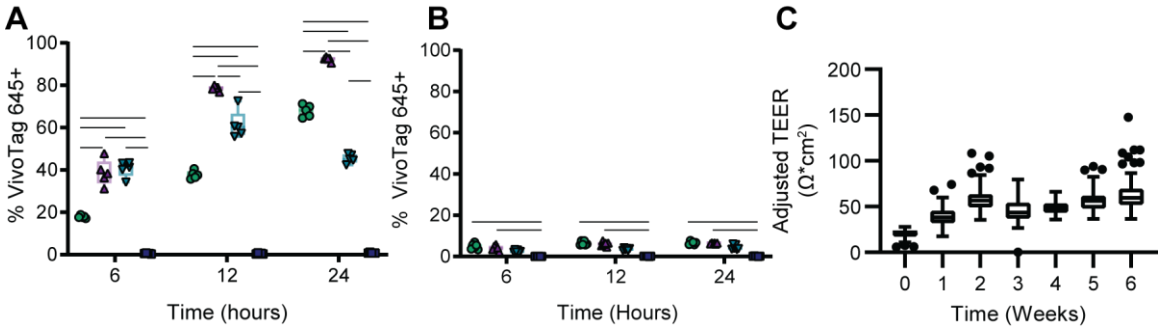

Figure 8: 208 kDa Chitosan Nanoparticle Formulation Delivery (A) hSAEC submerged culture uptake of Chitosan nanoparticles (n=5) and (B) NuLi-1 air-liquid interface culture uptake of particle formulations (n = 6) and (C) corresponding TEER measurements. Bars indicate statistical significance ($\alpha = 0.05$)

2.1.5.4 Discussion and Conclusions

The modification of chitosan with imidazole acetic acid was improved from previously published work reporting 2-3% IAA modification to controlled 20 and 40% modifications. These IAA modified chitosan nanoparticles enhanced nanoparticle transport through pulmonary mucosa in air-liquid interface cultures. This benefit appears to be dependent on the molecular weight of the chitosan and the correlating smaller sized particles. However, Novamatrix no longer produces the low molecular weight chitosan,

Protasan, and other low-molecular weight chitosan, such as Sigma Aldrich's (Cat. # 448869), resulted in particles larger than 200 nm. Fabrication of low molecular weight chitosan is a potential alternative [144–147].

CHAPTER 3. AIM 1: NANO-IN-MICRO *IN VITRO* CHARACTERIZATION

This aim had two broad goals for *in vitro* characterization of the Nano-in-Microgel multi-stage system: (1) to characterize the Nano-in-Micro system using reporter fluorescent nanoparticles and (2) to fabricate therapeutically loaded nanoparticles for targeting neutrophilic inflammation through delivery in the Nano-in-Micro system.

Pulmonary drug delivery is a non-invasive method for targeted delivery of therapeutics for the treatment of respiratory diseases such as asthma, idiopathic pulmonary fibrosis, or cystic fibrosis. For particle deposition in the respiratory airways and alveoli, the aerodynamic diameter of particles should fall between 1-5 μm, however, nano sized carriers are required for efficient endocytosis of intracellularly targeting small molecules or biologics. Additionally, alveolar macrophages rapidly clear particles with a geometric diameter in this 1-5 μm range. A nanoparticle-inside-microgel formulation could provide efficient, intracellular, deep lung delivery of nanoparticles and therapeutics. The microgel carriers are designed for (a) enzyme-triggered release of nanoparticles, (b) needed aerodynamic properties and (c) avoiding rapid clearance by alveolar macrophages. Additionally, the nanoparticles themselves have the benefit of preventing degradation of the therapeutics from these high levels of disease-related proteolytic enzymes, reducing rapid clearance, and allowing for efficient endocytosis.

We updated the previously reported Michael Addition during (water-in-oil) Emulsion (MADE) method [79] to a maleimide-thiol reaction. The maleimide-thiol provides faster reaction kinetics during fabrication while avoiding degradative conditions such as UV light, high temperatures, and organic solvents that could denature biologic

drugs or sensitive therapeutics during encapsulation. We fabricated both trypsin- and neutrophil elastase-responsive polymeric Nano-in-Micro, and for the first part of this aim studied the impact of starting polymer concentrations (20-50% w/v) for the microgel formulation on size, proteolytic degradation, and *in vitro* phagocytosis using two different crosslinkers: trypsin-responsive (CGRGGC) [79] and neutrophil elastase-responsive (CGAAPVRGGGGC) [88]. The trypsin-responsive peptide was used to expand the previously reported MADE method. A neutrophil elastase responsive peptide was chosen as this protease is well known to be involved in various acute and chronic pulmonary inflammatory diseases and would be relevant for the second half of this aim [4,62,89,90,148].

For the second part of this aim, several therapeutics were chosen in collaboration with the Tirouvanziam lab at Emory University to load into nanoparticle formulations: Roscovitine, Tanshinone IIA (TIIA), and Nexinhib20 (Nex20). Roscovitine is a cyclin-dependent kinase inhibitor that appears to function as a partial corrector for the most common CF mutation, F508del, and modulated the innate immune system [149,150]. Tanshinone IIA is isolated from *Salvia miltiorrhiza* and is believed to be an anti-inflammatory that has been shown to regulate myofibroblasts as well as macrophages during a bleomycin induced lung injury [151,152]. Nex20 has been previously shown to be a potent PMN exocytosis inhibitor of the intracellular target Rab27a that not only regulates exocytosis but also inhibits the up-regulation of the adhesion molecules CD11b and CD66b [153]. However, the poor solubility of Roscovitine, TIIA, and Nex20 in water is a significant disadvantage to therapeutic translation of the soluble drug often requiring the therapeutic be dissolved in DMSO prior to treatment. Each of these therapeutics is

encapsulated using an oil-in-water single emulsion into a poly(lactic-co-glycolic acid)-poly(vinyl) alcohol (PLGA/PVA) nanoparticle. We then encapsulated these water-soluble PLGA nanoparticles into our elastase-responsive microgels for pulmonary delivery modulating PMN-driven inflammation and confirmed *in vitro* microgel degradation and PMN nanoparticle uptake.

3.1 Methods

3.1.1 MADE Nano-in-Microgel Fabrication

Microgels were fabricated using Michael Addition During Water-in-Oil Emulsion (MADE). Equimolar amounts of a di-sulfhydryl peptide (CGRGGC, CGAAPVRGGGGC; CHI Scientific) and a 4-arm PEG Maleimide (Mal, 10kDa, Laysan Bio) were dissolved in PBS. Nanoparticles (0.1 µm Blue Fluospheres, ThermoFisher) and 0.01 mg of DyLight 650-4xPEG-mal or DyLight 488-mal (ThermoFisher, dissolved at 10 mg/mL in DMSO) were added to the PEG macromer solution. The PEG-peptide mixture was added to mineral oil with 1% v/v surfactant (Span 80/Tween 80, HLB = 5) and homogenized on a PRO Scientific D Series homogenizer for three minutes at 4000 rpm in a 35-40°C water bath. The emulsion was then left rotating for a minimum of two hours at 37°C. Microgels were removed from the surfactant and residual unreacted material by multiple centrifuge washes in water. To make non-enzyme responsive microgels, a 1 kDa HS-PEG-SH (Creative PEGWorks) was used in place of the peptide, and the solution pH lowered to increase the crosslinking time. Microgels were filtered through a 40 µm cell filter before use to prevent clogging of the flow cytometers and the Penn-Century MicroSprayer.

3.1.2 Microscopy and Analysis

Fluorescent images were collected either on a Zeiss 710 Laser Scanning Confocal Microscope with a 63X NA-1.4 oil Plan Apochromat objective or on a PerkinElmer UltraVIEW VoX spinning disk confocal microscope with a Hamamatsu C9100-23b back-thinned EM-CCD and Nikon 100x NA-1.45 oil objective. Sizing of swollen particles was performed with the MATLAB function "imfindcircles". Other image processing, particle-size in oil, calculations, stitching, and three-dimensional reconstruction were performed in Volocity (PerkinElmer Inc., USA).

3.1.3 Rheometry

Hydrogel storage and loss moduli were measured by dynamic oscillatory strain, and frequency sweeps using an MCR 302 Rheometer (Anton Paar) with a 9 mm diameter 2° cone and plate set at 25°C. Bulk hydrogels were made in 4.5 mm diameter silicone isolators, crosslinked, then removed from the isolators and allowed to swell in PBS overnight. One gel per formulation was used to determine the linear viscoelastic range of the hydrogel using a strain amplitude sweep with an angular frequency of 10 rad/s; strain from the linear portion was then used for the oscillatory frequency sweeps. Frequency sweeps were run with the constant strain from ω = 0.1-100 rad/s or until at least six points were linear.

3.1.4 In-vitro Degradation

Microgels were studied in both the absence and presence of enzyme using time-lapse imaging of a loaded cell trap provided by the Lu lab [154]. The use of a cell trap allows for the imaging of Nano-in-Micro degradation over time with a high n (n > 100) per run. Once traps were loaded DyLight 650 labeled microgels, enzyme solutions were flown

into the trap, and the trap was fluorescently imaged every minute for 30 minutes on a BioTek Lionheart. Images were stitched and analyzed in Gen 5.02 (BioTek). De-identified CF pooled patient sputum, airway supernatant (ASN), was collected by the Emory Biospecimens Repository under protocols approved by the Institutional Review Boards at Emory University and Georgia Institute of Technology.

3.1.5 Pore Size Calculation

The pore size of the microgels was estimated as described by Canal and Peppas [155]; these equations, (1-3), were designed to correlate the mesh size of a crosslinked network of a single polymer type and, as our microgels do not adhere to this requirement, can only act as an estimate. The bond length, l (1.46 Å), molecular weight of the repeating unit, Mr (44 g/mol), and characteristic ratio Cn (4), were used from PEG in Equation 1. The average molecular weight between cross-links, Mc, was calculated from the combined PEG and peptide molecular weights, 5551.63 g/mol for trypsin-responsive and 6004.15 for Elastase-responsive. For the equilibrium polymer volume fraction, $v_{2,s}$, (Equation 2) the swelling ratio, Q, was calculated from the mean size in the swollen and relaxed states measured by microscopy; this was confirmed with previously reported swelling ratio of the 60% w/v acrylate Trypsin microgels [79]. The values from both equations 1 and 2 were then used to solve for mesh size, ξ, Equation 3.

Equation 1
$$\left(\bar{r}_0^2\right)^{\frac{1}{2}} = l\left(\frac{\bar{M}_c}{M_r}\right)^{\frac{1}{2}} C_n^{\frac{1}{2}}$$

Equation 2
$$v_{2,s} = \frac{V_p}{V_s} = \frac{1}{Q}$$

Equation 3
$$\xi = v_{2,s}^{-1/3}\left(\bar{r}_0^2\right)^{1/2}$$

3.1.6 Macrophage Uptake Study

RAW 264.7 cells (ATCC) were cultured in DMEM media supplemented with 10% Fetal Bovine Serum (FBS) 100 U/mL/100 µg/mL Penicillin-Streptomycin (HyClone) in a 37°C incubator with 5% CO_2. RAW cells were detached by scraping and stained with CellTrace Yellow (ThermoFisher) following manufacturer instructions, then incubated with 20-50% w/v Nano-in-Micro at a 1:1 ratio in a 96 well V-bottom plate. At 0.5, 1, 2, 6, and 12 hours the plates were moved to 4C, and the cells stained with Zombie Green (BioLegend) and fixed with Cytofix (BD Biosciences). Fluorescence was evaluated using a BD LSR Fortessa with a high-throughput system.

3.1.7 PLGA Nanoparticle Fabrication

Nanoparticles were fabricated using a single emulsion solvent evaporation method. 0.8-1 mg of therapeutic and 0.2 mg of fluorophore (Rhodamine B, Sigma Aldrich, or DiR, ThermoFisher Sci.), and 100-130 mg of Poly (D,L-lactide-co-glycolide) (PLGA RG502H, Sigma Aldrich) were dissolved in 2 mL of ethyl acetate. The PLGA mixture was then added to 4 mL of 2.5% w/v poly(vinyl) alcohol (PVA; Sigma) and sonicated using a Sonics Vibra-Cell VCX130 with CV18 at 65% for 10 min on ice. The emulsion was then added to 50 mL of 0.3% w/v PVA solution and magnetically stirred for 5 hours. The nanoparticles were centrifuged at 8000 g for 10 minutes, pellet discarded, and nanoparticles in the supernatant were then washed in DI water by centrifuging at 100,000 g for 30 minutes. After the second DI rinse, the nanoparticles were resuspended in 5 mL 1% w/v trehalose solution, snap frozen in LN, lyophilized for 48 h, and stored at -20°C. Nanoparticles were resuspended at 1 µg/mL in water and run on a Malvern ZetaSizer or NanoSight depending on fluorophore encapsulated to determine the mean particle size. Therapeutics attempted were: (R)-

Roscovitine (Cayman Chemicals), Tanshinone IIA (Cayman Chemicals), Nexinhib20 (Cayman Chemicals). Drug encapsulation was measured by degrading the PLGA particles in DMSO or NaOH and measuring the drugs' absorbance against a standard curve using a BioTek Synergy HT plate reader; Roscovitine: $\lambda = 290$, Nex20: $\lambda = 290$, TIIA: $\lambda = 290$. Endotoxin levels were tested using a chromogenic LAL kit (ThermoFisher) following manufacturer's instructions.

3.1.8 PLGA Nano-in-Micro Fabrication

The PLGA nanoparticles can be encapsulated into the microgel formulation as previously described with minor modifications to the preparation of the PEG precursor solution. The PLGA nanoparticles were resuspended at 10 mg in 80 µl of PBS, allowed to dissolve, and sonicated for 5 minutes. This was then used to dissolve the 4-arm PEG MAL precursor solution before following the rest of the MADE method.

3.1.9 PMN in vitro Transmigration

This assay was performed as previously reported [130]. Briefly, PMNs were isolated from health donor's blood, according to an approved Emory University Institutional Review Board protocol, using Polymorphprep (Alere Technologies AS, Oslo, Norway) as per manufacturer protocol. Purified neutrophils were then loaded on the transmigration chamber. Transmigration and following incubations were performed using 100 nM of Leukotriene B4 (LTB4) (EMD Millipore) in RPMI or airway supernatant from CF sputum. The uptake of fluorescent microgels was then assessed 10 hours post transmigration by directly incubating PMNs recruited apically with microgels at a 1:10 ratio (PMN to microgel) in either CF ASN or RPMI for 30 and 60 minutes and quantified using flow cytometry ($n = 1$).

3.1.10 Statistical Analysis

Data were analyzed using GraphPad Prism with a Shapiro-Wilk test for normality (α=0.05). A one-way Anova (α = 0.01) with post-hoc Tukey's test with an adjusted P value for multiple comparisons or for two factors a two-way Anova (α = 0.01) with Sidak post hoc analysis was used with data that passed Shapiro-Wilk. Where applicable, a Mann-Whitney (α = 0.01) or Kruskal-Wallis (α = 0.01) with Dunn's test was used for data that failed Shapiro-Wilk.

3.2 Results and Discussion

3.2.1 Nano-in-Microgels for Aerodynamic and Geometric Size

Microgel formulations were made at 20, 30, 40, 50% w/v starting polymer concentration to assess the effect on microgel size, degradation, and macrophage phagocytosis. 4-arm PEG Maleimide was crosslinked with a trypsin-responsive (CGRGGC) or neutrophil elastase-responsive (CGAAPVRGGGGC) peptide backbone via crosslinking of the thiols on the cysteine residues. A maleimide-thiol reaction was chosen for the Michael Addition During water-in-oil Emulsion because of the faster kinetics relative to an acrylate-thiol [156]. By using both trypsin- and elastase-degradable crosslinker, we show the versatility of the multi-stage system, whereby the crosslinker can be exchanged for different disease-related protease responsive sequences. These peptides allow for the controlled degradation of the microgels by proteases to release their nanoparticle cargo, schematic representation in Figure 9A.

To fluorescently label the microgel for imaging and flow cytometry, a DyLight 650-4x-PEG-Maleimide or DyLight 488 Maleimide was added to the 4x-PEG-Maleimide precursor solution; representative images of a DyLight-650 labeled microgels with

encapsulated 60 nm carboxylated polystyrene beads can be seen in Figure 9B. DyLight 650 labeled the microgels clearly for all 20-50% w/v for flow cytometry, but not 60% w/v formulation, Figure 10A, DyLight 488 labeled in Figure 10B. Carboxylated beads (60 nm) can be seen in more than 89% of the microgels by flow cytometry, Figure 10B (orange). Encapsulation efficiency of the 100 nm Blue Fluospheres (used for *in vivo*) for each formulation was between 30-40% with total nanoparticles encapsulated (~1e11) in the microgels within the same order of magnitude as theoretical maximum (3.6e11), Table 3.

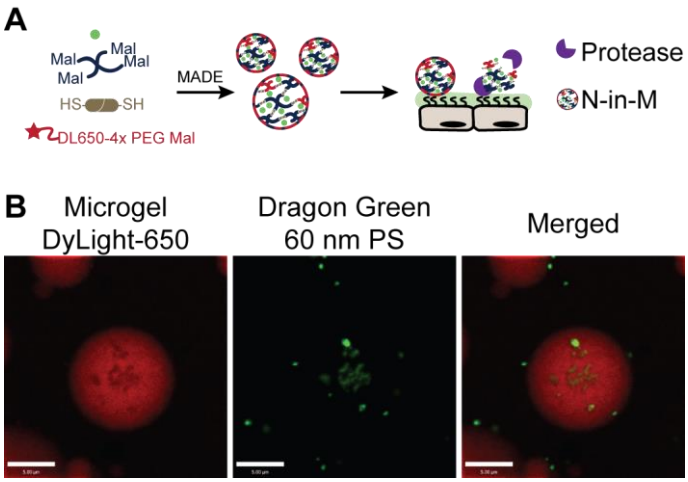

Figure 9: Nano-in-Micro Representative Schematic and Images (A) Schematic of Nano-in-Micro particle formulation and protease dependent microgel degradation and nanoparticle release (B) Representative image of a 20% trypsin-responsive DyLight 650 labeled microgel encapsulating 60 nm Dragon Green polystyrene beads; scale bars 5 µm, contrast linearly adjusted for clarity.

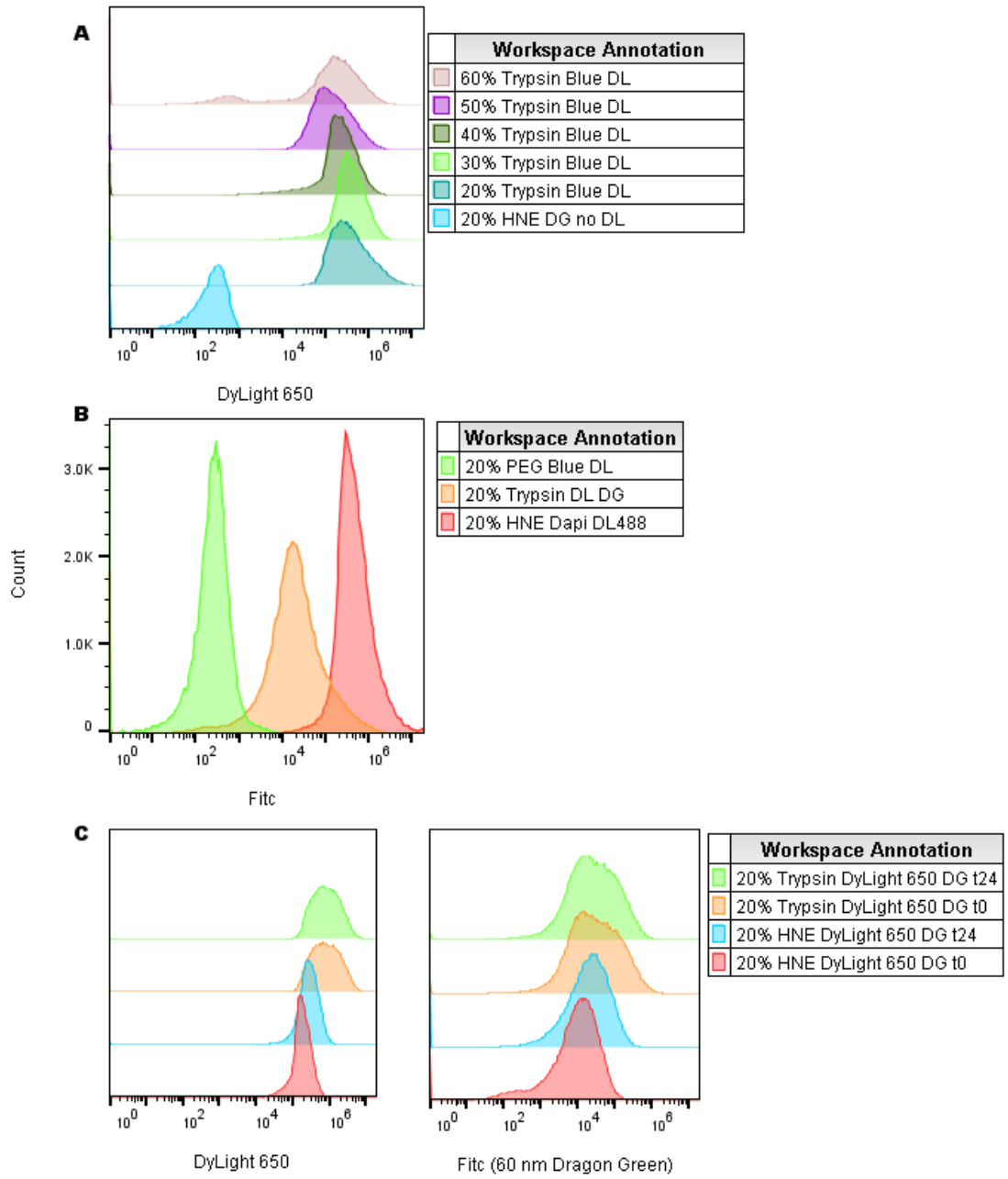

Figure 10: Flow Cytometry Characterization of Nano-in-Micro (A) Accuri signal of fluorescently DyLight 650 (DL) labeled microgels for the following formulations; no DyLight 650 (cyan), Trypsin-responsive 20% (blue), 30% (light green), 40% (dark green), 50% (purple), 60% (light purple) (B) Microgels without Dragon Green (DG) nanoparticles (light green), with 60 nm Dragon Green nanoparticles (orange), and microgels labeled with DyLight 488 (red). (C) Microgel fluorescence on Day 0 for 20% w/v Trypsin (Light Green) and 20% Elastase (red) and fluorescence 24h later for the same batch (orange, blue respectively).

Table 3: 100 nm Blue Fluosphere Encapsulation in Microgels

% w/v	% Encapsulation	# NP Encapsulated
	Trypsin (CGRGGC)	
20	34%	1.2E+11
30	30%	1.1E+11
40	42%	1.5E+11
50	31%	1.1E+11
	Elastase (CGAAPVRGGGGC)	
20	31%	1.2E+11
30	33%	1.2E+11
40	33%	1.1E+11
50	32%	1.1E+11

The geometric diameter of the microgels was measured with means between 4.5-8.5 µm for each starting polymer concentration, Figure 11B, D. Mean size generally increased with the increase of starting polymer concentrations; however, none of the formulations were significantly different. The lowest size is limited by the imaging technique used for the measurement. 60% w/v microgels were not included in the studies as their yield was low and the viscosity of the solution was difficult to transfer to the homogenizer efficiently. Aerodynamic diameter (Da) is dependent on the geometric diameter (Dg), shape factor (1 for spheres) and density of the particle through the following relationship: $Da = Dg*\rho^{0.5}$. Using the density of PEG as 1.13 g/mL, aerodynamic diameters of various microgel formulations were calculated and are shown in Table 4. Aerodynamic diameters of 1 to 5 µm are most suitable for deep lung deposition; this corresponds to a theoretical geometric size range of 0.94 and 4.7 µm for PEG based particles. This range is represented by dashed grey lines on Figure 11A, C. The actual aerodynamic diameter measured by a next generation impactor, after developing a dry powder formulation, would be necessary to account for microgel aggregation, density, and shape factor.

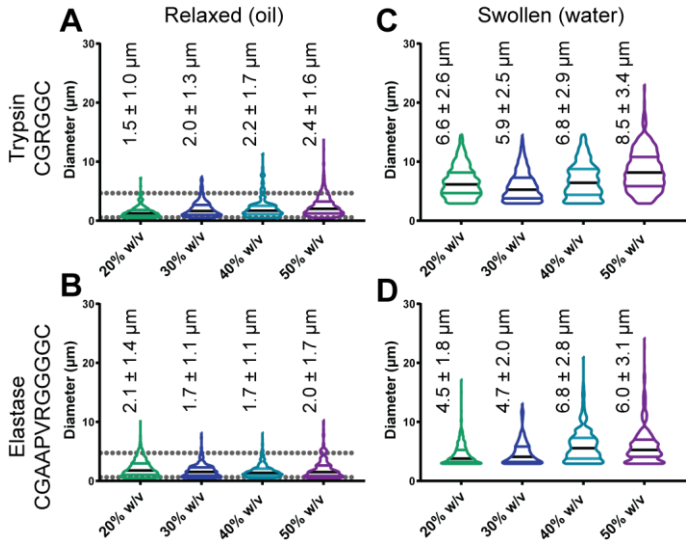

Figure 11: Trypsin- and Elastase-Responsive Microgel Size Distribution (A) trypsin- and (C) neutrophil elastase-responsive in the relaxed state and in the (B, D) swollen state. The dashed grey lines on the relaxed state are the min-max theoretical aerodynamic diameter range. Each violin plot is from max to min with median (black line) and quartiles labeled, n > 200 for each measurement.

Table 4: Calculated Aerodynamic Diameters

	Trypsin (CGRGGC)		
% w/v	Mean (µm)	Std Dev.	75 Percentile
20	1.6	1.0	1.9
30	2.1	1.4	2.8
40	2.3	1.8	2.7
50	2.6	1.7	3.4
	Elastase (CGAAPVRGGGGC)		
20	2.3	1.5	3.2
30	1.8	1.1	2.4
40	1.8	1.1	2.2
50	2.1	1.8	2.8

3.2.2 Greater Than 95% of Microgels Degrade Within 30 Minutes in vitro

In order to confirm enzymatic degradation of the microgels, Nano-in-Micro particles were loaded into single cell traps [154] then exposed to the relevant proteases and imaged over time (Figure 12A). Trypsin-responsive microgels were degraded in 0.01 mg/mL of trypsin (≥ 90 u/mL); for all formulations, 95% of microgels degraded within 20

minutes. These studies were repeated with the neutrophil elastase microgels degraded in de-identified pooled cystic fibrosis patient sputum. For all elastase formulations, 95% of microgels degraded within 25 minutes of exposure to the sputum. It is also possible that the protease-responsive crosslinkers be non-specifically degraded by other proteases present; e.g., cathepsin S on the elastase peptide (probability of cleavage found using PACMANs [157]). Non-enzyme degradable 20% w/v microgels were fabricated by crosslinking with a dithiol PEG and exposed to 0.01 mg/mL of trypsin (≥ 900 u/mL) as a control to show the peptide crosslinker is necessary for enzyme-responsive degradation. The fluorescence trend of the non-enzymatically degradable PEG microgels followed that of several sets of trypsin and elastase crosslinked microgels tested for photobleaching of the microgels; the mean at 25 minutes is 91%, Figure 12B. Interestingly, we did not observe a difference in degradation when varying polymer concentrations. This could be due to either the limits of the measurement method (1-minute intervals) or simply the polydispersity of the microgels and overlap in size of the different groups. It is also possible that the protease concentration is high and the kinetics of degradation is much faster than the increase in the number of crosslinks. The release of 100 nm nanoparticles will follow the degradation curve as the theoretical pore size calculated [155] is smaller than the nanoparticles, Table 5.

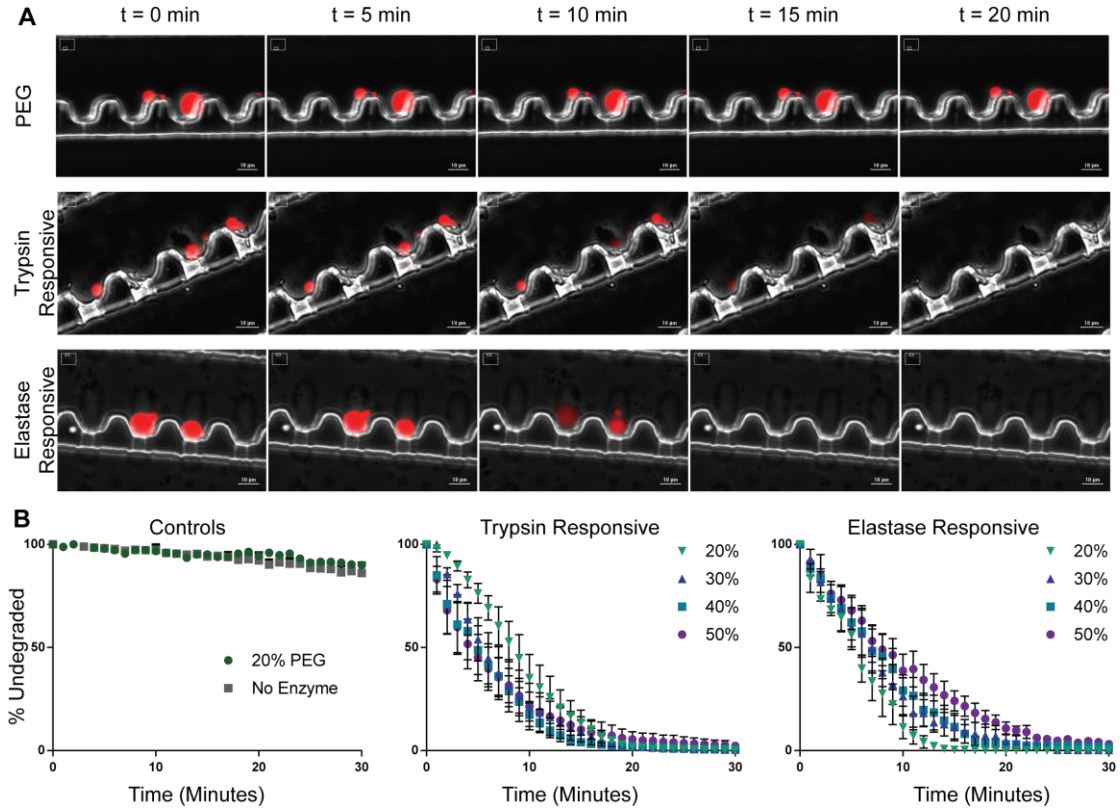

Figure 12: Trypsin- and Elastase-Responsive Microgel Proteolytic Degradation (A) Representative images of microgels crosslinked with PEG, trypsin-, or elastase-responsive peptides degrading in the presence of their respective enzymes (0.01 mg/mL trypsin; CF patient sputum for elastase). (B) Mean ± SEM plots of the percent of microgels remaining in the trap over 30 minutes for PEG microgels exposed to trypsin or photobleached trypsin/elastase microgels (N = 5), and enzyme degradation of trypsin (N = 5), and elastase (N = 3). Trypsin- and elastase- responsive microgels were tested for each 20-50% w/v starting polymer concentration with 95% of trypsin responsive microgels degrading in 20 minutes and 95% of elastase responsive degrading in 25 minutes.

Table 5: Theoretical Pore Size

% w/v	nm
	Trypsin (CGRGGC)
20	20
30	14
40	14
50	16
	Elastase (CGAAPVRGGGGC)
20	10
30	13
40	16
50	19

3.2.3 20-50% w/v Bulk Hydrogels are Relatively Soft

Since macrophage phagocytosis has been shown to be interdependent on size and mechanical properties of the particles [158,159], we next measured storage (G') and loss (G") moduli of the bulk hydrogels. For the trypsin-responsive crosslinker, the 20% w/v had significantly lower loss modulus than the 40 and 50%. Furthermore, both trypsin and elastase crosslinker 20% w/v formulation had lower storage modulus than the 40 and 50% w/v bulk gels. However, across all formulations, the hydrogels are relatively soft (10kPa), Figure 13; the measurements for 20-50% w/v with trypsin or elastase peptide crosslinkers are grouped along the x-axis by G' and G".

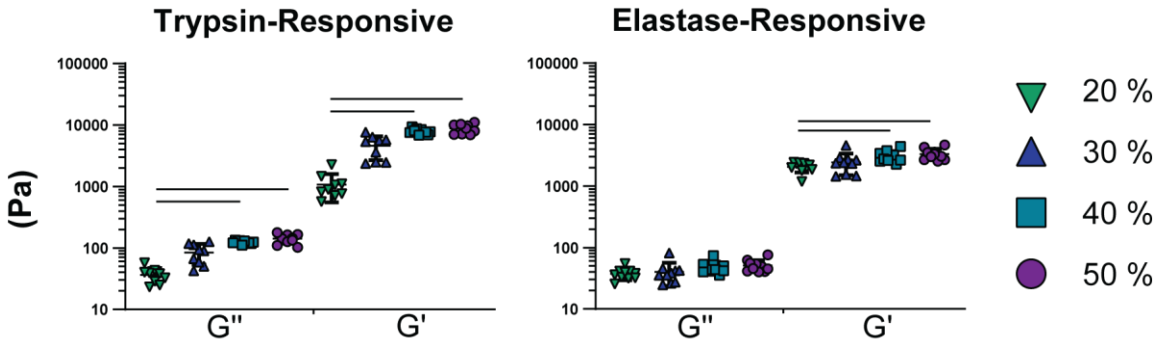

Figure 13: Storage and Loss Moduli for Trypsin- and Elastase- Responsive gels Bulk hydrogels with starting polymer concentrations from 20-50% w/v (n = 8). Bars within formulation are group mean ± SD. Horizontal bars represent statistical significance, Kruskal-Wallis with Dunn's multiple comparison test ($\alpha < 0.01$)

3.2.4 Increased Polymer Concentration Slows RAW 264.7 Phagocytosis

To study macrophage phagocytosis *in vitro*, DyLight 650 labeled Nano-in-Micro particle formulation (20-50% w/v) were mixed and incubated with RAW 264.7 cells at a 1:1 cell:particle ratio. At 0.5, 1, 2, 6, and 12 hours of incubation, the cells were fixed and analyzed using flow cytometry. After fixing, a small sample of cells from each treatment group was placed on a slide and imaged on a spinning disc confocal. A representative image (Figure 14A) showed that multiple particles could be phagocytosed by the same

cell. Over time, the percentage of macrophages that were positive for the microparticles increased for each formulation of microgel; however, the higher polymer concentrations had a lower percentage of macrophages positive for the microgels across time, potentially due to a combination of the slight differences in sizes and/or the rheological properties of the microgels. This trend was observed for both the trypsin- and elastase-responsive microgels, Figure 14B.

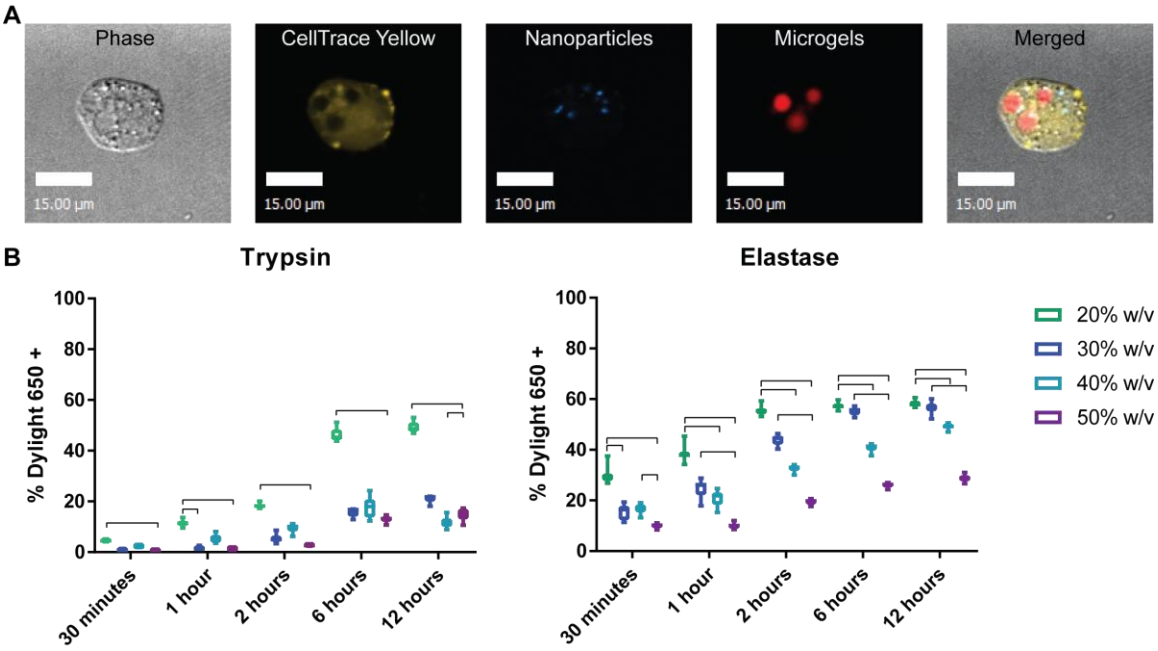

Figure 14: RAW 264.7 Macrophage Microgel Uptake (A) Representative images of a CellTrace Yellow labeled macrophage with 100 nm Blue Fluospheres, and DyLight 650 labeled microgels, linearly contrasted for clarity. (B) Microgel uptake measured by flow cytometry of the percentage of DyLight 650 positive RAW 264.7 macrophages for trypsin- (n=6) and elastase- responsive (n=12) microgels over time. Kruskal-Wallis with Dunn's multiple comparison test, bars represent statistical significance, $\alpha < 0.01$.

3.2.5 Therapeutic Loading into PLGA Nanoparticles

An oil-water single-emulsion solvent evaporation technique was used to encapsulate Roscovitine, Nex20, and TIIA with a red or near-IR dye. A single-emulsion was chosen as each of the drugs have poor water solubility and thus only needed the oil phase for encapsulation while producing sub-300 nm particles; mean size using this method

was below 200 nm. Roscovitine Rhodamine B PLGA nanoparticles mean size was 162.9 +/- 1.8 nm with a polydispersity index (PDI) of 0.23 measured by ZetaSizer. Nex20 DiR PLGA nanoparticle size was measured using a NanoSight since the DiR dye is not compatible with the laser used by the ZetaSizer. Nex20 DiR PLGA nanoparticles mean size was 145.6 +/- 3.3 nm with a D90 of 196.5 +/- 8.9 nm; Tanshinone IIA DiR PLGA nanoparticles were 140.7 +/- 1.3 nm with a D90 of 181.1 +/- 4.8 nm; DiR only PLGA nanoparticles mean size was 177.2 +/- 4.3 nm with a D90 265 +/- 9.5 nm. Nanoparticles (> 60 mg/mL) were degraded to measure the therapeutic loading efficiency. Roscovitine Rhodamine B PLGA nanoparticles were loaded at 3.09 µg/mg Roscovitine to PGLA formulation for a 49.1% encapsulation efficiency. Nex20 was loaded at 1.48 µg/mg of PLGA formulation, 21% encapsulation efficiency. TIIA was loaded at 0.05 µg/mg of PLGA formulation for a 6.6% encapsulation efficiency. Although Roscovitine, Nex20, and TIIA all loaded in the PLGA nanoparticles, the TIIA loading efficiency was low and may need a modified particle formulation for higher therapeutic delivery. Endotoxin levels were tested on 1 mg/mL of nanoparticles using a chromogenic LAL assay kit; DiR only was 0.31 EU/mL, TIIA DiR was 0.23 EU/mL, and Nex20 DiR nanoparticles were 0.24 EU/mL.

3.2.6 PLGA Loading into Nano-in-Micro

The PLGA Nano-in-Micro was designed for neutrophil elastases mediated degradation. Inflammation in diseases such as asthma, chronic obstructive pulmonary disorder (COPD), and cystic fibrosis is often mediated by polymorphonuclear neutrophils (PMNs). One of the hallmarks of PMN driven inflammation is the highly proteolytic microenvironment created by the release of proteases such as neutrophil elastase (NE) and metalloproteinases (MMP) [62,90,91,160,161]. Once the Nano-in-Micro is delivered, the

microgels degrade releasing the nanoparticles; the therapeutic nanoparticles can then modulate PMN exocytosis activity (e.g. Nex20), reducing the exogenous elastase, creating a negative feedback loop for future doses. Since the PLGA formulations included a near-IR dye, the DyLight 640-4xPEG Mal was exchanged for a DyLight-488 Mal to label the microgel (4x-PEG Mal DyLight 488 were unavailable). Representative images in Figure 15A showed many microgels appeared to have large aggregates of the PLGA formulation, suggesting poor loading may be due to insufficient dispersion of the nanoparticles. The mean size of these particles was 3.2 μm with a range of 8 μm. Flow cytometry showed the microgels incorporated the DyLight 488 dye (100% positive), Figure 15B; however, the PLGA formulations (DiR) were found to have poor distribution within the microgels, ranging from 14-18% of the microgels positive for the DiR nanoparticles, Figure 15C. This distribution was improved from 18% to 48% by including a sonication step during fabrication when the PLGA nanoparticles were resuspended in PBS before encapsulation within the microgels, Figure 15D.

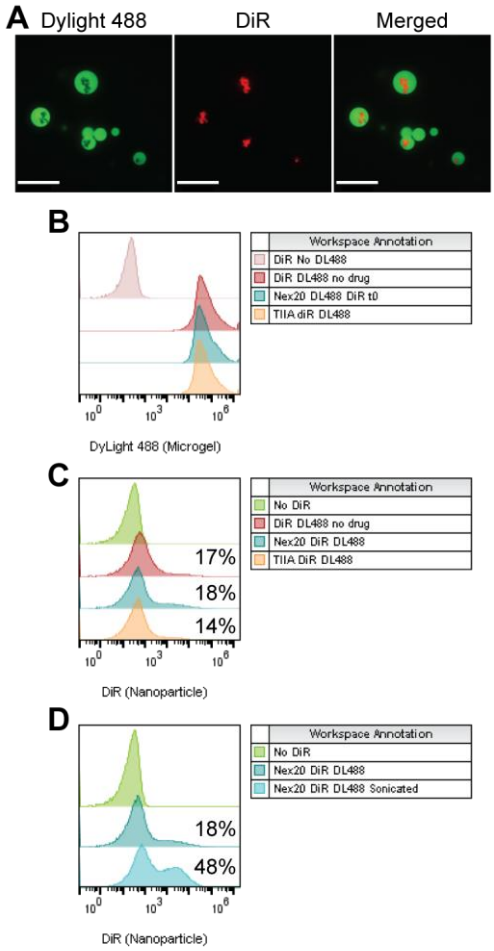

Figure 15: PLGA Nano-in-Micro (A) Representative images of DyLight 488 labeled elastase-responsive microgels loaded with DiR labeled PLGA nanoparticles, images linearly contrasted for clarity, scale bar = 20 µm. (B) BD Accuri flow profiles of microgels loaded with DiR PLGA nanoparticles without DyLight 488 loading (light pink), DiR with DyLight 488 (red), Nex20 DiR PLGA with DyLight 488 (blue), and TIIA DiR PLGA with DyLight 488 (orange). (C) Microgels without nanoparticles (green), 17 % loaded with DiR PLGA (red), 18 % loaded with Nex20 DiR PLGA (blue), 14 % loaded with TIIA DiR PLGA (orange) (D) Increase in Nex20 PLGA nanoparticles encapsulation from 18 to 48 % after sonication during fabrication (light blue).

Prior degradation results were confirmed by repeating the single-cell trap Nano-in-Micro degradation with Nex20 DiR PLGA loaded elastase-responsive 20% w/v Nano-in-Microgels, Figure 16A. The degradation followed similar trends as Figure 12, with 90 ± 2.5% of the microgels degraded within 25 minutes and 95% degraded in 30 minutes; the

slight increase in degradation time is most likely due to using a different pooled CF airway supernatant (ASN) sample. The Nano-in-Microgels were then tested by the Tirouvanziam lab in an *in vitro* transmigration model, which uses the relevant biological milieu, i.e. CF ASN, for PMN transmigration (TRM) and allows the recapitulation of the *in vivo* PMN airway phenotype found in CF patients [130]. We measured nanoparticle uptake by these airway PMNs using 60 nm fluorescent (Dragon Green) carboxylated polystyrene nanoparticles encapsulated within un-labeled elastase-responsive microgels. LTB4, a leukotriene produced by leukocytes during inflammation, and CF ASN were used to transmigrate PMN in the *in vitro* system. These PMNs were then collected and exposed to the elastase-responsive Nano-in-Micro at a 1:10 ratio in either RPMI medium or additional CF ASN. This showed that the degradation of the microgels in the presence of CF ASN increased the percentage of PMN positive for the nanoparticle by 5-10% at 60 minutes, regardless of the transmigration milieu (LTB4 or CF ASN), Figure 16B. Additionally, when both PMNs transmigration and the Nano-in-Micro are in the CF ASN milieu, there is an increase in PMNs positive for the fluorescent nanoparticles. Together, these data indicate that for efficient uptake of nanoparticles by airway PMNs, the elastase-responsive microgel must degrade first. Furthermore, there is an additive effect between the acquired PMN phenotype, imprinted by the transmigration condition (CF ASN vs LTB4), and the incubation milieu with the Nano-in-Micro system. This suggests that targeting of airway PMNs by the Nano-in-Micro system would be more efficient in pathological settings (CF ASN) rather than during the normal course of inflammation (LTB4).

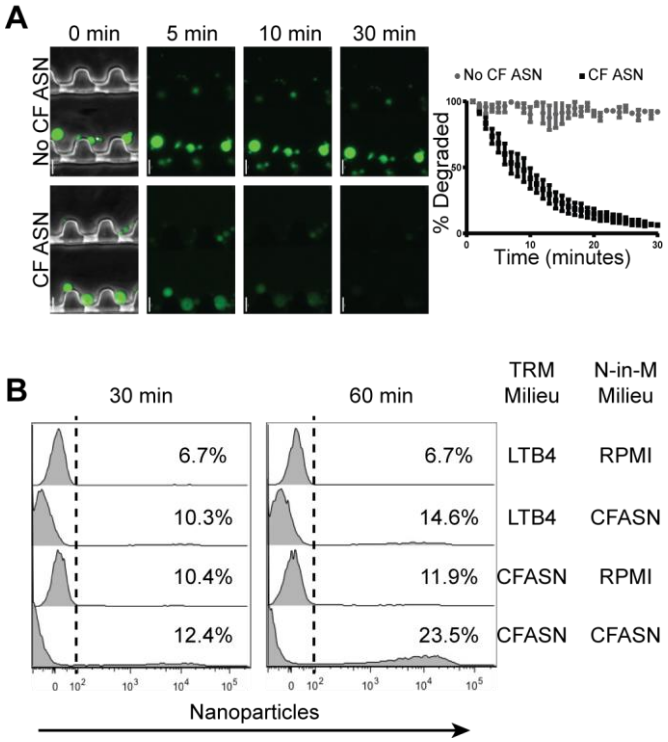

Figure 16: Elastase-Responsive Degradation and PMN Uptake (A) Nex20 DiR PLGA nanoparticles were encapsulated in 20% w/v elastase-responsive microgels, loaded into a single-cell trap, and imaged for 30 minutes with or without pooled CF airway supernatant (ASN); scale bar = 10 μm, mean ± SEM, N = 3 (no CF-ASN), N = 6 (CF-ASN). (B) PMNs were transmigrated (TRM) by either LTB4 or CF ASN, then given Nano-in-Microgels in either RPMI media or CF ASN. PMN that transmigrate (TRM) in the CF ASN milieu readily show fluorescence of the nanoparticles encapsulated in NE-responsive microgels when the Nano-in-Micro is delivered to a CF ASN milieu rather than media alone (n = 1).

3.3 Conclusions

The purpose of these studies was to understand (1) how the starting polymer concentration of our Nano-in-Micro multistage particles influenced the size and *in vitro* degradation and phagocytosis and (2) the incorporation of immune mediating therapeutics into the Nano-in-Micro system. This *in vitro* work has further improved upon the MADE method by changing the chemistry for faster reaction kinetics, shown the incorporation of a disease-relevant protease-responsive peptide, and shown the flexibility in exchanging nanoparticles. These results provide a further understanding of how enzymatically-

degradable multi-stage polymeric carriers can be used for pulmonary drug delivery. The following chapter will investigate the *in vivo* response to these multi-stage particles.

CHAPTER 4. AIM 2: NANO-IN-MICRO *IN VIVO* CHARACTERIZATION

The purpose of this aim is to understand how the Nano-in-Micro multi-stage system interacts with the innate immune cell environment in *in vivo* mouse models. The goals of this aim are: (1) characterize the phagocytosis and clearance of the Nano-in-Micro system in naïve mice following pulmonary delivery and (2) test the efficacy of the delivery system in an acute neutrophilic inflammation model using fluorescent reporter particles and immunomodulatory therapeutics.

Polymorphonuclear neutrophils (PMNs) play a central role in the pathophysiology of several disorders, such as rheumatoid arthritis [162], systemic lupus erythematosus [163], acute lung injury [164], asthma [165], chronic obstructive pulmonary disease (COPD) [92], and cystic fibrosis (CF) [166]. Importantly, although PMNs have been considered short-lived and with little opportunity for plasticity, recent studies have challenged this dogma, particularly in chronic inflammatory diseases [150,167–169], suggesting prolonged PMN lifespan, active release of proteolytic mediators and thus opening new therapeutic opportunities. However, despite the role of PMNs and PMN-derived mediators in shaping the clinical outcomes in disease, there is a clear lack of therapies and delivery methods allowing PMN-specific targeting in highly proteolytic microenvironments.

One of the hallmarks of PMN-driven inflammation lung diseases, such as acute respiratory distress syndrome, CF, and COPD, is the highly proteolytic microenvironment created by the release of neutrophil elastase (NE) and metalloproteinases (MMP), such as MMP-9 [170]. Additionally, accumulation of these PMN-derived proteases leads to the

saturation of the antiprotease shield and unopposed proteolytic action, causing structural lung damage and decline in lung function [90,160]. The highly proteolytic microenvironment, as well as presence of other detrimental enzymes, such as myeloperoxidase, in the diseased areas of the lungs represent a current challenge for the effective delivery and preservation of the efficacy of the drugs aimed at targeting airway disease and inflammation [90,171–173].

However, delivery of drugs encapsulated in nanoparticles represents a viable strategy to overcome the challenges of drug modifications induced by the microenvironment before they reach the cell of interest. Pulmonary drug delivery offers an alternative administration route that allows for site-specific delivery of therapeutics for respiratory airway disease; efficient localized delivery can potentially reduce the overall dose needed as well as reduce systemic toxicity from the therapeutic. The design of the Nano-in-Micro system not only allows the microgel to provide the needed aerodynamic size for deposition and geometric size to avoid rapid clearance (< 1 hour) but also takes advantage of the high proteolytic microenvironment for controlled release of the drug-loaded nanoparticles.

While particle deposition in the lungs is an important factor to the delivery of the Nano-in-Micro system, the aerodynamics of mice airways do not recapitulate those of the human airways. However, a naïve mouse model can be used to understand the *in vivo* response time frame for clearance by the mucociliary elevator and phagocytic innate immune cells. Additionally, an acute neutrophilic inflammation can be induced by administering lipopolysaccharide (LPS), a TLR-4 agonist, directly to the lungs; this model

predominantly recruits polymorphonuclear neutrophils (PMN). PMN peak in the tissue lysate at 2-4h, and around 12h in the bronchoalveolar lavage [174,175].

4.1 Methods

4.1.1 Ethical Statement

All studies were performed according to protocols approved by the Institutional Animal Care and Use Committee (IACUC) at the Georgia Institute of Technology, Emory University, and the University of Alabama Birmingham, and all methods were performed in accordance with the relevant guidelines and regulations.

4.1.2 Pulmonary Administration

C57BL/6 and 8-12 weeks old female Balb/c mice (Jackson Laboratories) were maintained in pathogen-free facilities, given sterile water, and food (low alfalfa if used for imaging) ad libitum. Using a 1A-1C MicroSprayer Aerosolizer and FMJ-250 high pressure syringe assembly (Penn-Century, Inc.) for aerosolized delivery, mice were anesthetized with a Ketamine/Xylazine 80-100 mg/kg/10-20 mg/kg cocktail, positioned on an intubation table, endotracheally intubated with a 1.22 mm ET Tube (Hallowell EMC), and swollen Nano-in-Micro formulations (1e6 microgels in 50 µL) were injected. If there was device failure the mouse was marked for follow up and removed from data sets; all samples removed were marked within the relevant IVIS figures. For oropharyngeal aspirations, mice were anesthetized with isoflurane, placed on an intubation table, then the tongue was pulled and held with atraumatic forceps as the formulation was administered into the mouth, and the nose gently covered until the liquid was inhaled. Within experiments, the concentration of microgels was equal between formulations. After sacrificing the mice with sodium pentobarbital, perfusing the lungs with PBS through the right ventricle then

excising the lungs, the fluorescence intensity of the excised lungs was measured by imaging via IVIS Spectrum μCT (Perkin Elmer Inc.).

4.1.3 LPS Induced Acute Neutrophilic Inflammation

5-week-old female C57BL/6 littermates (Jackson Labs) were maintained in a pathogen-free facility, given sterile water and food ad libitum. Mice were treated with either saline or 100 μg of LPS then for the fluorescent uptake study Nano-in-Micro formulation was delivered 2 h later and for the Nex20/TIIA study 1 h after injection. The time for Nano-in-Micro injection was shortened since at 2 h post LPS mice had significant difficulty in aspirating the particle formulation. Mice used for IVIS were given a low alfalfa feed diet to reduce fluorescence background.

4.1.4 Flow Cytometry

Single cell suspensions were prepared using a gentleMACS tissue dissociator (Miltenyi) with 1 mg/mL of Collagenase D (Roche) and 0.1 mg/mL DNase I (Roche) in Opti-MEM (ThermoFisher), then strained through a 40 μm cell strainer. Red blood cells (RBC) were lysed using 1x RBC Lysis Buffer (eBioscience). The single cell suspension was then washed and stained with Zombie Aqua (BioLegend), incubated with Fc Block (BioLegend) then with fluorochrome-conjugated antibodies (BioLegend unless noted; clone used), and fixed with Cytofix (BD Bioscience). Antibodies used for the experiment in Figure 23 were: Ly-6G-BV711 (1A8), CD45-BV605 (30-F11), SiglecF-PE (BD Bioscience; E50-2440), CD11c-APC/Fire750 (N418), F4/80-PE/Dazzle™ 594 (BM8), CD11b-PE/Cy7 (M1/70). Cells were collected on an untreated littermate to set the gates with noise below 1% by FMOs (fluorescence minus one). The gating scheme for this experiment is illustrated in Figure 17; data were acquired on a BD LSR Fortessa flow

cytometer. For Figure 24-Figure 27, cells were stained with FC block and Zombie live/dead dye for 10 minutes on ice, followed by staining for 15 minutes on ice with antibodies against the following markers: CD45, Ly6G, Ly6C, MHCII, CD11b, F4/80, CD206, CD11c, SiglecF, and CD63. Cells were washed with PBS-EDTA (250 nM), fixed with Lyse/Fix PhosFlow reagent (BD Biosciences) and acquired on a FACS LSRII (BD Biosciences) and on a Cytoflex S (Bechman Coulter). PMNs were gated as CD45+, Ly6G+ and CD11b+ cells while macrophages were identified as CD45+, F4/80+, MHCII+, Ly6G- cells. Compensation and data analyses for all flow experiments were performed using FlowJo (TreeStar).

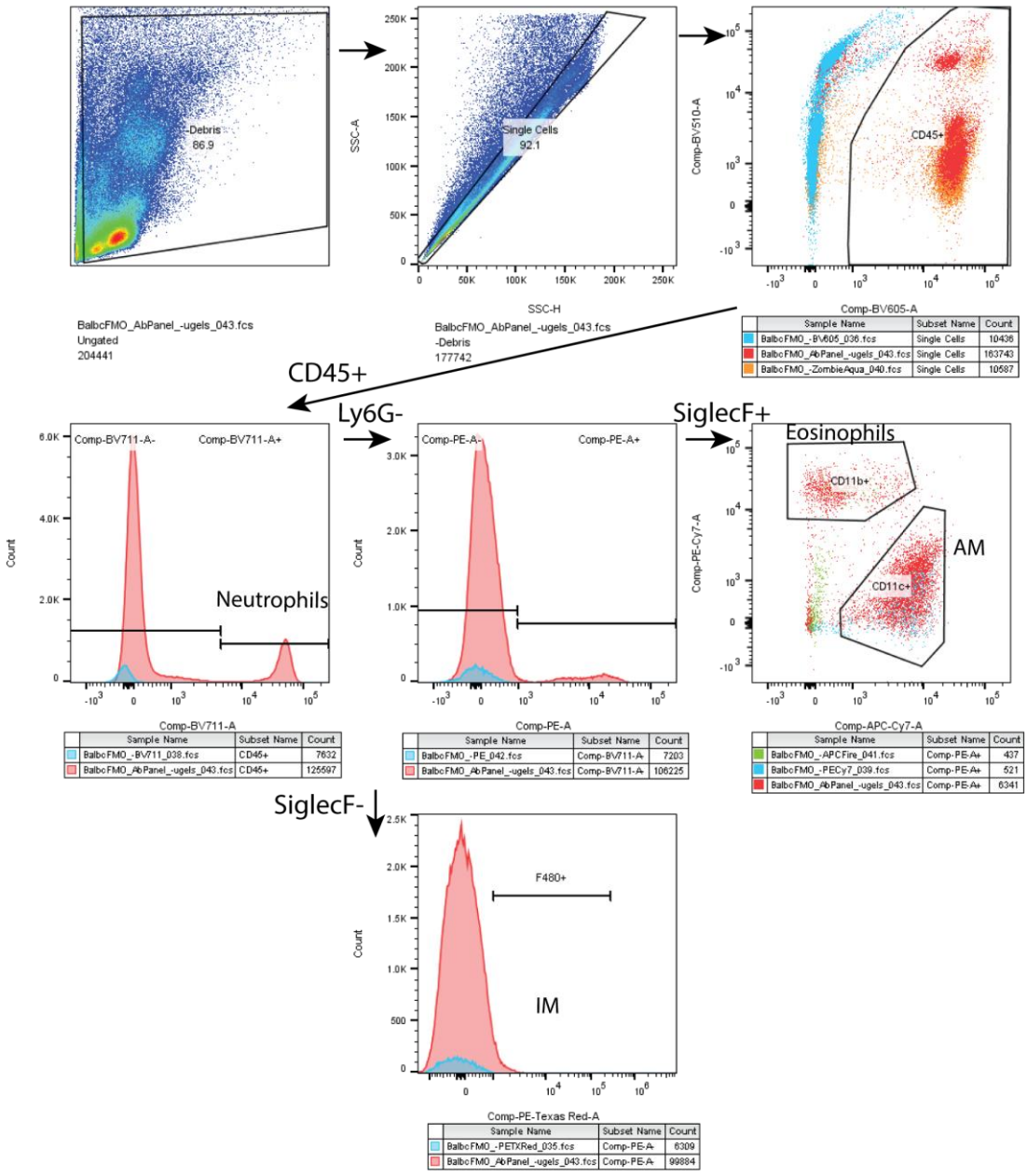

Figure 17: *in vivo* LSR Fortessa Gating Schematic Gating and FMOs for the flow panel. After gating for singlets cells were gated on CD45+ and although Zombie Violet live/dead fixable dye was included in the panel, due to the few number of cells in the final eosinophil and alveolar macrophage gates, the dead cells were included in the analysis. The CD45+ population was then bisected on Ly6G, with Ly6G+ labeled as neutrophils. The Ly6G- group was then bisected for SiglecF, the SiglecF+ population was then gated on CD11c and CD11b for eosinophils (CD11b+CD11c-) and alveolar macrophages (CD11b-CD11c+). The SiglecF- population was then gated for the macrophage marker F4/80.

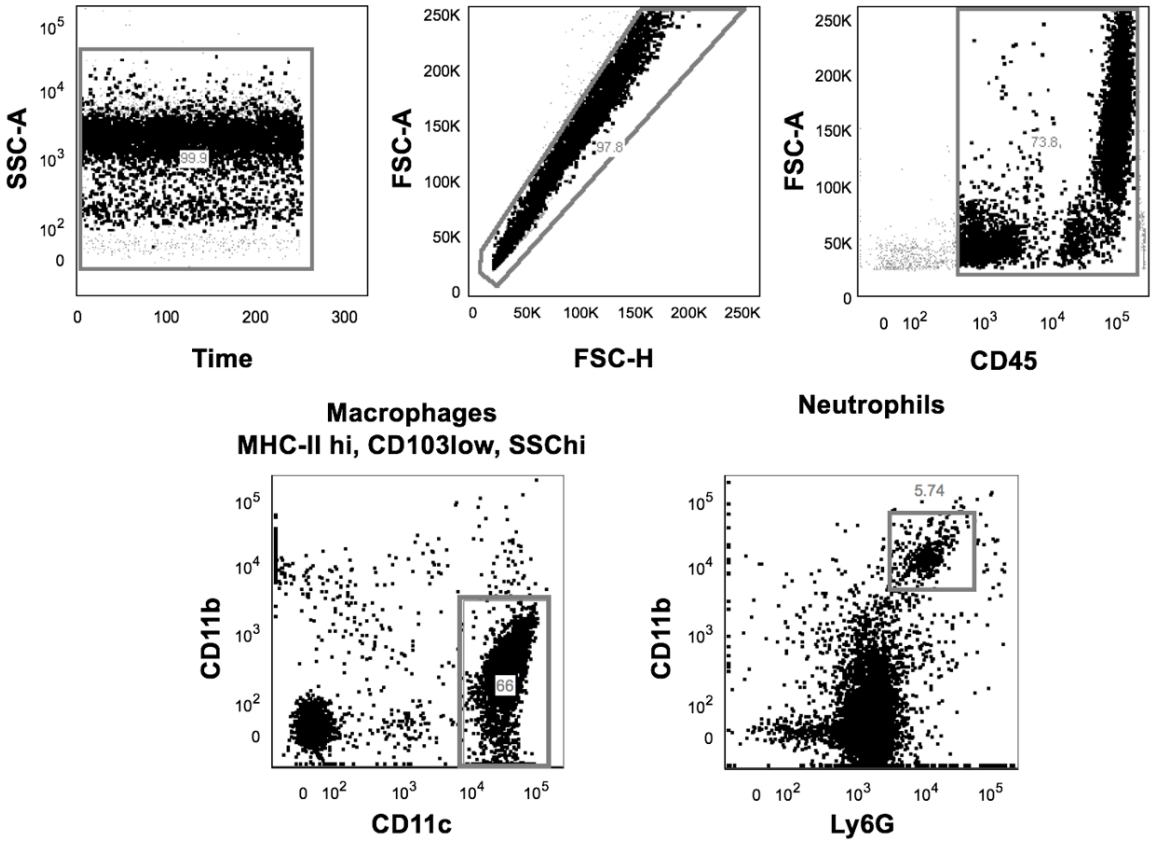

Figure 18: PMN and Macrophage Flow Cytometry Gating Scheme After singlet gating, PMNs were gated as CD45+Ly6G_CD11b+ while macrophages were gated as CD45+F4/80+MHCII+Ly6G-

4.1.5 Extracellular vesicles (EV) analysis

EVs were isolated from the BAL using bead-based pulldown with Annexin V as per manufacturer's protocol (SBI). Isolated EVs were stained with the EV marker ExoFITC (SBI) and anti-mouse neutrophil elastase (R&D systems). EVs were analyzed by flow cytometry on a Cytoflex S (Beckman Coulter).

4.1.6 ELISA

NE and MMP9 concentrations were measured in the BAL of mice as per manufacturer's protocol (R&D Systems). Cytokines from the plasma and BAL were

measured using a multiplex platform following manufacturer's protocol (Meso Scale Diagnostic, V-PLEX mouse cytokines – 19 analytes).

4.1.7 Statistical Analysis

Data were analyzed using GraphPad Prism with a Shapiro-Wilk test for normality (α=0.05). A one-way Anova ($\alpha = 0.05$) with post-hoc Tukey's test with an adjusted P value for multiple comparisons, or a two-way Anova ($\alpha = 0.05$) with Sidak post hoc analysis was used with parametric data. Where applicable, Kruskal-Wallis ($\alpha = 0.05$) with Dunn's test was used for nonparametric data.

Results

4.1.8 Microgels Begin Clearing Within 24h in Naïve Mice in vivo

Based on our *in vitro* data, the degradation rate of the elastase-responsive microgels in CF airway fluid would occur within a short time frame (i.e., 30 minutes). Since the 20% w/v microgels had both the fastest and the highest percentage of RAW 264.7 macrophages positive for the microparticles *in vitro*, Figure 12, they were used to investigate how quickly the microgels would be cleared from the lungs *in vivo*, and to further understand how fast the protease-specific peptide crosslinked microgels must degrade to release their nanoparticles before being cleared. The trypsin-responsive crosslinker was selected because trypsin is a protease primarily found in the digestive system and should not be present in the lung, allowing us to primarily study clearance rather than degradation. Balb/c mice were treated with saline or 20% w/v trypsin-responsive Nano-in-Micro particles by a Penn-Century MicroSprayer aerosolizer, which demonstrated that microgels were present in all 5 lobes of the lungs as well as some interaction with SiglecF+ phagocytes (eosinophils or alveolar macrophages) confirmed by confocal microscopy, Figure 19.

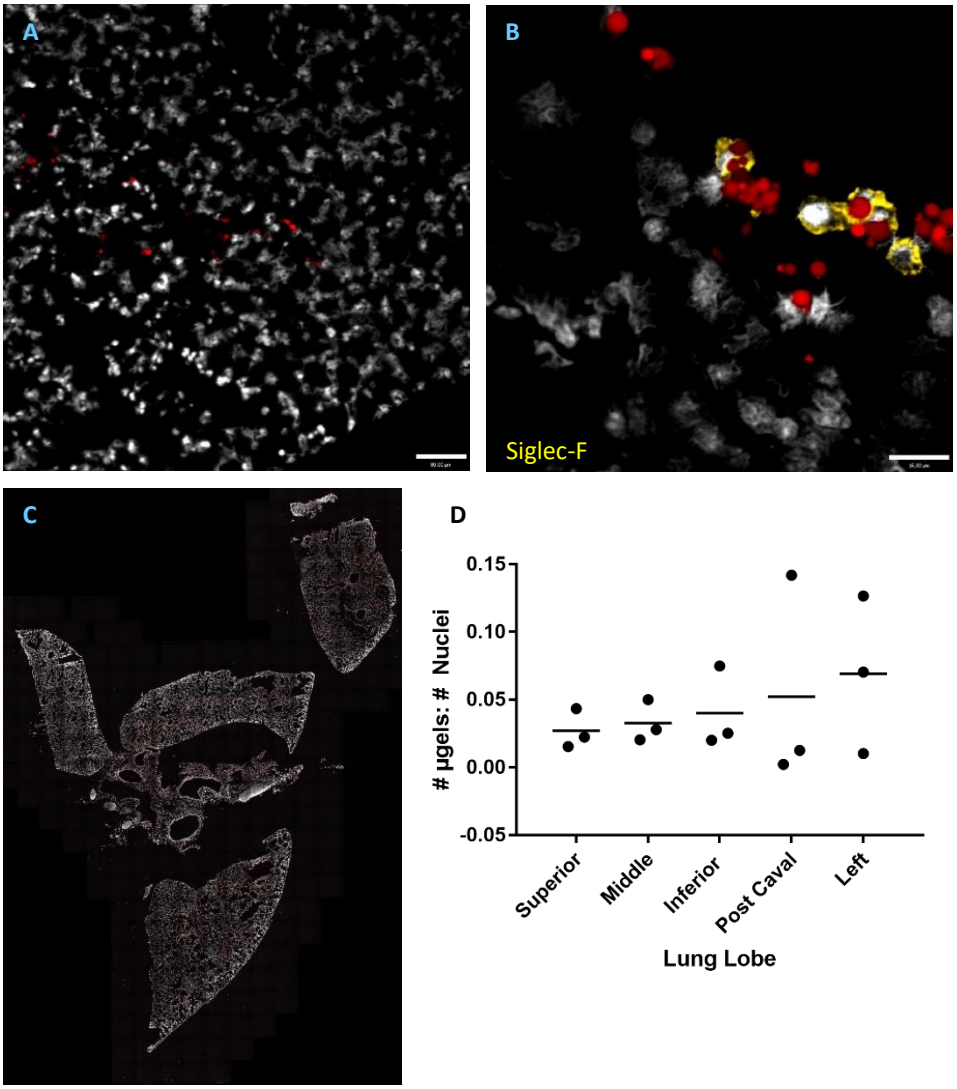

Figure 19: Microgel Deposition in naïve Mouse Lungs Microgels were instilled in mice lungs, lungs were harvested immediately and frozen for cryosectioning. (A) 10x image of a DAPI microgel section of the lobes (scale bar 80 µm) B) SiglecF stained cells within a lung section (scale bar 16 µm) and (C) representative full lung section. (D) Ratio of microgels present to nuclei within each lobe, measured by Volocity, each point is an individual mouse and shows deposition of microgels in each of the lobes.

To determine how quickly the microgel formulations would begin to clear during normal non-degradative conditions, 20% w/v trypsin-responsive microgels, 20% w/v PEG (non-enzymatically-degradable) microgels, or saline controls were delivered to the lungs of naïve mice via aerosolizer. The lungs were then excised at 0.5, 6, and 24 hours, and the radiant efficiency of the whole lung was measured using IVIS. Fluorescence intensity of

the microgel decreased with time but was still visible at 6 hours after injection, representative images in Figure 20 and all IVIS images along with preliminary flow data in Figure 21. We expect that the levels of proteases present in the lungs were relatively low given that the mice were naïve, and thus the measured decrease in fluorescence should not be due to enzymatic degradation of the peptide backbone on the microgels, which was confirmed by the similar rates of clearance for both the enzymatically- and non-enzymatically degradable Nano-in-Micro formulations. This suggests that without relevant proteases to degrade the microgels, they are most likely cleared by either macrophage phagocytosis or mucociliary clearance.

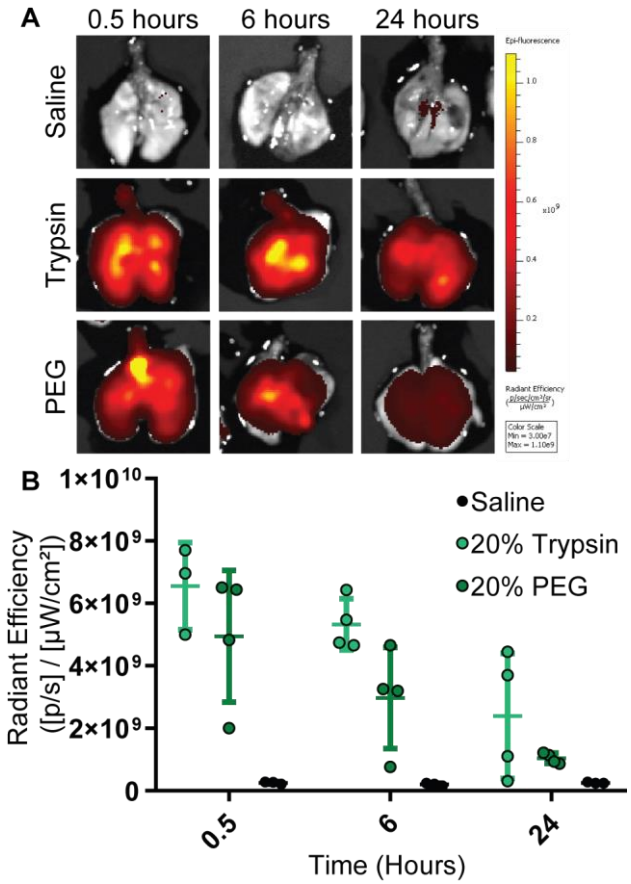

Figure 20: 20% w/v Trypsin- and PEG- Microgel Clearance in Naïve Mice (A) Representative IVIS Spectrum µCT images for background control (saline), trypsin-responsive and non-enzymatically degradable PEG DyLight 650 labeled Nano-in-Micro particles at 0.5, 6, and 24 hours after instillation (n = 3 - 4). (B) DyLight 650 labeled Nano-in-Micro fluorescence showing a similar decrease in measured radiant efficiency between both formulations over time. Kruskal-Wallis with Dunn's multiple comparison test within each time point is not statistically significant, $\alpha < 0.01$.

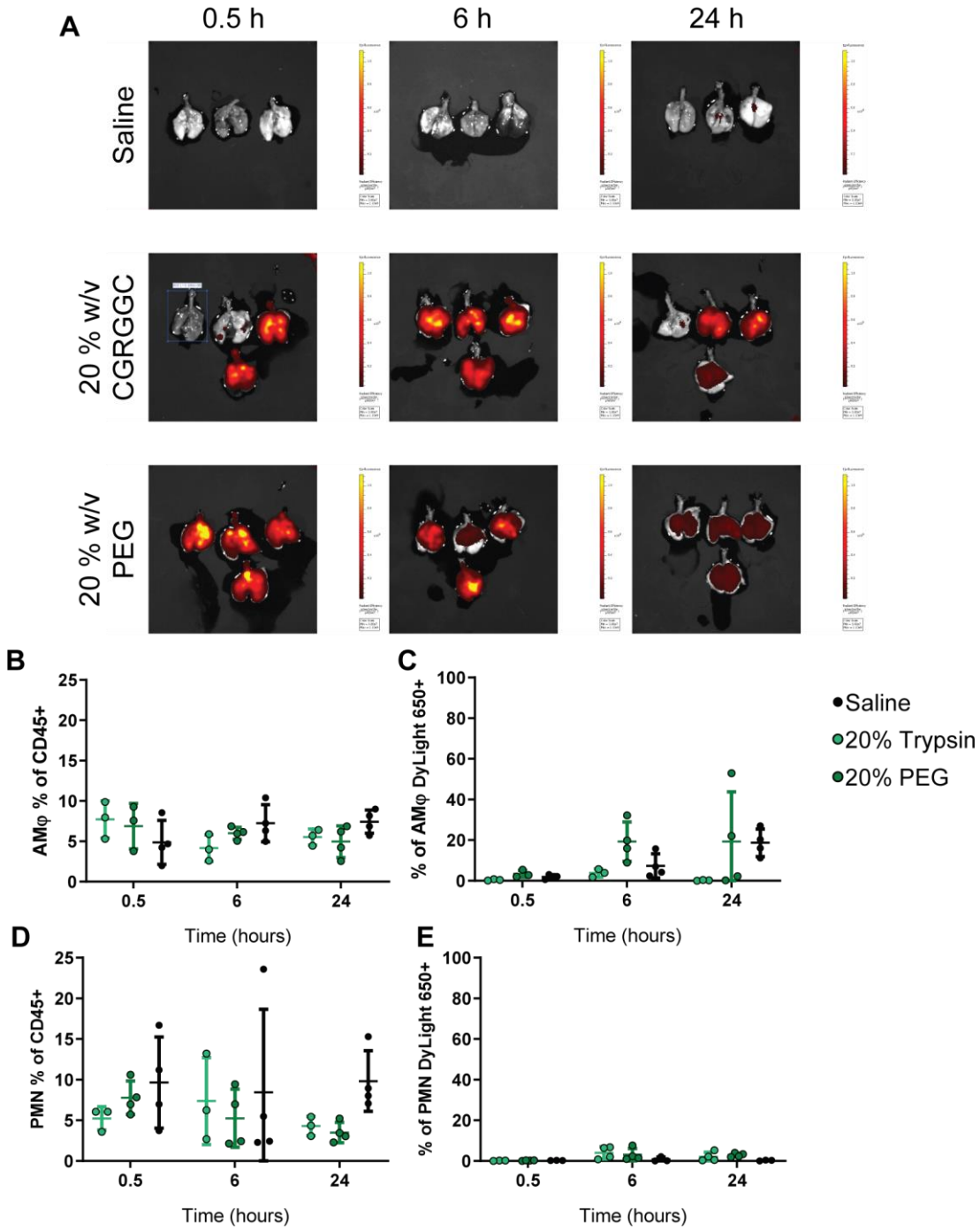

Figure 21: IVIS and Flow for 20% w/v CGRGGC and PEG Nano-in-Micro (A) All IVIS images for 20% Trypsin and 20% PEG microgel lung delivery, the lung from 0.5h trypsin with an ROI box was a sample injected into the esophagus and removed from the data sets (B) Preliminary flow data for Alveolar Macrophages and Neutrophils showing some uptake in individual mice but no group significance.

To determine whether the trends in macrophage phagocytosis *in vitro* were replicated *in vivo*, 20 and 30% w/v trypsin-responsive Nano-in-Micro particles were delivered via aerosolizer to naïve mouse lungs. Next, lungs were excised at 0.5, 6, and 24 hours and imaged with IVIS. Similar trends of radiant efficiency were seen between the 20 and 30% w/v formulations, Figure 22. Curiously, we observed the overall intensity of radiant efficiency was lower relative to Figure 20 (mean over $4x10^9$ at 0.5 hours), which may have been due to delivery variability issues with the aerosolizer. However, clearance remained similar within formulations. Fluorescence for both clearance experiments, Figure 20 and Figure 22, was maintained at 6 hours, showing that microgels for use with disease states should degrade within a short time frame (< 6 hours) for the nanoparticle cargo to be effectively released. Without a perceivable difference observed between the formulations a 20% w/v formulation may be all that is needed for the microgel to provide efficient, delivery within the short time frame in which the microgels can be degraded to release their nanoparticle cargo; this reduces the amount of polymer to fabricate the Nano-in-Microgels.

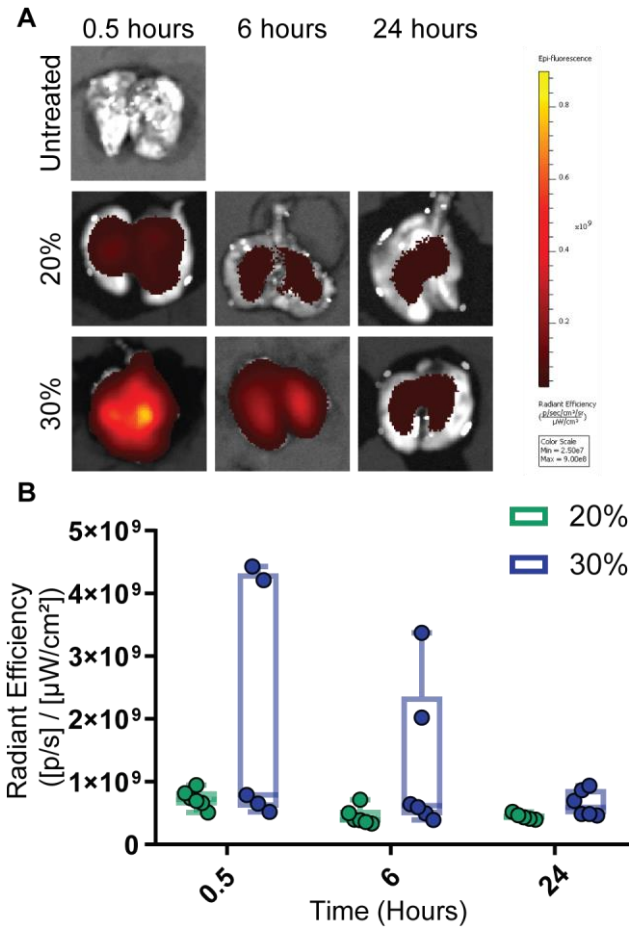

Figure 22: 20, 30% w/v Trypsin-Responsive Microgel Clearance in Naïve Mice (A) Representative IVIS Spectrum images for radiant background efficiency (untreated), 20 and 30% w/v trypsin-responsive Nano-in-Micro particles at 0, 6, and 24 hours after treatment. (B) Measured radiant efficiency of delivered microgel fluorescence in the excised lungs.

4.1.9 Limited Phagocytosis in vivo Within 1 Hour of Administration

To determine whether the microgels with different peptide crosslinkers were phagocytosed differently, a 1:1 ratio of trypsin-responsive microgels and elastase-responsive microgels (labeled with DyLight 650 and DyLight 488, respectively) were loaded with Blue Fluospheres were delivered to the airways of mice. Microgels were administered with the aerosolizer (PC) or by oropharyngeal aspiration between Balb/c littermates. Additionally, microgels were delivered by oropharyngeal aspiration to

C57BL/6 mice from two age group (5-6 and 16-17-week old) since this strain is often used in LPS models of neutrophilic infiltration. One hour after delivery, and presumably after the elastase-responsive microgel would begin to degrade (Figure 12), the mice were sacrificed, the lungs collected, and digested into single cell suspensions. Stained samples were then run to determine the phagocytic cells positive for the different microgel formulations. Cell populations were defined as follows: 1) polymorphonuclear neutrophils (PMN): CD45+Ly6G+, 2) alveolar macrophages (AM): CD45+Ly6G-SiglecF+CD11c+CD11b-, 3) eosinophils (Eo): CD45+Ly6G-SiglecF+CD11c-CD11b+, and 4) non-alveolar F4/80+ macrophages (Mφ): CD45+Ly6G-SiglecF-F4/80+. The MicroSprayer appears to deliver microgels within the target area near alveolar macrophages, Figure 19; however, the extent and dose with which these particles reach the lower airways may be low and with oropharyngeal aspirations may be lower still since the added velocity added by the MicroSprayer is absent. Additionally, the F4/80+ macrophage populations can include both non-alveolar macrophages as well as interstitial macrophages [176] that may or may not come in contact with the microgel formulations, skewing the percentages of populations positive for microgels low. Statistical analysis comparisons were within species for each cell type.

The neutrophil populations for the MicroSprayer and oropharyngeal aspiration Balb/c delivery methods were significantly different and the alveolar macrophage population between the two C57BL/6 groups were significantly different using a two-way Anova ($\alpha = 0.01$) with Sidak post hoc test, Figure 23A. While the microgel+ populations within each of the cell populations have median values below 5% for each type, (Figure 23B-C), the elastase-responsive group has a few between 5-10%; the grey dashed line

marks the 1% threshold used to set the gates on FMOs. Due to the low number of cells within each of the sub-populations the nanoparticles (Figure 23D) were gated directly off their parent cell population rather than from the microgel positive populations with only the Balb/c F4/80+ macrophage populations showing cells positive for nanoparticles.

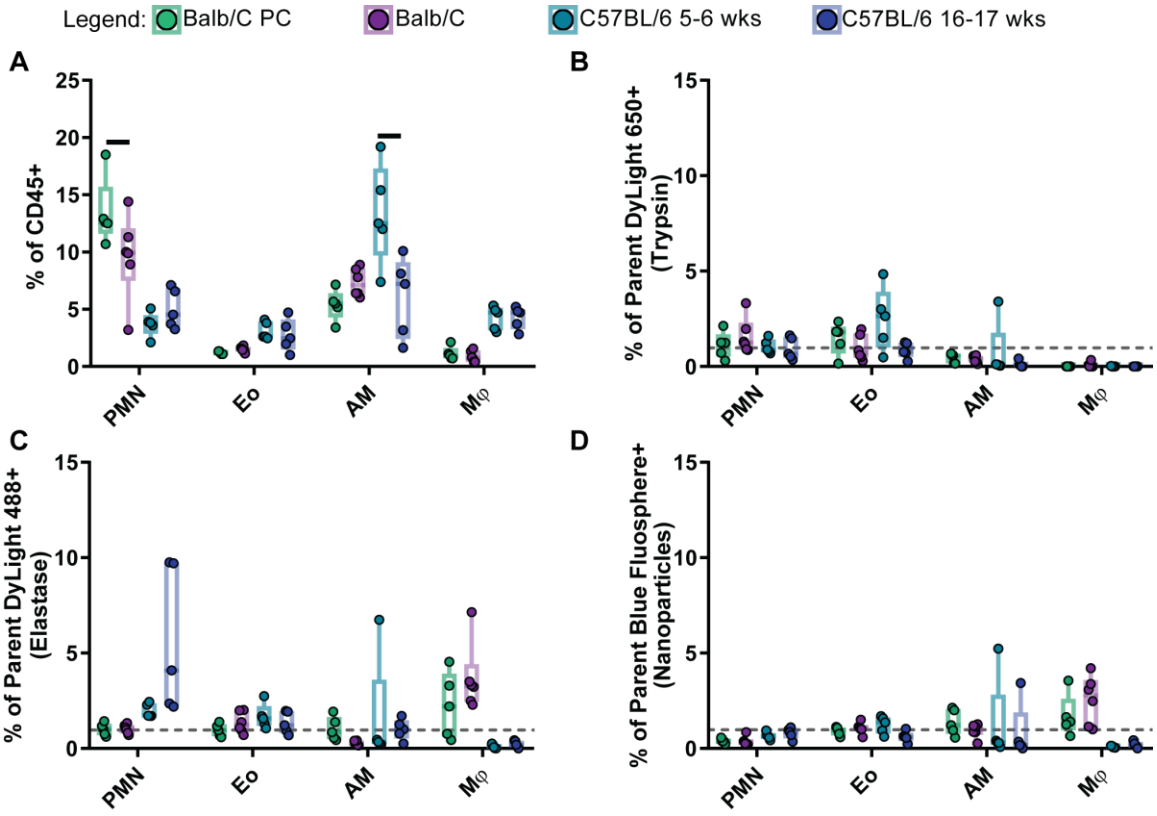

Figure 23: Naïve Balb/c and C57/BL6 Uptake of Nano-in-Micro Particles (A) Neutrophil, eosinophil, alveolar macrophage, and F4/80+ macrophage populations for microgels delivered to Balb/c by aerosolizer (green), Balb/c by oropharyngeal aspiration (purple), 5-6-week-old C57BL/6 (light blue), and 16-17-week-old C57BL/6 (dark blue) mice by oropharyngeal aspiration; two-way Anova ($\alpha = 0.01$) with Sidak post hoc. Percentage of neutrophils (PMN; CD45+Ly6G+), eosinophils (EO; CD45+Ly6G-SiglecF+CD11c-CD11b+), alveolar macrophages (AM; CD45+Ly6G-SiglecF+CD11c+CD11b-), and F4/80 macrophages (Mφ; CD45+Ly6G-SiglecF-F4/80+) positive for (B) trypsin-responsive microgels and (C) elastase-responsive microgels or (D) Blue Fluospheres; Mann-Whitney ($\alpha = 0.01$). Grey dashed line marks the 1% threshold used to set the gates on FMOs.

While particle size is an important factor for phagocytosis and endocytosis, recent work looking at the relationship between particle elasticity and cellular uptake has shown that softer particles are often more difficult for cells to consume. This is because particle deformation leads to a greater extent of spreading between the elastic particle and the cell; specifically, phagocytosis by immune cells for particles in the softer (kPa) range have slower uptake than stiffer (MPa) particles [76,159,177]. We observed that with the 20% w/v trypsin- and elastase-responsive microgels, there was limited phagocytosis in the first hour by neutrophils, eosinophils, alveolar macrophages, and F4/80+ macrophages for both Balb/c and C57BL/6 mice regardless of delivery method (aerosolizer vs. oropharyngeal aspiration); we believe the combined size and softness of the microgels influenced this observation.

Furthermore, the *in vitro* elastase-responsive microgels degraded in CF patient sputum within 30 minutes, Figure 12 and Figure 16, which suggested that the elastase-responsive microgels should degrade and release nanoparticles before most of the microgels are cleared from diseased lungs. This microgel phagocytosis and clearance from Figure 19-Figure 23 was observed in naïve animals; however, under severe disease burdens (such as asthma, COPD, and CF) there is reduced phagocytic ability of these innate cells [178–181], which may create a longer window for the microgels to degrade—releasing their cargo.

4.1.10 Nano-in-Micro in an Acute LPS-Induced Lung Injury Model

We tested the efficacy of the multi-stage particle system in an LPS-induced acute inflammation mouse model. Using microgels labeled with a near IR dye, DyLight 650, loaded with representative Blue (365/415) 100 nm Fluorosphere nanoparticles, the Nano-

in-Micro were delivered intratracheally to mice treated with saline or LPS. The radiant efficiency in the excised lungs, corresponding to the fluorescence intensity of the microgel dye at 1, 6, and 22 hours after Nano-in-Micro delivery (3, 8, 24 hours post LPS), showed a significant reduction at 6 hour post Nano-in-Micro delivery, Figure 24A, revealing a faster microgel degradation in mice treated with LPS compared to the saline treated group. Concurrent with the observed microgel degradation, we observed reduced activation of blood PMNs over time (surface CD11b, Figure 24B), PMN recruitment to the airways with subsequent release of the neutrophil elastase (NE)-rich granules (surface CD63), and increased amount of the soluble neutrophil elastase in the bronchoalveolar lavage (BAL), Figure 24C-D. Together, these data suggest that the short-term clearance of the microgels during the LPS treatment is preceded by and dependent upon the degradation of the elastase-responsive peptides crosslinking the microgel. Notably, the subpopulation of LPS treated BAL PMNs double positive for both the Microgel and Nanoparticles showed increased surface CD63 expression, Figure 24E, suggesting that fusion to the plasma membrane of NE-rich granules and release of their content in the extracellular milieu is concomitant with increased uptake of soluble material. Lastly, analysis of the distribution of nanoparticles and microgel uptake by both, PMNs and macrophages, showed that airway PMNs, at 1 and 6 hour post-delivery, were primarily positive for nanoparticles alone, suggesting that our microgels were degraded, allowing the PMNs to access and endocytose the nanoparticles, Figure 24F. However, at 22 hours PMNs in the BAL and lung lysate showed equal uptake of both, the microgel and the nanoparticles, suggesting clearance of the remnant microresidues of the Nano-in-Micro system. As expected, BAL and lung lysate macrophages quickly began to phagocytose the Nano-in-Micro system. Notably, the

pattern of particle uptake by macrophages clearly differed from that of PMNs; the shift to nanoparticle alone at the later time-points may be due to either digestion of the microgels and subsequent intracellular release of the nanoparticles or to degradation of the dye labeling the microgels in the lower endosomal pH.

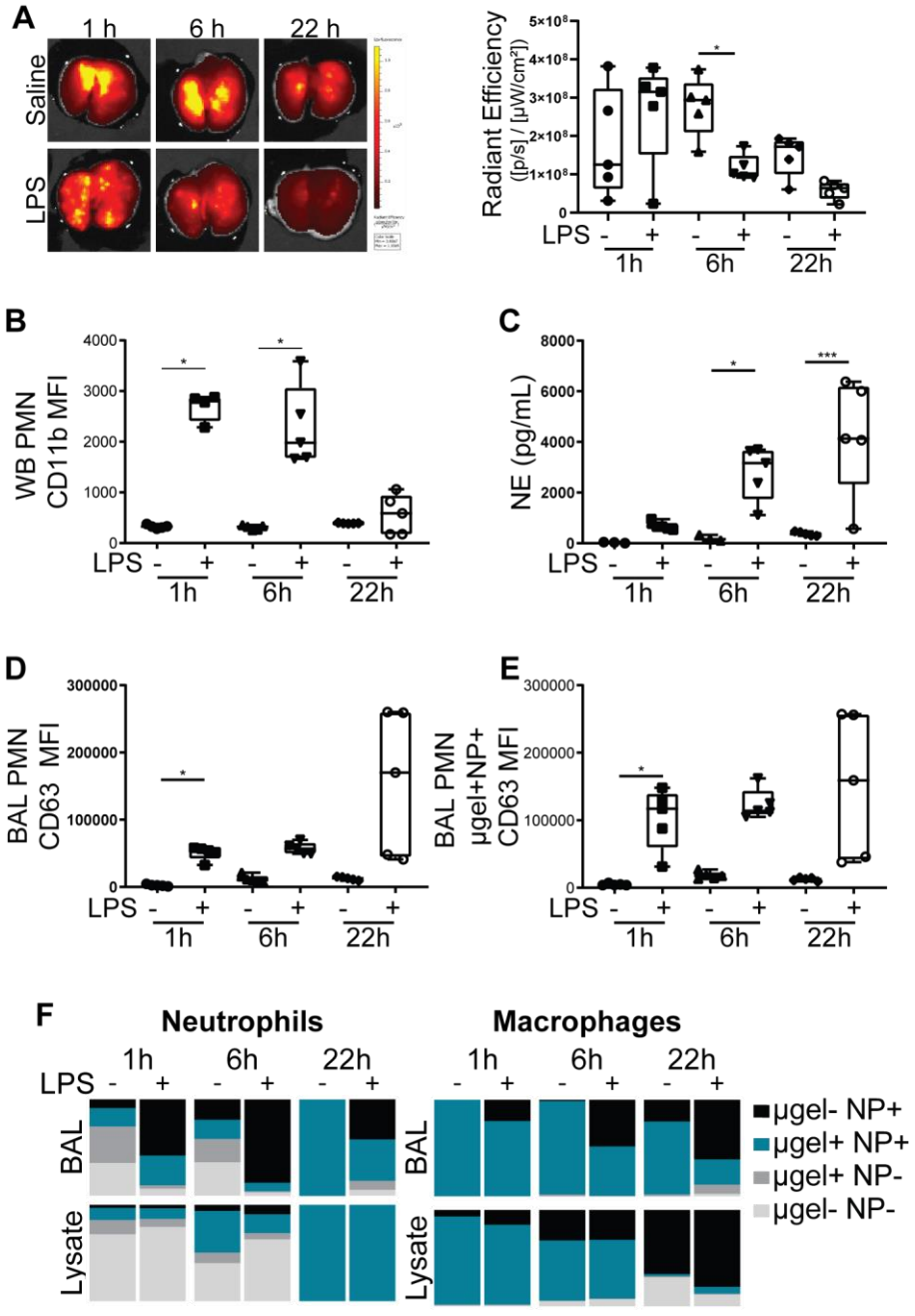

Figure 24: Fluorescent Nano-in-Micro in an Acute Neutrophilic Inflammation Model (A) Representative IVIS images of excised mouse lungs with corresponding measures of radiant efficiency for 1, 6, and 22 hours (C) Increase in BAL elastase levels for the LPS

treated mice. (D) Increased CD63 expression on BAL PMNs and increased (E) CD63 expression on Nano-in-Micro positive BAL PMNs (F) Percentage of BAL Neutrophils or Macrophages positive for nanoparticle only (black), Nano-in-Micro (blue), microgel only (dark grey), or negative for both (light grey). *$p < 0.05$, ** $p < 0.01$, *** $p < 0.001$ within time points indicated.

4.1.11 Delivering Therapeutics via Nano-in-Micro

To determine whether the Nano-in-Micro system could not only effectively deliver nanoparticles to PMNs but also modulate inflammation, PLGA nanoparticles loaded with either Nexinhib20 and DiR (Nex20) or Tanshinone IIA and DiR (TIIA) were encapsulated into the 20% w/v elastase-responsive microgels. DiR is a near IR fluorescent dye, acting as a tracer for nanoparticle uptake, but upon release from the nanoparticle can potentially label the cell's plasma membrane. Additionally, to assess if the particle formulation itself influenced the immune response, additional control groups for both saline and LPS treated mice were treated with a control DiR-only PLGA nanoparticles inside the elastase-responsive microgel. The effects of the delivery of the therapeutics by the Nano-in-Micro system on systemic PMN responses were assessed in the blood (WB), bone marrow (BM), lung bronchioalveolar lavage fluid (BAL), and lung tissue lysate.

While there was no detectable sign of neutrophilia or neutropenia in the blood relative to the saline control, the TIIA Nano-in-Micro treatment group did have statistically lower counts than the LPS treatment group and, while not statistically significant, the mean PMN TIIA count is 3-fold lower than the saline, Figure 25A. However, in the bone marrow, Nex20 and TIIA Nano-in-Micro treatment increased PMN bone marrow levels to those of the saline treated group, Figure 25B. Additionally, there appeared to be no therapeutic effects on the expression of inflammatory activation markers, Siglec-F and CD11b, for the LPS treated mice bone marrow PMNs, Figure 26.

Remarkably, unlike TIIA, delivery of Nex20 reduced the percentage and mean total number of PMNs in the lysate and BAL compared to the LPS treated control group, by 4.3- and 13-fold respectively, suggesting successful modulation of inflammation by delivery of the drug Nex20 to these PMNs by the Nano-in-Micro, Figure 25C-D. Neither the blood nor bone marrow PMNs were positive for the fluorescently labeled nanoparticle, DiR, Figure 25E-F; however, confirming the Nex20 results, BAL and lysate PMNs treated with Nano-in-Micro formulations were positive for the DiR dye suggesting endocytosis of the PLGA nanoparticles (control and therapeutic) by airway PMNs, Figure 25G-H. The modulation by Nex20 Nano-in-Micro seen in the bone marrow PMN counts together with the normal blood counts, point towards physiological feedback regulation of hematopoiesis and highlight the specificity of the delivery system in targeting only the desired organ and avoiding off-target systemic effects.

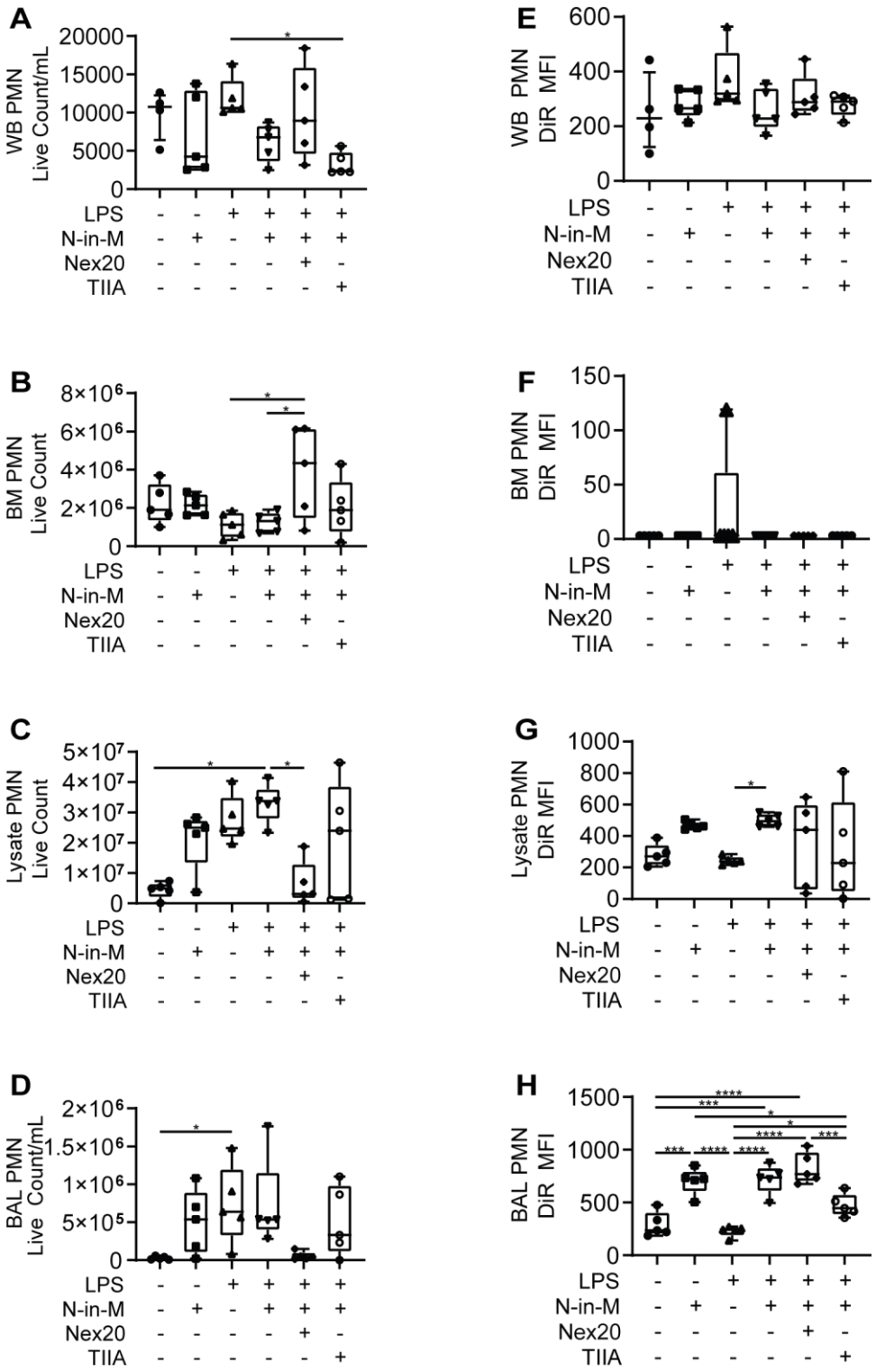

Figure 25: Nex20 and TIIA Nano-in-Micro PMN counts and DiR MFI (A) Blood PMN and (B) bone marrow PMN counts had no detectable signs of neutrophilia or neutropenia, while in the (C) lysate and (D) BAL the expected increase in PMNs with LPS treatment were abrogated in the Nex20 but not the TIIA treatment groups. As expected with site-specific delivery, the DiR nanoparticle fluorescence was not picked up by PMNs in the (E)

blood or (F) bone marrow but was visible in the (G) lysate and (H) BAL. *p < 0.05, ** p < 0.01, *** p < 0.001, **** p < 0.0001 between groups indicated.

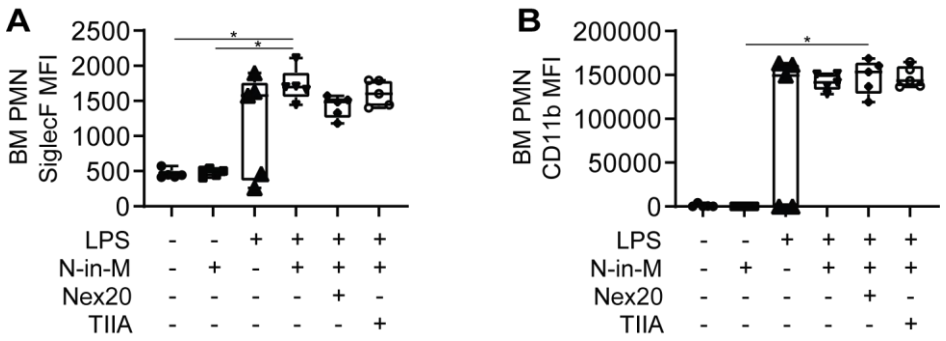

Figure 26: Bone Marrow PMN SiglecF and CD11b Expression Increased expression of inflammatory markers (A) SiglecF and (B) CD11b on bone marrow PMNs in LPS treated groups. *p < 0.05 between groups indicated.

To determine whether delivery of Nex20 and TIIA Nano-in-Micro could influence not only PMN numbers, but also their phenotype and function, active release of NE-rich granules was measured by flow cytometry on BAL PMNs. Most strikingly, concomitant with increased nanoparticle uptake by PMNs, Figure 25H, surface CD63 expression on BAL PMNs, reflective of NE release, was significantly lower for both therapeutic formulation than all other treatment groups, Figure 27A. Notably the Nex20 Nano-in-Micro were also significantly lower than the saline treatment group. Blood PMN CD63 expression for both therapeutic treatments appeared to have similar expressions as the saline group, Figure 27B. However, the lysate PMNs for TIIA had increased CD63 expression—this subset also had increased SiglecF expression, Figure 27B-C. Despite similar PMN recruitment observed between the LPS alone and the control DiR PLGA Nano-in-Micro, the control N-in-M delivered to LPS treated mice activated the airway PMNs, resulting in a significant increase of both MMP9 and NE in the BAL, a respective

2.7- and 28-fold increase relative to the saline treatment group, and a respective 1.3- and 5-fold, compared to the LPS alone group. However, the delivery of Nex20 Nano-in-Micro abrogated this response with the levels of NE and MMP9 not significantly different from the saline control group. Unfortunately, this response was not observed for the TIIA which appears in line with the increased CD63 expression of the lysate PMNs. Additional tissue staining showed that delivery of Nex20 by the Nano-in-Micro system was able to reduce myeloperoxidase (MPO) positive cells, most likely PMNs, to the levels of the saline treated group; however, TIIA retained MPO activity. TIIA has previously been shown to modulate the proinflammatory immune response after injury for several mouse models (acute kidney injury, rheumatoid arthritis, LPS and smoke lung injury) by modulating the neutrophilic response, lowering MPO activity, and preventing epithelial damage from oxidative stress [182–184]; however, it has been shown to function in a dose dependent manner [182] and while the TIIA Nano-in-Micro appears to alter the LPS induced neutrophilic inflammation response the low encapsulation efficiency of TIIA in the PLGA may result in too low a dose to have effective reduction in inflammation.

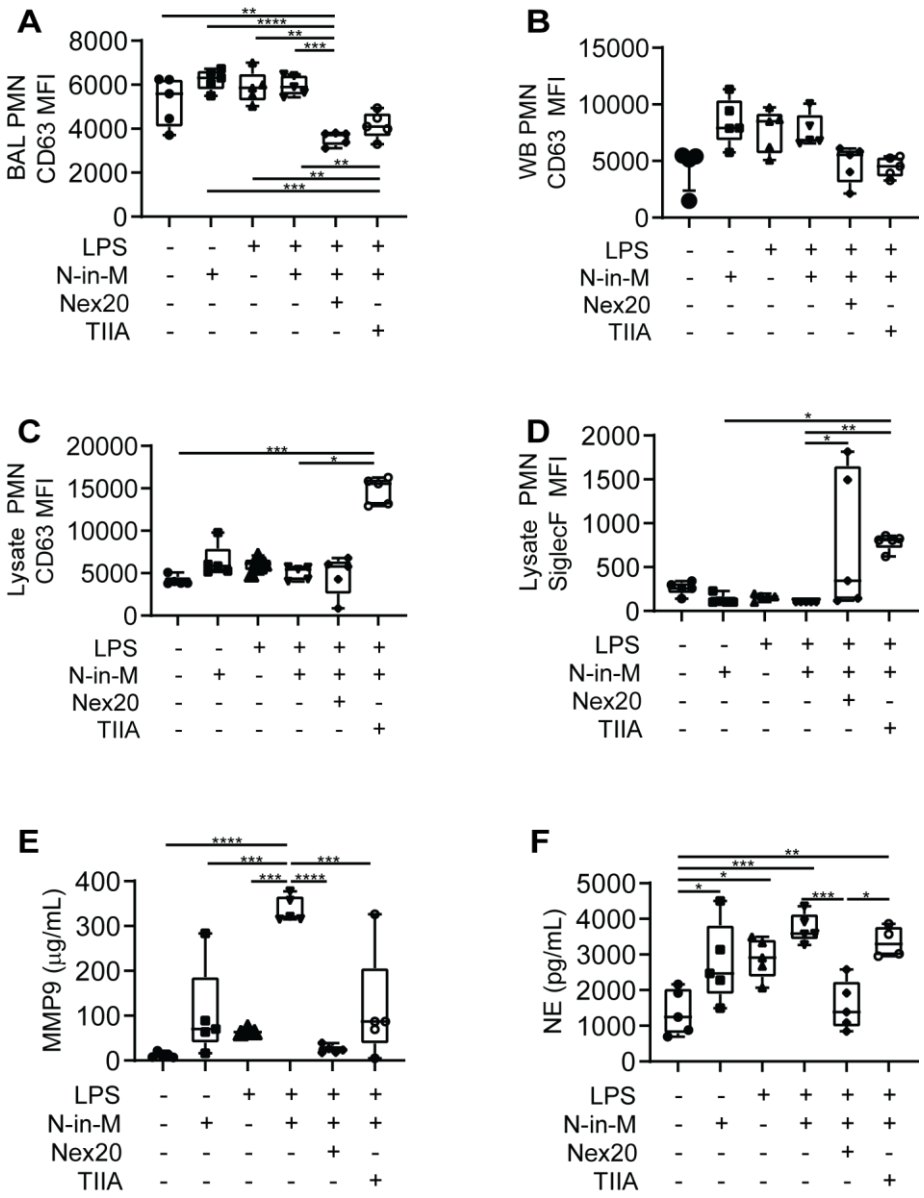

Figure 27: Nex20, TIIA Nano-in-Micro BAL and Lysate PMN Phenotype Modulation (A) CD63 expression on BAL PMNs is significantly decreased for both Nex20 and TIIA treatment groups (B) Blood PMN CD63 expression appear to be decreasing (C) however, lysate CD63 expression is higher for the TIIA treatment group. (D) SiglecF expression of lysate PMNs is increased for both treatment groups. Nex20 Nano-in-Micro treatment is able to reduce the (E) soluble MMP9 and (F) soluble NE BAL levels. *$p < 0.05$, ** $p < 0.01$, *** $p < 0.001$, **** $p < 0.0001$ between groups indicated.

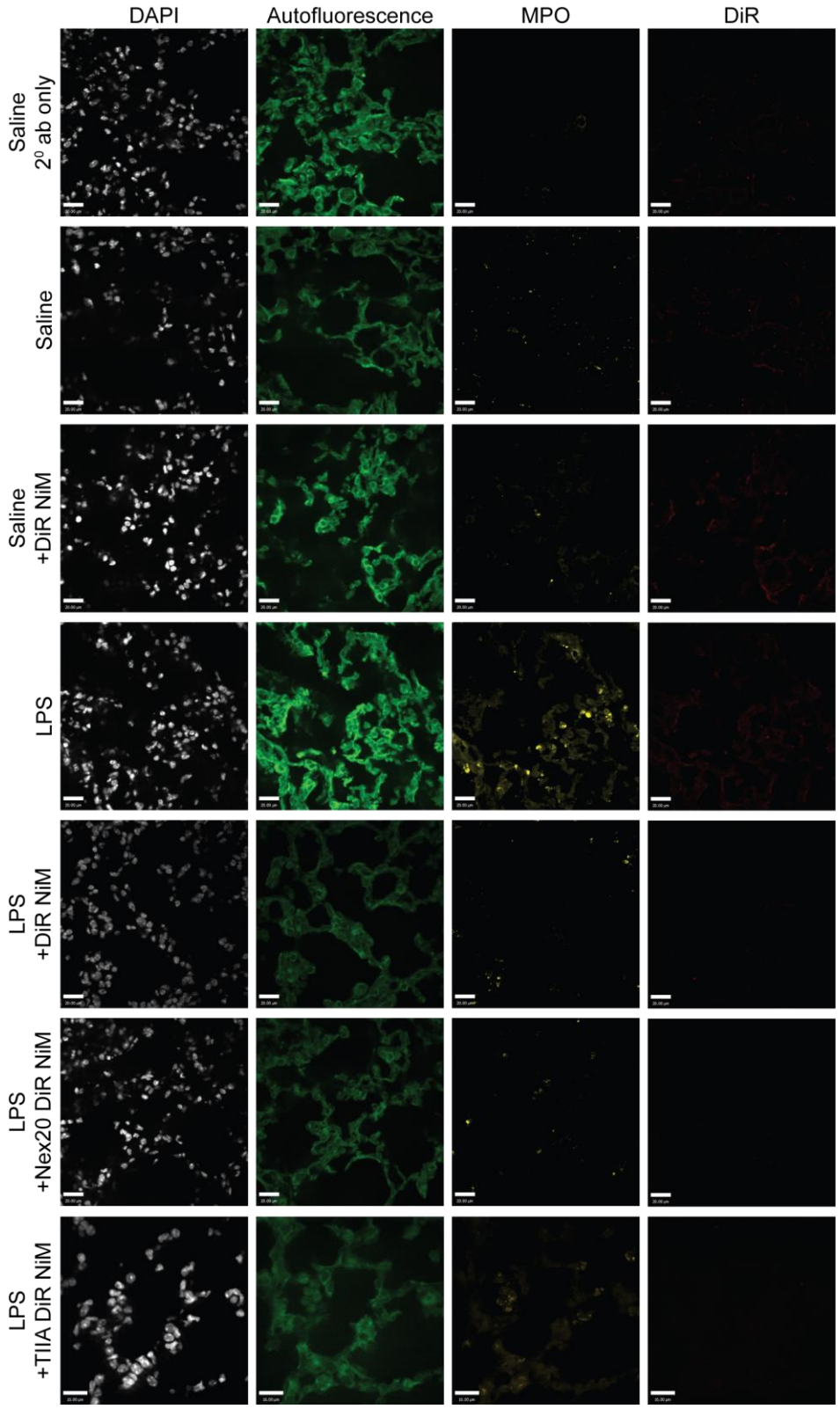

Figure 28: MPO Tissue Staining Treatment with Nex20 Nano-in-Micro show decreased presence of myeloperoxidase (MPO) staining in tissue sections relative to the LPS and TIIA Nano-in-Micro treatment groups, scale bar = 20 μm, linearly contrasted for clarity.

As the TIIA Nano-in-Micro failed to reduce the soluble MMP9 and NE levels, it was removed from further BAL cytokine analysis. Surface elastase expression of extracellular vesicles has been shown to be integral to the PMN hyperexocytic inflammation process [185]. BAL extracellular vesicle surface elastase levels showed increased levels in the LPS and control Nano-in-Micro group which were lowered by Nex20 Nano-in-Micro treatment, Figure 29A. Nex20 Nano-in-Micro treatment was able to reduce important chemoattractant implicated in neutrophil and macrophage recruitment KC/GRO, IL-17A/F, and MIP-2, Figure 29B-D. Proinflammatory cytokines TNFα, IL-6, and IL-1β were also reduced to within saline treatment levels, Figure 29E-G.Together, these results showcase the robustness of this novel delivery system, reflected by the successful delivery and preservation of the therapeutic efficacy of Nexinhib20.

Here, we showed that the novel Nano-in-Micro delivery system, takes advantage of the highly proteolytic microenvironment to release nanoparticles to deliver immunomodulatory drugs to airway PMNs. Moreover, this shows that our N-in-M system allows for the delivery of drugs, such as Nexinhib20 that are only soluble in organic solvents such as ethanol and DMSO and as such limits their delivery to the lung. Here we have overcome this problem by compartmentalizing Nexinhib20 in nanoparticles allowing for pulmonary delivery to areas of highest PMN burden and protease activity.

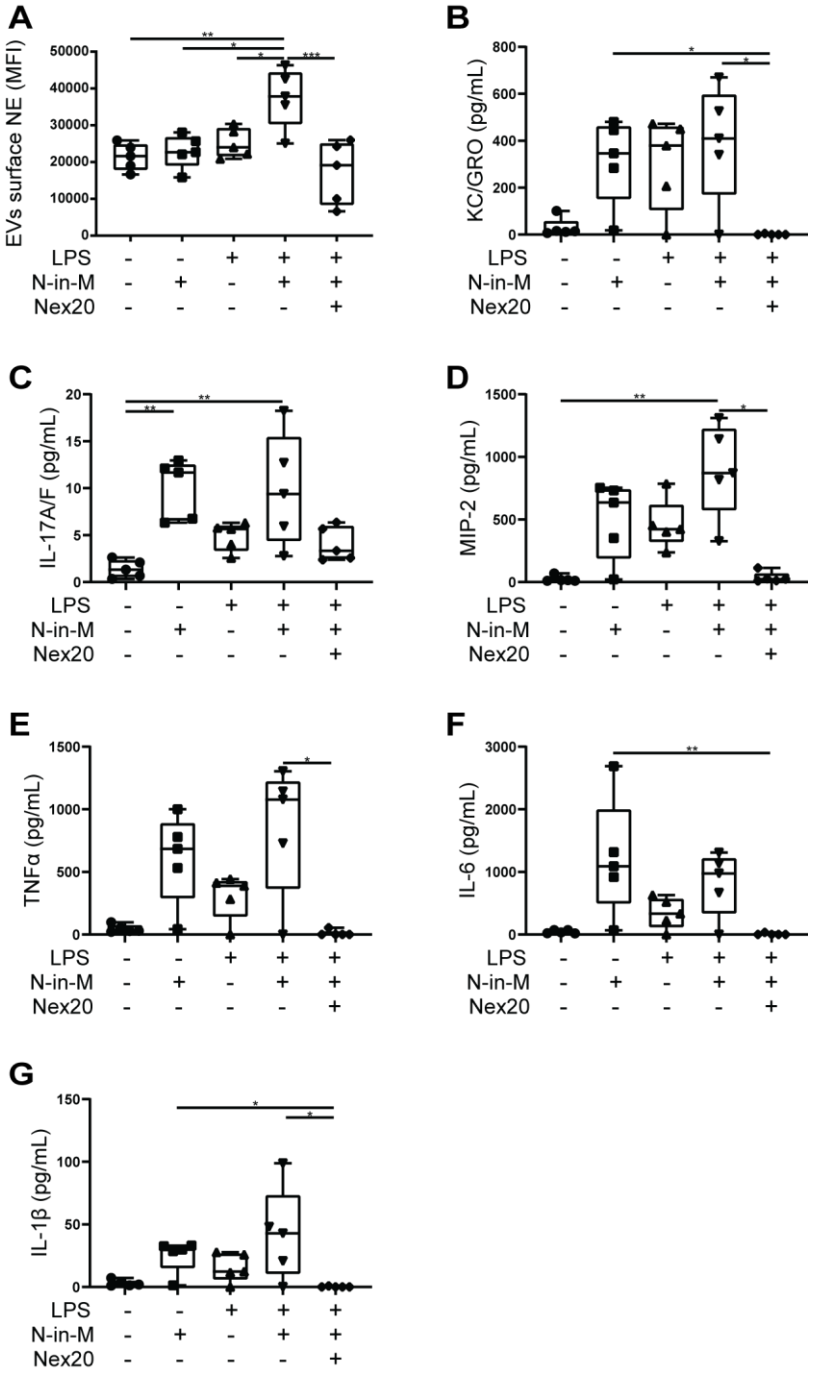

Figure 29: Nex20 Nano-in-Micro Cytokine Analysis Treatment with Nex20 Nano-in-Micro showed reduction of (A) EV-bound NE measured in the BAL. Proinflammatory cytokines (B) KC/GRO, (C) IL-17A/F, (D) MIP-2, (E) TNF (F) IL-6 and IL-1 were also low with Nex20 Nano-in-Micro treatment. *$p < 0.05$, ** $p < 0.01$, *** $p < 0.001$, between groups indicated.

4.2 Conclusion

The purpose of these studies was to understand (1) the phagocytosis and clearance of the Nano-in-Micro system in naïve *in vivo* settings following pulmonary delivery and (2) test the efficacy of the delivery system in an acute neutrophilic inflammation mode. The trypsin peptide crosslinker was used to understand how the Nano-in-Micro system without specific enzymatic degradation cleared over 24 hours *in vivo*. We showed that the lowest starting polymer concentration to fabricate the Nano-in-Micro system (20% w/v) was not rapidly phagocytosed (< 1 hour) but sustained fluorescent signal at 6h. Using the elastase-responsive peptide, we showed during LPS-induced acute neutrophilic inflammation that specific targeting of airway cells was achievable with the presented Nano-in-Micro delivery system, which preserved the efficacy of the delivered drug. Moreover, this self-contained delivery method allowed the targeting of airway PMNs, making it a viable therapeutic strategy for PMN-driven inflammation in airway diseases, such as cystic fibrosis and chronic obstructive pulmonary disease.

In conclusion, the results of these studies show that the MADE method for fabricating multi-stage particles produces enzyme-responsive microgels, without exposure to degradative conditions to preserve therapeutic efficacy, and also allow for quick release of nanoparticles for targeting pulmonary disease. Future work in optimizing a dry powder formulation for existing pulmonary delivery devices (e.g., DPIs, nebulizers) is needed to translate the system into clinical usage.

CHAPTER 5. AIM 3: MICROPHSIOLOGIC VASCULARIZED LUNG-ON-A-CHIP

Recent airway-on-a-chip microfluidic devices composed of a pseudostratified epithelium separated from a single layer endothelium by a synthetic polymer have allowed for simplified aspects of the lung environment to study the biochemical and metabolic activity in normal and diseased states [131–133]. However, replicating interstitial diseases such as iPF has been proven more difficult. Recently published methods have demonstrated that perfusable microvasculature can be recreated using microfluidics and that these *in vitro* techniques can reproduce normal and diseased states [107,186–188]. Improvements on the vascular design have created multi-layer microfluidic devices to observe the interactions between vasculogenesis and cancer organoids [189].

For most multilayered microfluidic devices, a semi-permeable cell culture membrane, often made of polydimethylsiloxane (PDMS) or polyester track-etched membranes, is used to create a physical barrier between cell types. These are significantly different from native extracellular matrix (ECM) and impact cell function and immune cell transport; however, thin films from native ECM have been incorporated into other multi-layered microfluidic devices [190]. Additionally, the adjacent endothelial monolayer does not recreate the structures of pulmonary microvasculature and lacks relevant interstitial cells such as fibroblasts. The inclusion of fibroblasts in these co-cultures is important as cross-talk between fibroblasts and epithelium influences wound healing [191] and is particularly important in iPF where the epithelium has been shown to direct the fibrosis [18,192,193].

Here, we show the design, fabrication, and cell troubleshooting of a multi-layer device to create the air-liquid interface of the upper respiratory airways that incorporates a vascularized endothelial network. We fabricated devices with both a 0.4 µm Polyester Track Etched (PETE) membrane and a more physiologically relevant vitrified collagen. Once the final design was chosen, microfluidic device fabrication was streamlined by formatting the microfluidic device into a 96 well format. A vitrified collagen membrane based microphysiologic device offered a physiologically relevant membrane that could allow for migration of immune-relevant cells into the apical side of the device. However, the natural-based fibrin gel used in the lower central channel for the vasculature began failing and had to be modified to create a stable hydrogel for use with the vitrified collagen. To show that the microphysiologic design was functional, 0.4 µm PETE devices were used to create a fibrosis-like pulmonary *in vitro* system.

5.1 Methods

5.1.1 Individual Microphysiologic Device Fabrication

Vasculature masters were fabricated on a silicon wafer by photolithography as previously described [187]. Slight modifications to the previously published designs were made and are detailed in Figure 30, courtesy of Michael Nelson. Airway masters were printed in Systems Accura 60 (Protolabs) with a 1 x 1 x 9 mm central channel and 1 mm guide marks matching the vascular microchannel layer ports. Devices were fabricated by bonding the feature side of the vasculature PDMS to the feature side of the (1 mm punched) airway PDMS with either a vitrified collagen membrane or a 0.4 PETE membrane (5.1.1.1 and 5.1.1.2) sandwiched between the features. Media reservoirs were either fabricated by punching a 10:1 ratio elastomer to curing agent polydimethylsiloxane (PDMS, Sylgard 184

Dow Corning) block and bonding to the cured airway PDMS piece, Figure 30A, or by using a faster method (described below) which used a single airway-reservoir PDMS piece made by thermal bonding, Figure 30B.

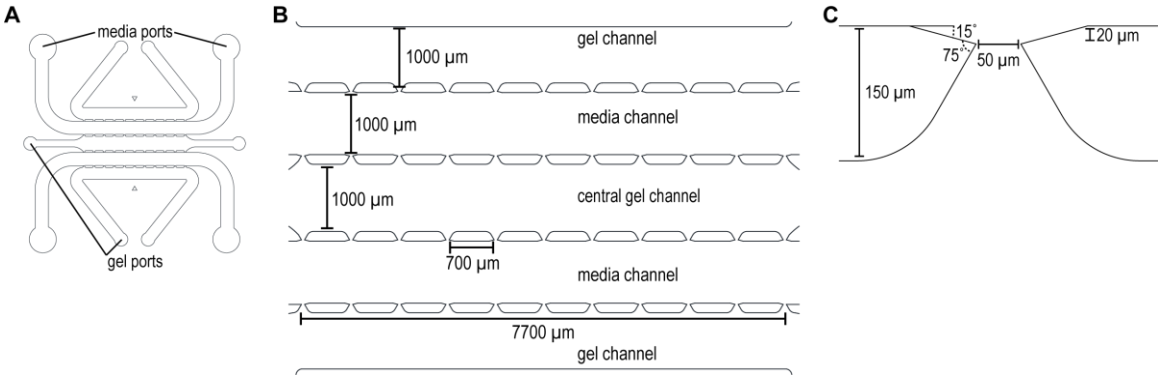

Figure 30: Vasculature Design Schematic (A) Overview of the 5-channel device with the media and gel ports labeled, (B) the 5 channels are each 1 mm wide and separated by (C) 50 µm ports designed to keep the air-liquid interface of the liquid fibrinogen and empty media channel as the fibrin gel forms.

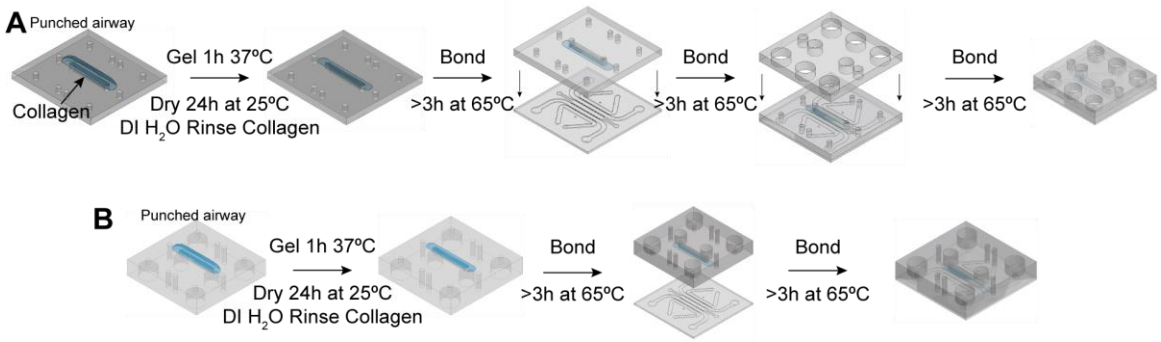

Figure 31: Single Device Fabrication Schematics (A) Three-piece or (B) two-piece fabrication sequence for the individual microphysiologic devices.

To fabricate the airway-reservoir piece two methods were used, Figure 32. Media reservoir molds were fabricated out of EcoFlex (Smooth-On) or Smooth-Cast 310 (Smooth-On). To fabricate the reservoir EcoFlex/Smooth-Cast mold a negative of the reservoirs was created by punching a 5:1 ratio of PDMS elastomer to curing agent with 4 mm biopsy punches at the airway and vasculature media ports to match the full 3D printed

airway master. EcoFlex or Smooth-Cast 310 was poured over the negative following manufacturing instructions. The EcoFlex/Smooth-Cast mold was then briefly plasma treated (20 seconds) and silanized (trichloro(1H,1H,2H,2H-perfluorooctyl)silane) for more than 3 hours before pouring with PDMS. The airway and media ports were molded as one piece by pouring 10:1 PDMS in two stages: (i) the airway mold was poured with enough PDMS to slightly cover the ports and cured for 30-45 minutes at 65°C (ii-EcoFlex) the without removing the cured PDMS, 2-3 mm of PDMS was poured on top of the cured PDMS, degassed and the EcoFlex mold was then aligned over the posts and cured at 65°C for an hour. Alternatively, (ii-Smooth-Cast) the cured PDMS airway mold was removed from the master, the Smooth-Cast mold was then poured, degassed, the cured airway PDMS piece was then placed and weighted on the Smooth-Cast mold and cured at 65°C for an hour. Once cured, the airway-reservoir PDMS layer was separated from the mold and punched with a1 mm biopsy punch.

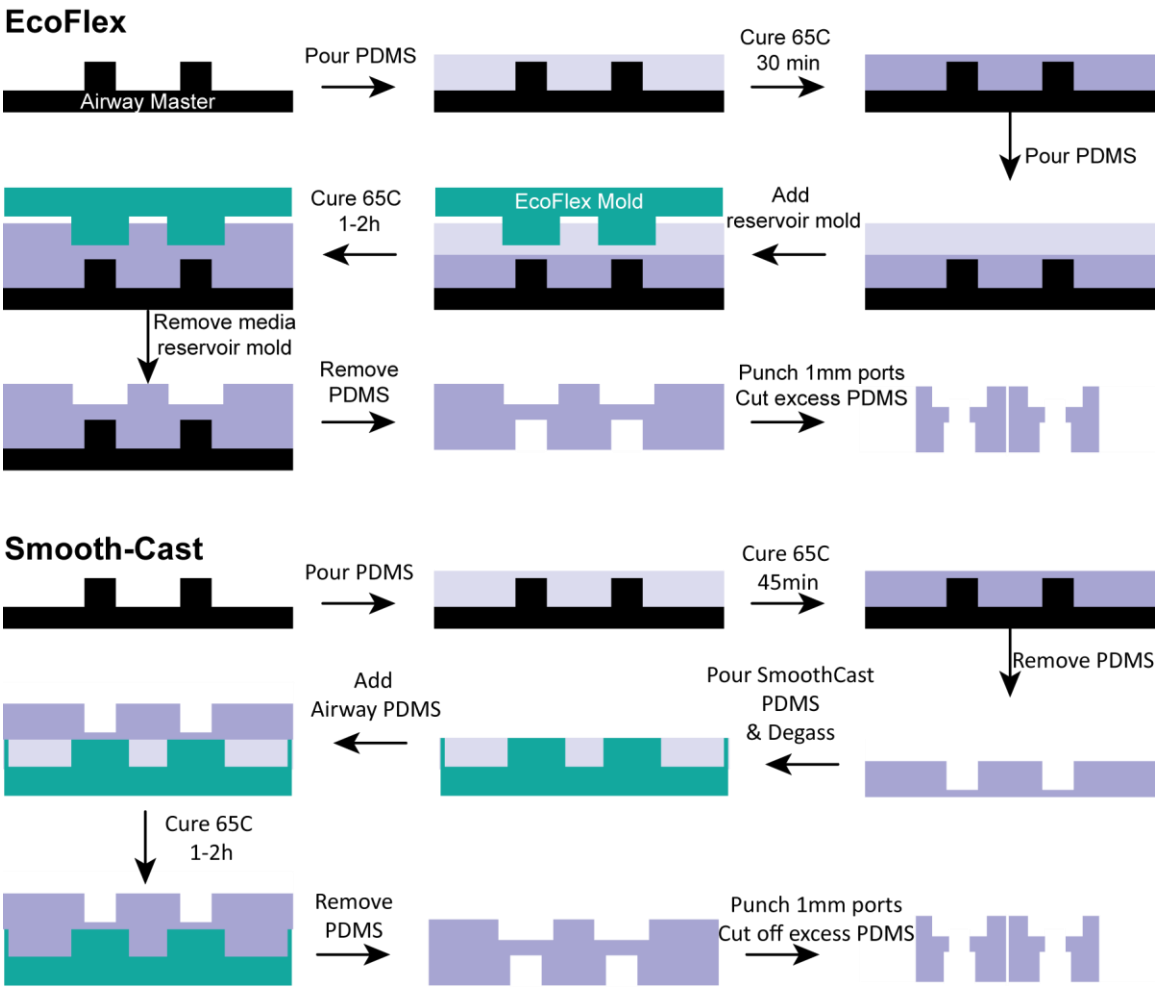

Figure 32: Airway-Media Reservoir Fabrication Methods Single PDMS pieces of the airway mold and media reservoirs were fabricated by using either an EcoFlex or Smooth-Cast mold and thermally bonding the PDMS as described in the schematic.

5.1.1.1 Collagen Membrane

A vitrified collagen membrane, to replicate the basement membrane, was made as previously described [190] directly on the punched airway channel by mixing rat tail type 1 high concentrated collagen (Corning) with 10x PBS, 1N NaOH, DI water according to manufacturer's instructions for a final collagen concentration of 4 mg/mL. Once well mixed, approximately 35-40 µL of collagen was pipette across the open airway channel, incubated in a 37°C humid incubator for 45-60 minutes, then allowed to dry at room temperature overnight. Membranes were then rinsed with DI water to remove excess salts,

water was aspirated, and membranes were allowed to dry for at least 6 hours before bonding. The vascular and airway layers were then treated with oxygen plasma for 60 seconds using a Harrick Plasma Cleaner (PDC-001) and left to bake at 65°C for at least 3h. Once fully bonded, excess PDMS was cut off the device sides.

5.1.1.2 0.4 µm Polyester Trach Etched (PETE) Membranes

PETE membranes were bonded with (3-aminopropyl)triethoxysilane (APTES) as previously described [194]. Briefly, optically transparent 0.4 µm PETE membranes were cut from 6-well Transwell (Corning), plasma treated for 20 seconds, and placed in 5% APTES preheated to 80°C for 10 minutes. Membranes were then dried on a Kimwipe, the airway and vasculature PDMS surface was then activated with oxygen plasma and the membrane was sandwiched between the two PDMS pieces. This method also works with the Sterlitech PETE membranes; however, the 0.4 µm lack the optical transparency of the transwell membranes.

5.1.2 96-well Plate Microphysiologic Device Fabrication

The vasculature microchannel design was adjusted so the media and gel ports centered in the middle of the 96-wells; new masters were fabricated by photolithography. As the silicon masters could only fit a 2 x 2 array, the vasculature master was poured twice for each 96-well plate. Airway masters were printed in Systems Accura 60 (Protolabs) with a 2 x 4 array of 1 x 1 x 14.57 mm central channel and 1 mm guide marks matching the vascular microchannel layer ports. PDMS molds of the airway channel were first bonded to black bottomless 96-well plates (Greiner Bio-One). 96-well bottomless plates were immersed in a 2% v/v solution of 3-mercaptopropyl timethoxysilane (Sigma Aldrich) diluted in methanol for 1 minute, rinsed with deionized water, and air dried. Plates and

PDMS airway molds were plasma treated, aligned, bonded together, and left at 65°C overnight [195]. Collagen or PETE membranes were then added as described in sections 0 and 5.1.1.2. The non-feature side of the vasculature molds was bonded to glass coverslips, then the feature side was aligned and bonded in pairs to the bottomless 96-well plate and airway channel, Figure 33A. Top view of the completed device can be seen in Figure 33B.

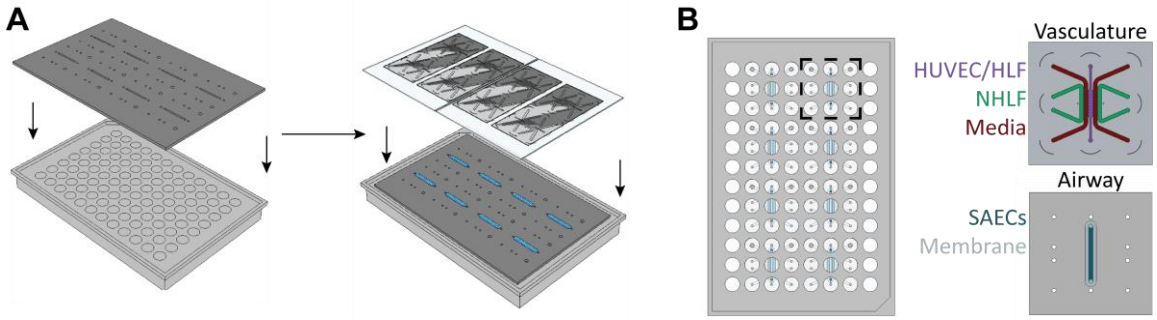

Figure 33: 96-well Plate Microphysiologic Device Fabrication (A) 96-well fabrication plasma bonding sequence (B) Top view schematic of the 96-well design and cutouts of a single device PDMS layers.

5.1.3 Cell Culture and Device Seeding

Normal Human Lung Fibroblasts (NHLF, Lonza lot # 608197 and # 508583) and Idiopathic Pulmonary Fibrosis Human Lung Fibroblasts (iPF-HLF, Lonza lot # 627840) were grown to passage 7 in Fibroblast Growth Medium-2 BulletKit (Lonza). Human Umbilical Vein Endothelial Cells (HUVECs, Cat # C2519A) were grown on 0.1% Bovine Gelatin (Sigma Aldrich) coated flasks up to passage 8 in Microvascular Endothelial Cell Growth Media-2 BulletKit (EGM2MV, Lonza). Normal Human Small Airway Epithelial Cells S-ALI Guaranteed (SAECs, Lonza lot # 677244) were grown in PneumaCult-Ex Plus to passage 3 and differentiated in PneumaCult-ALI medium (STEMCELL Technologies). Endothelial cells with or without iPF-HLF or NHLF (#608197) were resuspended in thrombin (4 U/mL) mixed 1:1 with fibrinogen/collagen (9 mg/mL / 1 mg/mL), unless the

gel was otherwise defined, and flowed into the lower central channel for a final concentration of ECs at 6e6 cells/mL and iPF-HLF at 0.3e6 cells/mL. NHLF (#508583) were resuspended in thrombin at 6e6 cells/mL (4 U/mL) mixed 1:1 with fibrinogen (10 mg/mL) and flowed into the outer two side channels. The fibrin gels were then placed in a 37°C humid incubator to gel for 15 minutes before the addition of EGM2MV into the media reservoirs, media was then exchanged daily. On day 4 hSAECs were seeded in the top airway channel at 2.5e6 cells/mL in PneumaCult-Ex Plus, allowed to acclimate for 24 hours then airlifted by pipetting the media out of the upper channel. Once airlifted, a 50/50 mixture of EGM2MV/PneumaCult-ALI was used to feed the device.

5.1.4 Fibroblast Screening

Five lots of fibroblasts were purchased from Lonza (Lot #s: 580583, 608197, 548315, 655309, 615568) and screened for their vasculogenic potential. Screening was completed in simple vasculogenic devices. Vascular masters were poured with 3-4 mm of 10:1 PDMS and cured. Once cured the media ports were punched with a 4 mm biopsy punch and the gel ports were punched with a 1 mm biopsy punch. The feature side of the PDMS was then bonded to a square glass coverslip. HUVECs were seeded in the central channel to a final concentration of 6e6 cells/mL in a 3 mg/mL fibrin gel. Outer channels were seeded with each individual lot of fibroblasts (passage 7) at a final concentration of 3e6 cells/mL in a final concentration 3 mg/mL fibrin gel. Devices were fed EGM2MV for 5 days, perfused with dextran, then fixed and stained with phalloidin.

5.1.5 Fibrin-Collagen-PEG Hydrogels

Fibrin, collagen, and PEG hydrogel combinations were loaded into the central channel of the vitrified collagen membrane devices. Fibrinogen was pegylated similarly to

previously published work [196,197]. Briefly, fibrinogen was dissolved at 12 mg/mL in PBS and sterile filtered. Immediately before use, 3400 Da bifunctional succinimidyl valerate (SVA) PEG (Laysan) was dissolved at 12 mg/mL and sterile filtered. Fibrinogen and PEG were mixed to twice the final concentration (PBS added to dilute as necessary), incubated the indicated amount of time at 37°C and placed on ice before the addition of collagen. High concentration rat collagen was dissolved to 6 mg/mL following manufacturer's instructions and left on ice.

5.1.6 Perfusion

Device perfusion was imaged using a BioTek Lionheart system with a 4x objective. Montage parameters were set on each individual device, 50 µL of 10 µg/mL 70 kDa FITC-dextran in PBS was added to one media port and the device was immediately imaged. Images were stitched and contrasted with Gen 5.04. For the percentage of perfusable area analysis the stitched images were straightened and cropped to remove the ports using Adobe Photoshop. Cropped images were then analyzed for fluorescent area using ImageJ by adjusting the threshold until all vessels were captured [198]. Images where the dextran leaked into the airway were excluded from analysis; images with perfusable vasculature with areas where the dextran flowed between the top of the gel and the bottom of the membrane had the area included in the calculation but not the GFP fluorescence.

5.1.7 Immunofluorescent Staining

Devices were stained as previously described [186]. Briefly, devices were washed 3 x with PBS, fixed with 4% paraformaldehyde for 10 minutes, permeabilized for 15 minutes with 0.1% v/v Triton X-100, washed with PBS, and then blocked for 3 hours at room temperature with 5% w/v BSA and 4% v/v goat serum. Primary antibody was diluted

1:100 in the blocking buffer and devices were stained overnight at 4C. Devices were then washed with 0.1% w/v BSA in PBS. Devices were incubated with secondary antibodies diluted at 1:250 and DAPI diluted to 1:1000 in blocking buffer for 3 hours at room temperature; antibodies used are listed in Table 6. Devices were then washed in 0.1% BSA and imaged.

Table 6: Antibodies Used for Microphysiologic Device Staining

Target	Clone	Fluorophore	Secondary
α-SMA	E184	Alexa Fluor 488	N/A
TUBB4	6C2	Primary	Goat-Anti Mouse 555 or 647
Pro-Collagen I	PCIDG10	Primary	Goat-Anti Mouse 555
CD31	WM59	Alexa Fluor 647	N/A
Rabbit IgG Isotype	EPR25A	Alexa Fluor 488	N/A

5.1.8 Confocal Microscopy

Fluorescent images were collected on a PerkinElmer UltraVIEW VoX spinning disk confocal microscope with a Hamamatsu C9100-23b back-thinned EM-CCD and Nikon 10x NA-0.3 air objective or a Nikon S Plan Fluor ELWD (extra-long working distance) 20x NA-0.45 air objective. To account for variability in the laser over time, devices for each experiment were imaged in a single session and devices from experimental groups were randomized during the session. Each device was imaged in 5-6 regions in the central channel, MFI was measured using Volocity software (Perkin Elmer) and if outliers were identified in GraphPad Prism by ROUT (Q = 0.2%) the entire device was removed from analysis.

5.1.9 Statistical Analysis

Data were analyzed using GraphPad Prism with a Shapiro-Wilk test for normality (α=0.05). A one-way Anova (α = 0.05) with post-hoc Tukey's test with an adjusted P value

for multiple comparisons, or a two-way Anova ($\alpha = 0.05$) with Sidak post hoc analysis was used with parametric data. Where applicable, Kruskal-Wallis ($\alpha = 0.05$) with Dunn's test was used for nonparametric data

5.2 Results

5.2.1 Microphysiologic Device Overview

We designed a microphysiologic device to recapitulate the endothelial vasculature, stromal environment, and epithelial cell layers of the lower respiratory airways, Figure 34A. It was composed of two main PDMS pieces; the bottom layer was a 5-channel device that provided the structure to create a vascularized hydrogel in the center of the device while the second layer provides a single channel for airway epithelium, Figure 34B. The vascular layer had 2 outer channels (green) for normal human lung fibroblasts (NHLF) that created a cytokine gradient for vasculogenesis of the central channel (purple) loaded with human umbilical vein endothelial cells (HUVECs) with or without human lung fibroblasts (HLF). This device also provided the media channels for the entire microphysiologic device (red). The airway was a second PDMS piece punched at each of the gel and media channels (color coded) with a single channel that sat above the HUVEC/HLF channel for small airway epithelial cell (SAECs) culture. A thin film membrane was placed between the two layers to allow for gel loading and a substrate for the epithelial cell growth and differentiation. The vasculature layer was seeded first, Figure 34C, followed by the epithelium on day 3, which was then airlifted the next day and allowed to differentiate for the following 5-7 days. We confirmed the HUVECs formed vessel structures (white arrow YZ section) within a fibrin gel below the airway epithelium (green arrow), Figure 35.

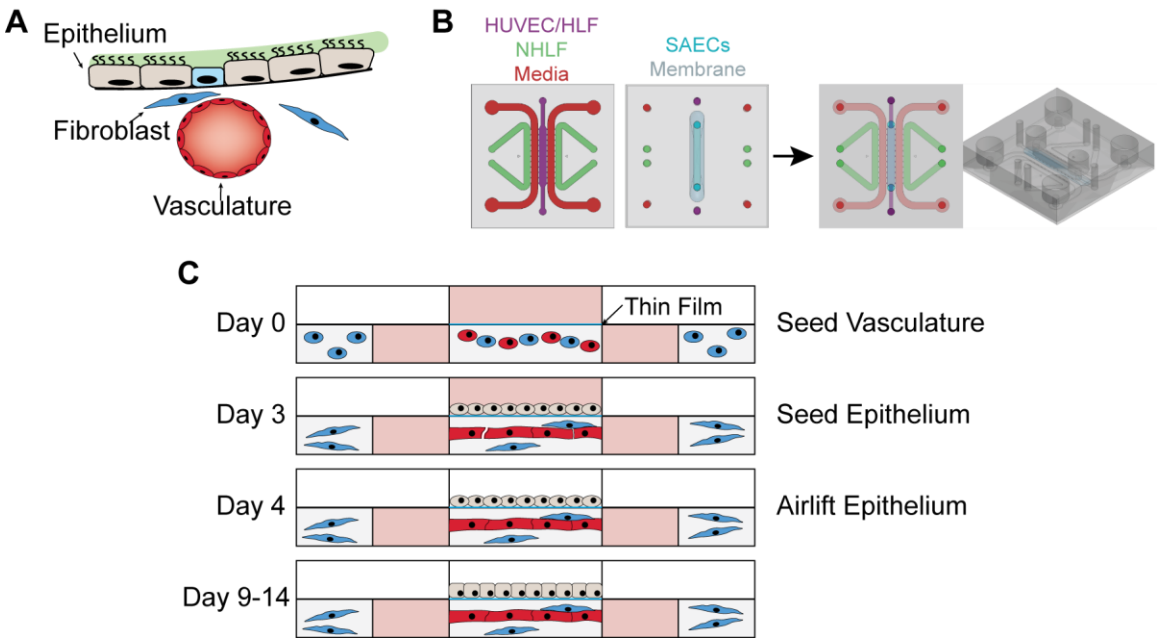

Figure 34: Microphysiologic Device Layout Schematics (A) Diagram of the lung physiology replicated (B) The device is composed of two PDMS layers separated by a thin film membrane, bonded together to create the multi-layer device. (C) Schematic of the microphysiologic device cross section and time course for cell growth and structure.

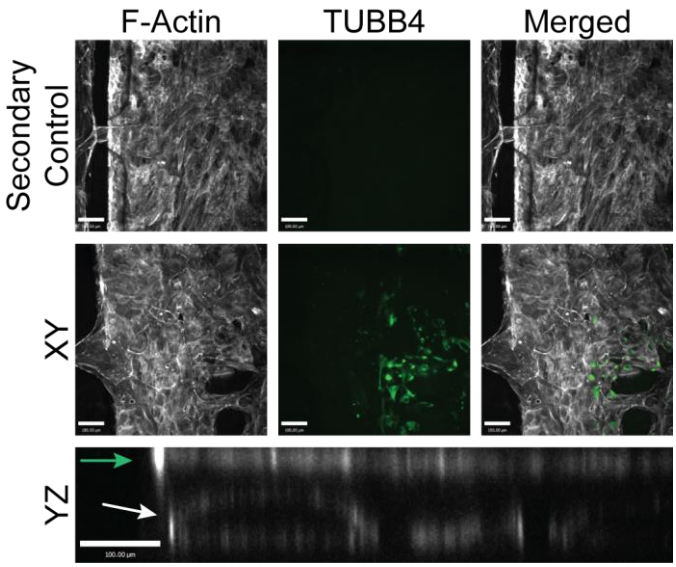

Figure 35: Device Staining and Cross Section Microphysiologic devices (0.4 µm PETE) were stained for F-Actin (white) and tubulin IV (green). Extended Focus Z-stacks of the XY plane show F-Actin staining throughout the device, while tubulin appears in the epithelium, YZ sections show vascular structures (white arrow) below the epithelium (green arrow).

5.2.2 Fibroblast Screening

Initial devices were seeded with mesenchymal stem cells in the outer stromal cell channels, and while they formed vasculature, the ports failed to consistently open for functionally perfusable devices. Five lots of fibroblasts were tested for their ability to direct vasculogenesis. Lots were designated A-E, and donor information provided by Lonza certificates of analysis can be found in Table 7. While each fibroblast lot created-vessel like structures, only two lots created at least partially perfusable devices, Table 7 and Figure 36.

Table 7: Fibroblast Lot Summary Information

Label	Lot #	Age	Gender	Ethnicity	Smoker (Y/N)	Perfusable Devices
A	580583	79	F	C	Y	6/6
B	608197	67	M	C	N	4/8
C	548315	52	M	C	Y	3/6
D	655309	56	M	B	N	0/7
E	615568	12	M	H	N	6/6

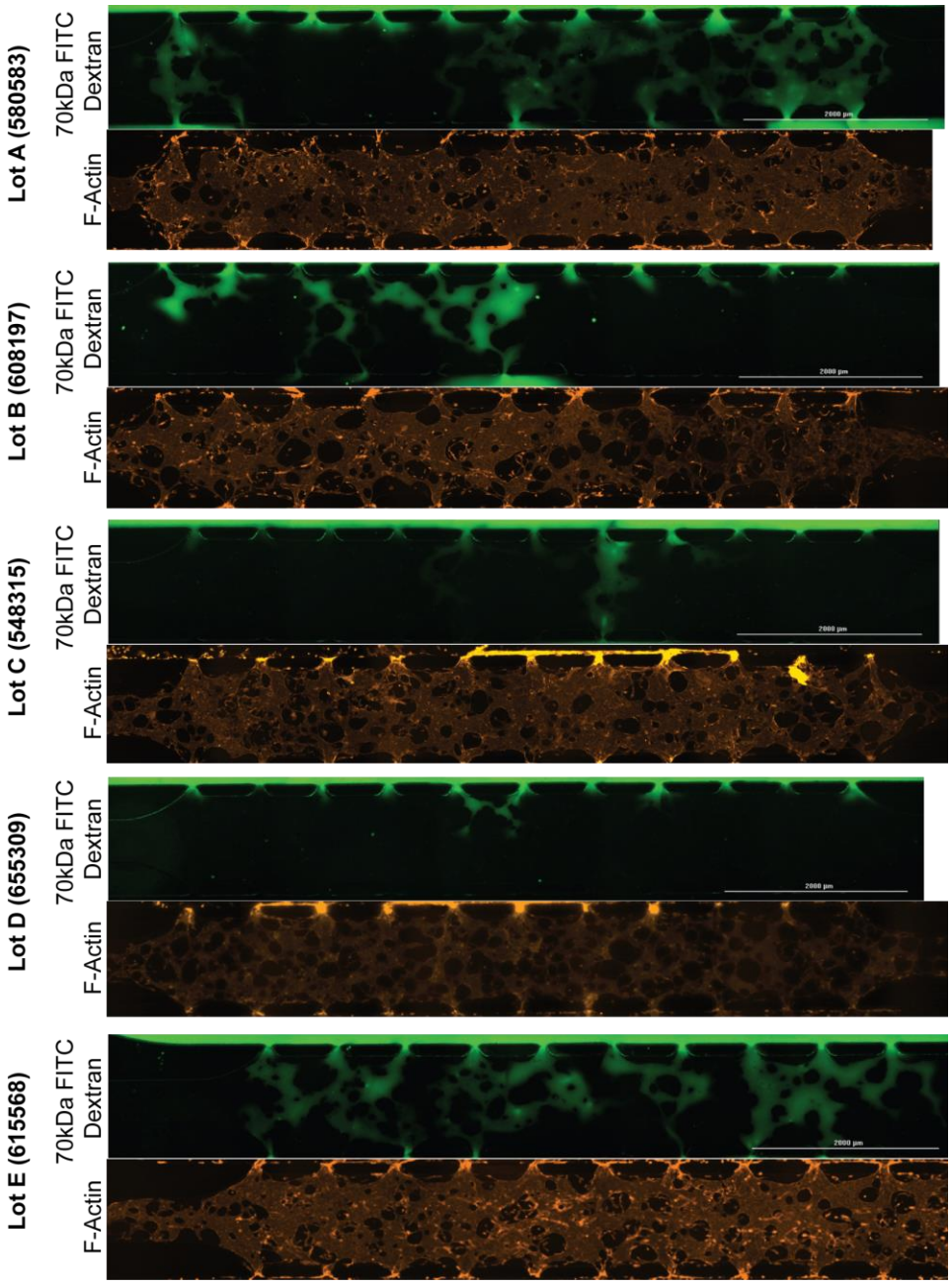

Figure 36: Fibroblast Lot Effects on HUVEC Vasculogenesis and Perfusion Representative images of perfusable vasculature alongside the same fixed F-Actin stained devices for passage 7 fibroblasts.

These two lots were then seeded into the vitrified collagen microphysiologic devices in the outer channels with and without the respective lot also seeded at a 10:1 HUVEC to NHFL ratio in the central channel for 12 days. Devices seeded with lot E (615568) fibroblasts had begun to overgrow resulting in large flat regions of FITC-Dextran

signal due to leakage rather than perfusion, Figure 37. Lot A fibroblasts created perfusable networks with endothelial only devices; however, with endothelial/fibroblast co-cultures the devices began to overgrow as well. Lot A (580583) was chosen for the outer channels to direct vasculogenesis while lot B (608197) was chosen for future co-culture with endothelial cells in the central channel. Lot B was chosen for the central channels since it appeared to form some vasculature suggesting it provided necessary cytokine signaling but was not as effective as A, so we believed that the lot A fibroblasts could produce a competitive cytokine gradient relative to B to create vasculature with fibroblasts.

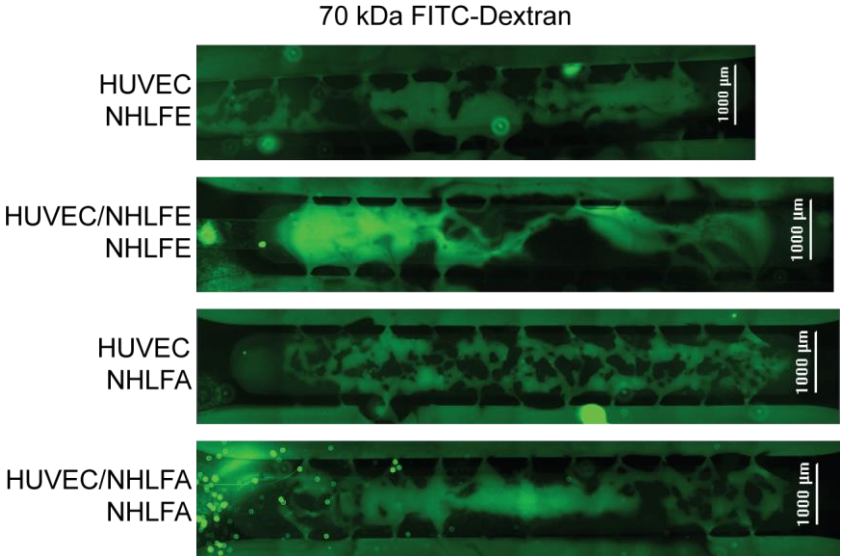

Figure 37: Fibroblast Lot Effects on Microphysiologic Lung-on-a-Chip Vasculature 70 kDa FITC-Dextran perfusion of 12 day cultured vitrified collagen microphysiologic devices loaded with the two perfusable fibroblast lots in the outer channels and HUVECs with or without the respective fibroblast lot at a 1:10 ratio in the central channel, and hSAECs in the airway channel.

5.2.3 Fibrin/Collagen Hydrogels

To further improve the vascular network, collagen was added to the fibrin gel since fibrin/collagen hydrogels of various ratios have been shown to improve tubule formation [104,199]. The total gel concentration was kept at 5 mg/mL, and collagen was added from

0.25-1 mg/mL. Devices were seeded with a 20:1 HUVEC to NHLF in vitrified collagen and PETE membrane devices. Oddly, all vitrified collagen devices including the fibrin only gel that had previously been successful began failing on day 4. The gel pulled off the posts on day 4 and eventually collapsed the rest of central channel, Figure 38. The PETE based microphysiologic devices did not have this issue, and, based on phase contrast imaging, the 4.5/0.5 mg/mL fibrin/collagen gel was chosen for future studies, Figure 39.

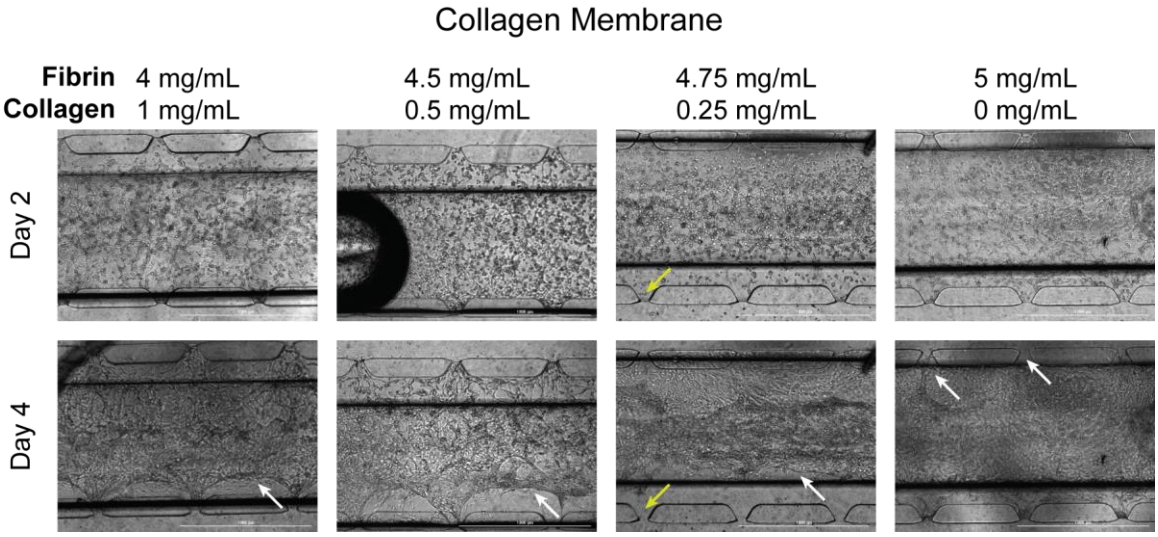

Figure 38: Vitrified Collagen Device Fibrin/Collagen Hydrogel Failure HUVECs and NHLFs (20:1) were seeded in fibrin/collagen gels at final concentrations of 4/1, 4.5/0.5, 4.75/0.25, and 5/0 mg/mL (n = 8 per gel). Phase contrast images of representative devices for each gel type were taken on day 2 and 4 after seeding. White arrows indicate regions where hydrogel failure can be seen, yellow arrows point to the visible lack of gel in a post between the two time points, scale bars = 1000 µm.

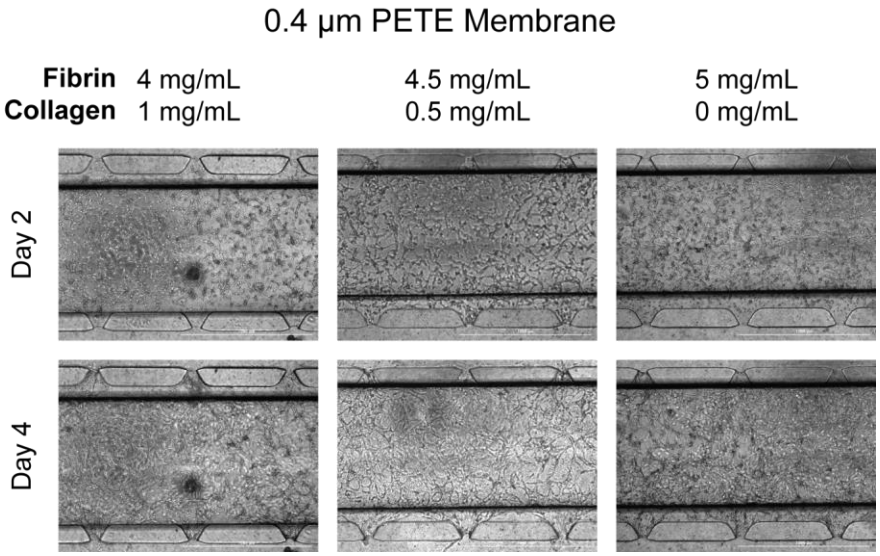

Figure 39: PETE Device Fibrin/Collagen Hydrogels HUVECs and NHLFs (20:1) were seeded in fibrin/collagen gels at final concentrations of 4/1, 4.5/0.5, and 5/0 mg/mL. Phase contrast images of representative devices for each gel type were taken on day 2 and 4 after seeding, scale bar = 1000 µm.

Since the human fibrin only gel formulation had been previously successful, the vitrified collagen devices were loaded again with 5 mg/mL fibrin gels but exhibited similar results with 35 of 40 devices failing (~12.5% success rate). Since the hydrogel failures were not observed with the stiffer PETE membranes, failure in the vitrified collagen devices was most likely a result of the forces exerted on the hydrogel by the HUVECs and NHLFs in combination with the flexibility of the vitrified collagen membrane.

5.2.4 Fibrin/Collagen/PEG Hydrogels for Vitrified Collagen Devices

The loss of a stable fibrin hydrogel may be due to batch-to-batch variability of the human fibrinogen; this poses a significant problem for disease-relevant devices as fibrotic myofibroblasts, are contractile cells [200–202]. PEG has been previously used to create a stiffer fibrin hydrogel with 5 mg/mL Fibrin and 0.5 mg/mL bifunctional succinimidyl glutarate (SG) PEG [196,197]. Here we modified the fibrinogen with a bifunctional succinimidyl valerate (SVA) PEG. PEG-SVA was chosen over PEG-SG as SVA has a

reactivity half-life of approximately 30 minutes, double the time for SG. Various combinations of fibrinogen, collagen, and PEG with varying preincubation times for the fibrinogen with the PEG were tested for gelation times within 15 minutes, Table 8, gel combinations that did not gel are labelled DNG. Of note the previously published ratios of fibrin/peg 5/0.5 mg/mL did not gel with preincubation for PEG-SVA; however, lower concentrations of PEG resulted in stable hydrogels. Hydrogel combinations that gelled within 15 minutes were tested in vitrified collagen devices.

Table 8: Fibrin/Collagen/Peg Hydrogel Formulations Tested

Fibrin (mg/mL)	Collagen (mg/mL)	SVA-PEG-SVA (mg/mL)	Pre-incubation (min)	Experiment End
5	0	0	N/A	Day 4
5	0	0.5	0	Day 5
5	0	1	15	DNG
5	0	0.5	15	DNG
5	0	0.5	30	DNG
5	0	0.25	30	>Day 9
5	0	0.1	30	>Day 9
4.75	0.25	0	N/A	Day 4
4.75	0.25	0.25	0	Day 5
4.75	0.25	0.5	15	DNG
4.75	0.5	0.25	15	>Day 5
4.75	0.25	0.25	15	>Day 5
4.5	0.5	0	N/A	Day 4
4.5	0.5	0.1	N/A	>Day 8
4.5	0.5	0.25	15	>Day 8
4.5	0.5	0.5	15	Day 1
4	1	0	N/A	Day 4
4	0	1	15	DNG
4	0.5	1	15	DNG
5 (Bovine)	0	0	N/A	>Day 8

Four combinations of fibrin/collagen/PEG (5/0/0.1, 5/0/0.25, 4.5/0.5/0.1, 4.5/0.1/0.25) survived 8-9 days of HUVEC/NHLF (20:1, VEGF/Ang-1) culture without signs of hydrogel failure, representative images Figure 40A. Perfusion in the devices was quantified with 70kDa FITC-dextran by the percentage of GFP positive area, Figure 38B, and percentage of perfusable ports, Figure 40C. Vasculature only devices published by Kim et al. had vessel area between 60-80% [187], this range is represented by grey dashed lines, Figure 38B. Alongside the 4 human fibrin combinations, 5 mg/mL bovine fibrin gels were tested. Of the 5 hydrogel formulations, the two human-fibrin/PEG formulations without collagen had the highest number of devices (4/7 and 6/7) within the 60-80% perfusion range. The bovine fibrinogen had 75% of the devices with 100% open (perfusable) ports; however, the HUVEC/NHLFs structured into large overgrown vessels rather than microvasculature. It is possible that the seeding density of HUVECs could be titrated to find a more-optimal density for the long culture times.

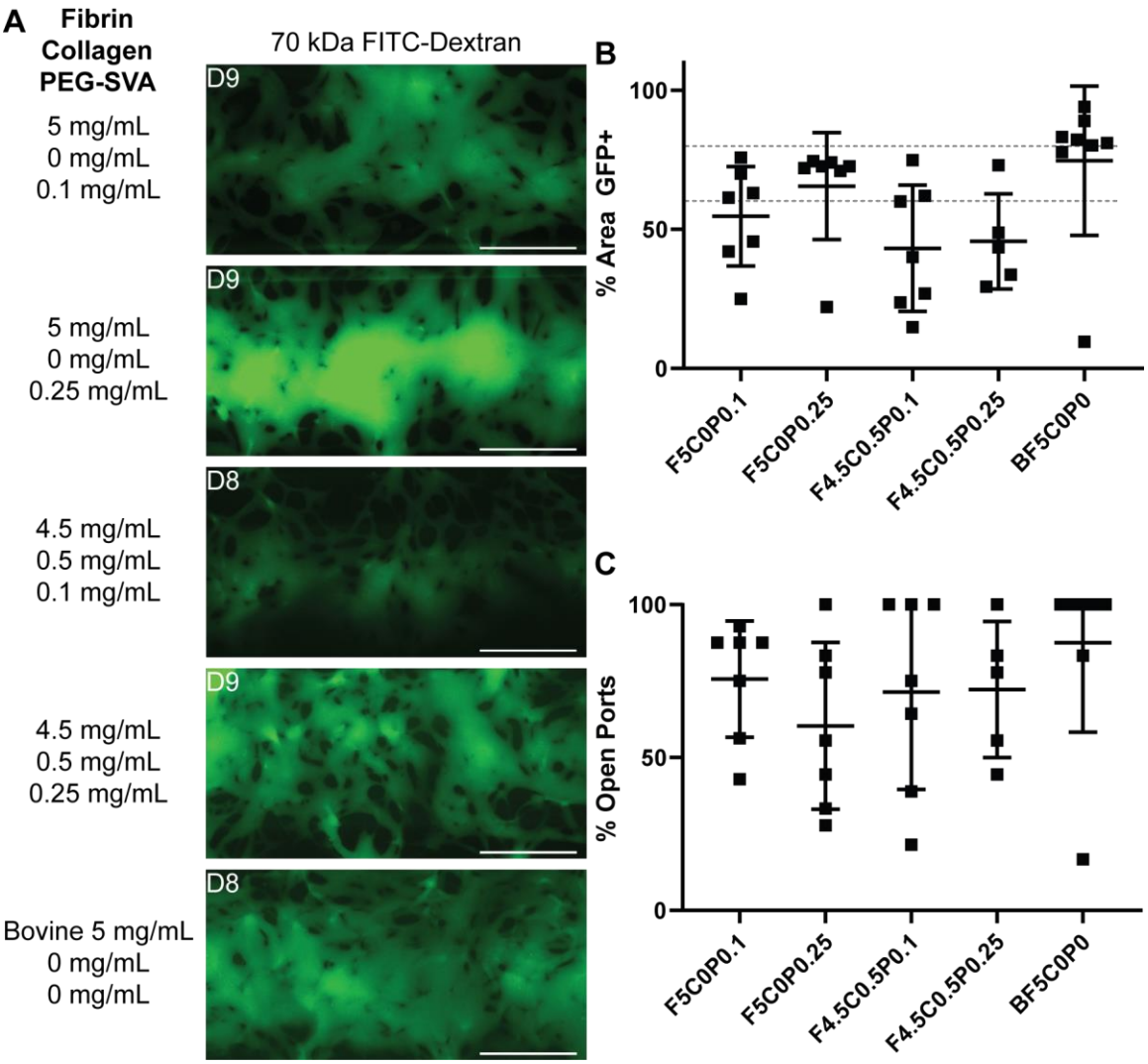

Figure 40: Fibrin/Collagen/PEG Vitrified Collagen Microvascularized Lung-on-a-Chip (A) Representative images of 70kDa FITC-Dextran perfusion in vitrified collagen devices, scale bar 500 µm. (B) Percentage of the central channel area between the posts positive for the 70kDa FITC-Dextran (GFP+). (C) The percentage of ports imaged that had perfusable vasculature.

5.2.5 0.4 µm PETE Fibrosis Model

Microphysiologic devices fabricated with 0.4 µm PETE membranes were seeded with either NHLF or iPF-HLF in the central channel alongside HUVEC in a 4.5 mg/mL 0.5 mg/mL Fibrin/Collagen hydrogel, maintained for 5 days and then treated with or without 5 ng/mL of TGFβ-1 for 3 more days. TGFβ-1 is often overexpressed by

myofibroblasts in iPF and is known to help progress fibrosis [191,202]. Hallmarks of myofibroblasts and resulting fibrosis include pro-collagen 1 and α-smooth muscle actin (α-SMA). Microphysiologic devices with NHLF and iPF-HLF stained positive for α-SMA with and without the TGFβ-1 treatment, Figure 41B. Each device stained positive for pro-collagen 1, possibly caused by non-specific binding of the antibody to the fibrin/collagen hydrogel mixture used for the devices. As the perfusable endothelial networks were still inconsistent in these devices, media was supplemented with VEGF and Ang-1 for the first 4 days of culture in subsequent experiments.

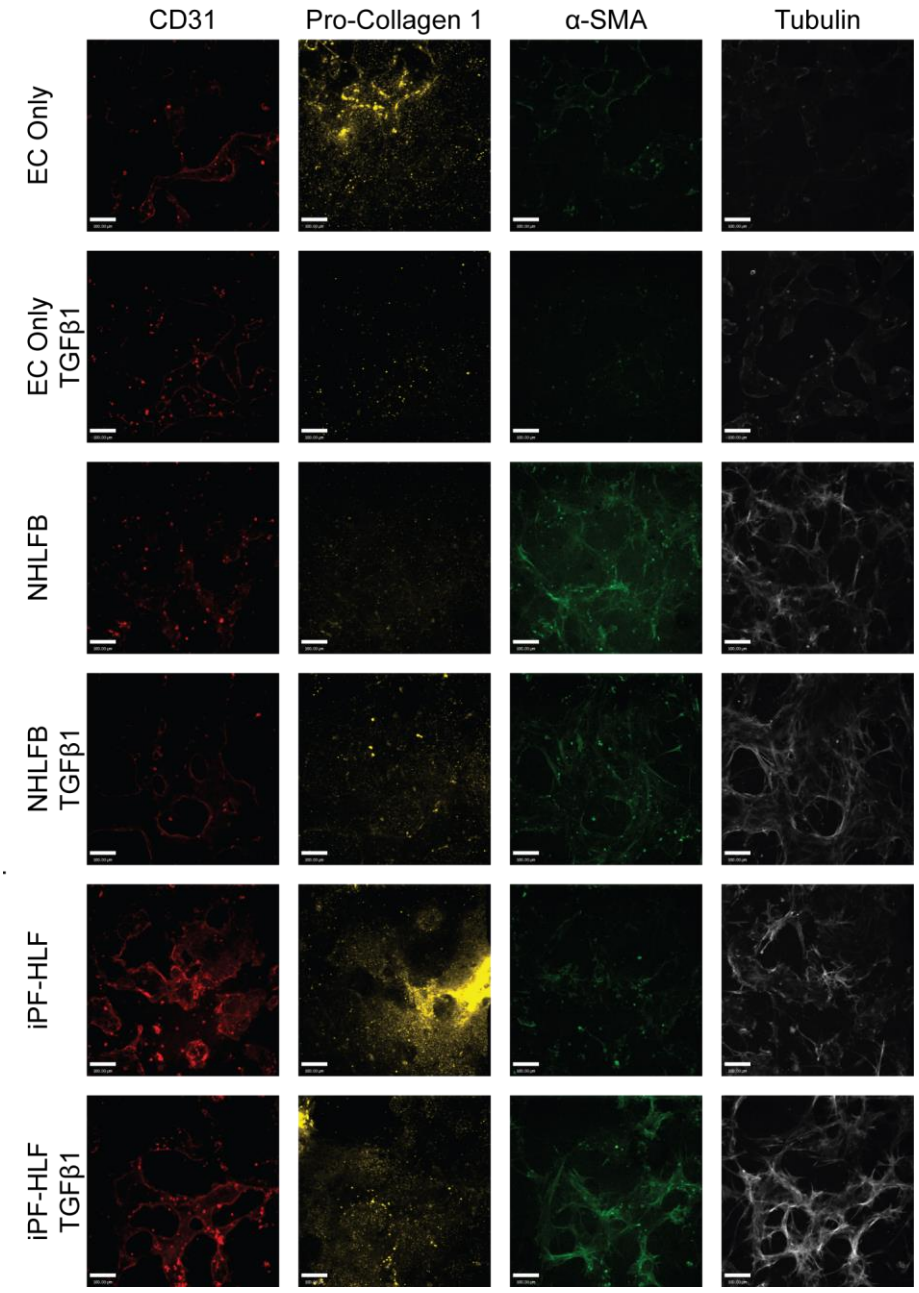

Figure 41: NHLF and iPF Device Pro-Collagen I and α-SMA Staining 0.4 μm PETE microvascularized lung-on-a-chip devices seeded with either NHLF or iPF-HLF alongside HUVECs in the central channel treated with or without 5 ng/mL of TGFβ1. Devices were stained for vascular endothelium (CD31, red), pro-collagen 1 (yellow), α-SMA (green), and F-Actin (white).

5.2.6 0.4 µm PETE Devices Treated with Pirfenidone

Pirfenidone is an antifibrotic drug used for treating iPF that often reduces the expression of α-SMA *in vitro* cultures of fibroblasts [202]. Microvasculature lung-on-a-chip devices were seeded with healthy fibroblasts, Figure 42A, or iPF fibroblasts alongside the HUVECs in the central channel. After 8 days of culture, (D5 of ALI), devices were seeded with media containing 50 or 100 µg/mL of Pirfenidone and on day 9 the cultures were ended and devices were perfused, representative images Figure 42B, then fixed and stained for α-SMA, endothelial cells (CD31), and nuclei (DAPI), representative images Figure 42C. The devices with NHLF had too much variability in perfusion measured by the percentage of open ports and the perfusable area to see changes in the Pirfenidone treatment, Figure 42D. For the devices with iPF derived fibroblasts, there appeared to be variability in perfusion of the devices with the increase in pirfenidone treatment negatively affect the percentage of perfusable vasculature across the device; however, there was no statistical significance, Figure 42E. Additionally, there was no change in the expression of α-SMA for either NHLF or iPF devices and notably no apparent difference in α-SMA MFI between the healthy and diseased fibroblasts. It is possible that while these fibroblasts had some base-line expression of α-SMA (relative to isotype control) that the fibroblasts alone are not able to recapitulate the fibrotic environment and additional treatment to the devices may be needed to induce fibrosis.

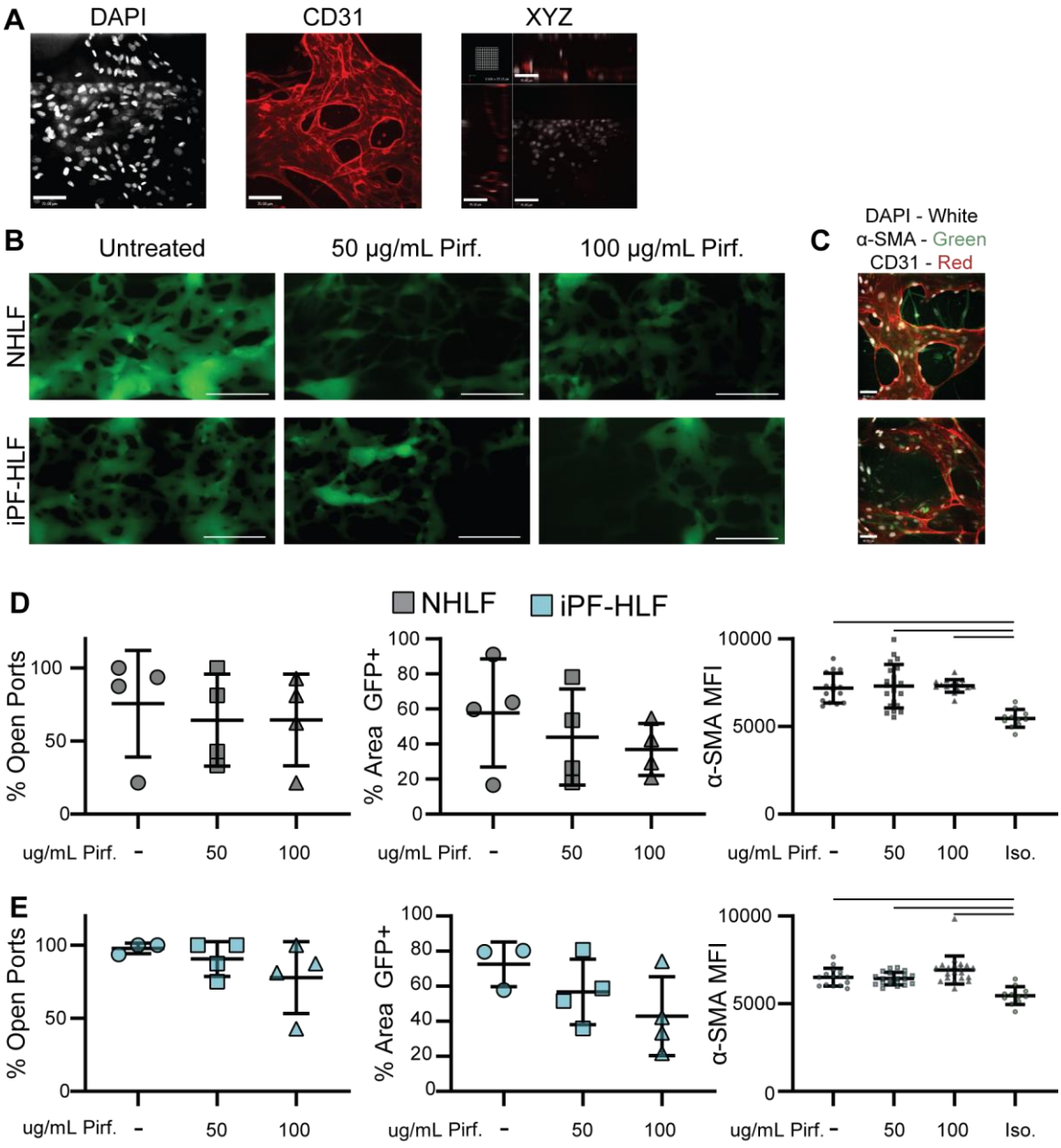

Figure 42: Pirfenidone Treated NHLF and iPF Microphysiologic Devices Devices were seeded with NHLF or iPF fibroblasts and treated with 50 or 100 µg/mL Pirfenidone on Day 8 (A) Representative extended focus z-stack of nuclei (DAPI) and endothelial cells (CD31) and XY, XZ, and YZ views of the endothelial tubules; images linearly contrasted for clarity, scale bars = 70 µm. (B) Representative images of 70kDa FITC-Dextran perfusion, scale bar = 500 µm. (C) Representative images of fibroblast α-SMA (green), endothelial cells (CD31-red) and nuclei (DAPI-white), linearly contrasted for clarity, scale bars = 50 µm. Characterization of vasculature by percentage of open ports for each device, percentage of the central channel area between the posts positive for the 70kDa FITC-

Dextran (GFP+) and α-SMA mean fluorescence intensity (MFI) for (D) NHLF and (E) iPF microphysiologic devices. Bars indicate statistical significance, $\alpha = 0.05$.

Next, microvascularized lung-on-a-chip devices were treated with or without 5 ng/mL of TGFβ-1 for 3 days (D5 of culture D1 of ALI) to push the fibroblasts toward a myofibroblast phenotype. The devices were then treated with 50 or 100 µg/mL of Pirfenidone for 24 hours. Perfusion of the devices, representative images Figure 43A, showed the addition of TGFβ-1 to the normal fibroblast cultures did not appear to impact vessel quality based on the number of perfusable ports and the percentage of perfusable area, Figure 43B-C. In the NHLF devices the addition of pirfenidone to the TGFβ-1 in the normal fibroblast devices appeared to cause the vasculature to become less stable as devices had fewer open ports and less perfusable area. Within this experiment the iPF seeded microphysiologic devices without any treatment had less than 60% perfusable area while the NHLF based devices were at 60-80%. The iPF devices also appeared to be sensitive to the TGFβ-1 treatment as the perfusable area appeared to drop and increased with the 100 µg/mL pirfenidone treatment, Figure 43B-C; however, there is no statistical significance. Staining for α-SMA, representative images Figure 44A, did not show increased MFI in the TGFβ-1 groups for either NHLF or IPF, Figure 44B-C. However, the NHLF TGFβ-1 was lower than the untreated devices and 50 µg/mL Pirfenidone but not the TGFβ-1 only treatment. It is possible that the current imaging technique is not sensitive enough to detect appreciable changes to the α-SMA in these microphysiologic devices. Future experiments to increase the α-SMA may be necessary to show an effective fibrosis model; TGFβ-1 concentrations can be increased or bleomycin injury to the epithelium may be tested to see if the fibroblasts can be pushed to a more myofibroblast phenotype.

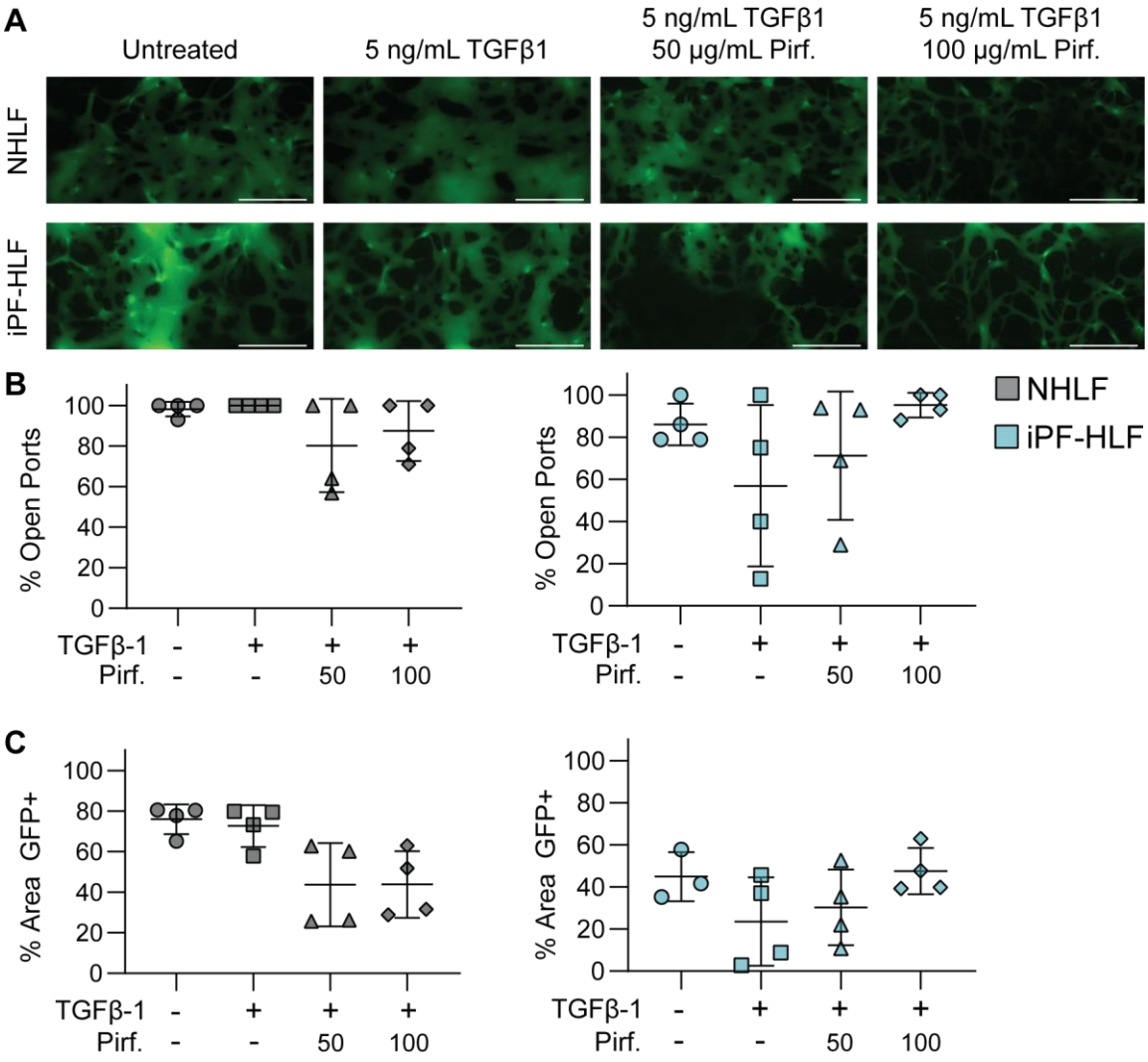

Figure 43: TGFβ-1 and Pirfenidone Treated NHLF and iPF Devices Microvascularized lung-on-a-chip devices seeded with normal and iPF fibroblasts were treated with/without 5 ng/mL TGFβ-1 for 3 days and with 50 or 100 µg/mL Pirfenidone for 1 day (A) Representative images of 70kDa FITC-Dextran perfusion, scale bar = 500 µm. (B) Percentage of open ports for each device and (C) Percentage of the central channel area between the posts positive for the 70kDa FITC-Dextran (GFP+).

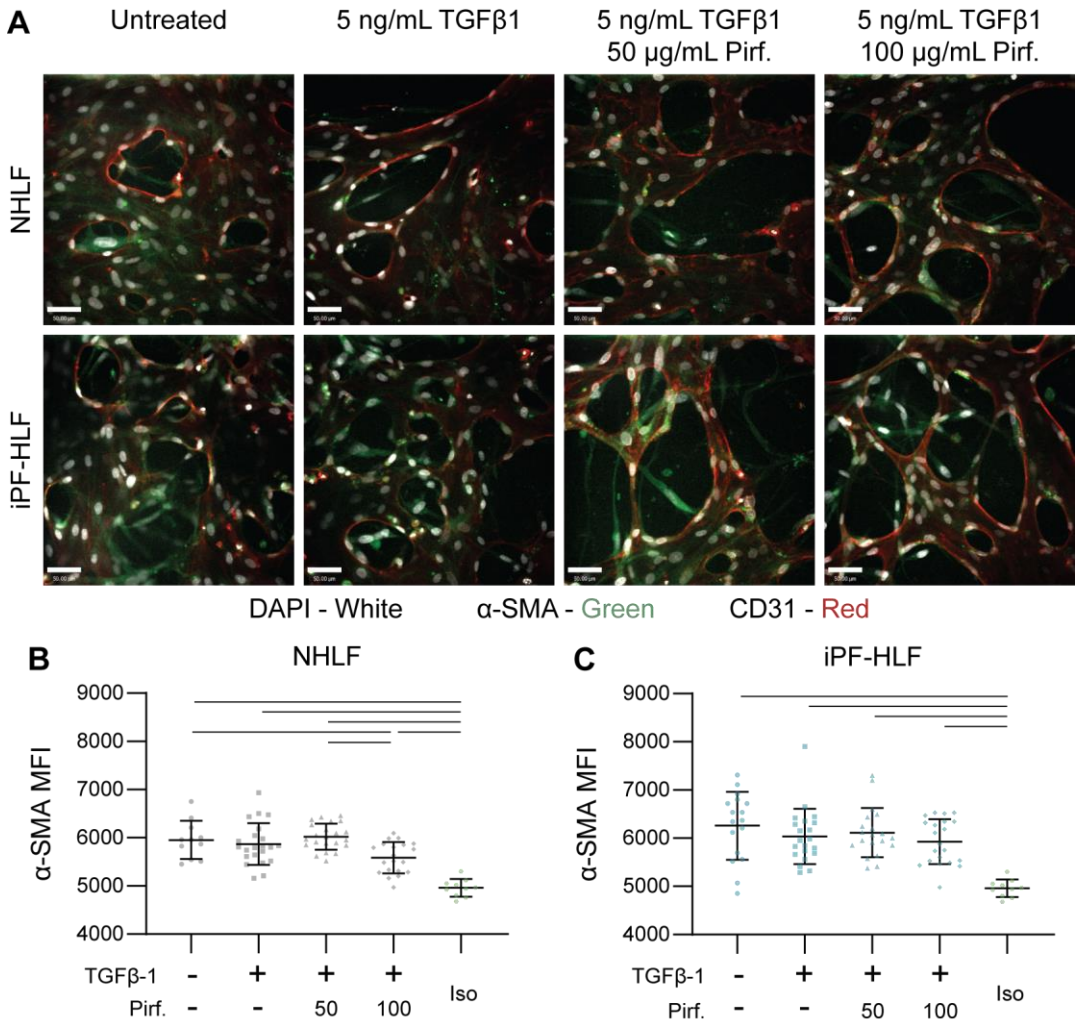

Figure 44: α-SMA Staining and Quantification Microphysiologic devices seeded with either normal or iPF fibroblasts alongside HUVECs were treated with 5 ng/mL of TGFβ-1 for 3 days and Pirfenidone for 1 day. (A) Representative fluorescent images of nuclei (DAPI-white), fibroblasts α-SMA (green), endothelial cells (CD31-red), linearly contrasted for clarity, scale bars = 50 µm. α-SMA mean fluorescent intensity for (B) NHLF and (C) iPF microphysiologic devices. Bars indicate statistical significance $\alpha = 0.05$.

5.3 Conclusions

We have successfully fabricated a multi-layer microphysiologic device that allows for the co-culture of endothelial cells in a vascular network alongside healthy or diseased fibroblasts below an airway epithelial layer. Devices were fabricated in a 96-well format for easier handling and medium-throughput experiments. Vitrified collagen membranes

could be incorporated into the microvascularized lung-on-a-chip with the addition of PEG into the fibrin hydrogel structure. Future analysis of the vasculature structure with Angiotool may be necessary to determine the vessel quality.

0.4 μm PETE membrane-based devices were able to recapitulate microvasculature with healthy and diseased iPF fibroblasts within the fibrin interstitium-like hydrogel. Increased α-SMA staining was visible in preliminary fibroblast-HUVEC co-cultures and treatment with anti-fibrotic Pirfenidone in TGFβ-1 fibrosis appeared to rescue the microvascular structure. Effects of the Pirfenidone on the fibroblast expression of α-SMA, MMP production or other inflammatory cytokines released have yet to be elucidated and are necessary to determine the extent of fibrosis recapitulated.

CHAPTER 6. CONCLUSIONS AND FUTURE WORK

In this dissertation the overall objective was to study the Nano-in-Micro multi-stage particles by investigating (i) how the microgels and nanoparticles interact with the phagocytic immune cells *in vitro* (Aim 1) and *in vivo* (Aim 2) and (ii) how we can recapitulate the vascular pulmonary environment to study these interactions in an *in vitro* setting (Aim 3)

6.1.1 Nano-in-Micro System

Nano-in-Micro multi-stage particles were studied to (i) provide aerodynamic size (ii) avoid rapid macrophage phagocytosis and (iii) deliver fluorescent and therapeutic nanoparticles for efficient endocytosis. Despite extensive knowledge on particle deposition and transport in the airways, there are several innovative aspects derived from this current work. This *in vitro* work has further improved upon the MADE method by changing the chemistry for faster reaction kinetics, shown the incorporation of a disease-relevant protease-responsive peptide, and shown the flexibility in exchanging nanoparticles between fluorescent polystyrene beads and drug-loaded PLGA nanoparticles. The successful deposition and efficient delivery of nanoparticles to neutrophils in immune mediated diseases to the deep lung which avoid rapid clearance will facilitate development of the next generation of highly effective pulmonary drugs.

The *in vivo* work showed the lowest starting polymer concentration to fabricate the Nano-in-Micro system (20% w/v) was not rapidly phagocytosed but sustained fluorescent signal, lowering the amount of polymer needed for fabrication. Further improvements to the manufacturing method could include high throughput production of single emulsion particles with appropriate size. Potential alternatives could include microfluidic based

arrays that can be designed to process larger volumetric scales [203]. Additionally, here we showed the rapid degradation of the microgels using a single protease-responsive peptide. Different molar ratios of peptide to PEG, or percentage of degradable peptide incorporated into the backbone could be used to adjust the degradation time of the microgels to create a time-dependent release of the nanoparticles. Furthermore, a 10kDa 4-arm PEG maleimide was used in this work. If the molecular weight of the PEG backbone were increased this could increase the swelling ratio and resultant swollen size of the microgels potentially increasing the residence time of the microgels before phagocytosis.

We showed this multi-stage formulation allowed for the targeting of airway PMNs in an acute neutrophilic inflammation model, effectively delivering the immunomodulator Nexinhib20 to reduce the inflammatory cytokines released by the inflammatory neutrophils. Alternative nanoparticle formulations could also increase the loading efficiency of Nexinhib20 into the nanoparticle, which could then be used to adjust the therapeutic dose delivered by the nanoparticles. Roscovitine encapsulated into the PLGA nanoparticles with high efficiency *in vitro* and as a potent inducer of neutrophilic apoptosis would be an excellent alternative to test for therapeutic efficacy in place of Nexinhib20. Future work in chronic neutrophilic inflammation models such PGP induced inflammation would be necessary to confirm this multi-stage system is a viable therapeutic strategy for chronic airway diseases, such as CF and COPD.

The Nano-in-Microgels used throughout this work were delivered in their swollen state. For translation to a clinical system, a dry powder formulation with appropriate excipients such as lactose, mannitol, or trehalose would need to be developed and tested. Preliminary testing of excipients with microgels revealed that after lyophilization a T2

Turbula Blender would be necessary to create a free-flowing powder that could then be tested for aerodynamic properties with a next generation impactor. Larger batch processing of the Nano-in-Micro particles would also be necessary to fill capsules used with current existing pulmonary delivery devices (e.g., DPIs, nebulizers).

6.1.2 Vascularized Lung-on-a-Chip

We have shown a novel approach to developing a microvascularized lung-on-a-chip. Numerous approaches for developing either an air-liquid interface for airway epithelium or vascular networks *in vitro* have been developed. These devices have allowed for different pieces of the lung environment to be studied *in vitro* in normal and diseased states. This lung-on-a-chip that we have developed is unique since it brings together a few of these separate pieces; the lower gel allows for a 3-dimensional vasculature network to form. This endothelial space also allows for relevant stromal cells e.g., healthy or diseased fibroblasts, to be incorporated into the microfluidic device in a physiologically relevant structure—around the vasculature and below the airway epithelium. Additionally, as will be discussed later in this section, multiple different disease-like models can potentially be fabricated by exchanging the cells of interest.

The fabrication of microfluidic devices was improved by transitioning from individual microfluidic devices to a 96-well format. This increased the ease of fabrication as well as the quantity of devices that could be fabricated in a single batch. Additionally, this allowed the number of devices seeded per experiment to increase, increasing both the number of groups and higher n within each experiment. With less handling of each individual device and an increase in the rigidity of the plate structure there were overall fewer device failures over the 1-2-week cultures resulting from handling the flexible

PDMS devices (e.g., accidental bending/stretching leading to leaking in the airway channel). Further improvements to device loading such as consistent accurate cell counts, titrating the seeding density of endothelial cells for 2-3-week cultures to prevent overgrowth in the lower hydrogel channel.

However, there is still characterization that needs to be completed. Cytokine analysis of the normal devices relative to the diseased, TGFβ1 induced or iPF, would be worth studying to show if biomarkers observed in patients were replicated. Further microscopy characterization is necessary especially with the airway epithelium. We have shown preliminary tubulin IV staining that indicates cilia-like structures; however, without higher magnification imaging we have yet to determine if functional cilia form. This is necessary since these devices have not been cultured for two-week or longer cultures of ALI which is usually when fully differentiated cilia present. Furthermore, airway epithelium is a heterogeneous population and other stains such as tight junction (Z01), MUC5AC or MUC1, and club cells (uteroglobin) would be useful to our understanding the epithelial structure formation as well as the mucosal structure created in the co-cultured system. The vertical structure of these microfluidic devices is an inherent limitation for microscopy. To image in the z-plane requires objectives with 2-4 mm working distance which usually results in a lower NA. This reduces the resolution and increases depth of focus allowing more out of focus light, limiting the fine resolution imaging of intracellular structures.

Most vasculature microfluidic devices rely on the use of HUVECs. Future work moving away from HUVECs to lung-derived endothelial cells may be necessary when studying the cross-talk between epithelium and endothelium during wound repair and

fibrosis specific to iPF, acute lung injury, or COPD. However, similar to the fibroblast screen completed, screening microvasculature endothelial cells would be necessary to ensure that tubule formation occurs. Although a patient-derived microfluidic device for the testing of patient-specific response to therapies would be an ultimate target, ensuring that the troubleshooting presented in this work (fibroblast, hydrogel, or media screening) would not be necessary would require a more consistent hydrogel formulation that can promote vasculogenesis even with endothelial lots that resist vasculogenesis.

The vitrified collagen membranes have only been tested at a final 4 mg/mL concentration. Varying the concentration as well as the volume of the collagen used to create the membranes on the microphysiologic devices could adjust the thickness and quality of the membrane. Additionally, other ECM based thin film membranes including alginate and Matrigel could be used to improve this physiologically relevant membrane thus reducing the number of devices that lose the ability to maintain the air-liquid interface and promote better differentiation of the epithelial layer.

The current hydrogel is primarily a naturally-derived fibrin network which has lot-to-lot variability. This inconsistency has proven detrimental to the vitrified-collagen devices. Transitioning to a purely synthetic hydrogel would be beneficial to prevent such lot-to-lot variability as well as control the composition and signaling that the cells receive by the addition of bioactive motifs. A PEG based hydrogel may be worth investigating since a high degree of commercially available chemical modifications, molecular weights, and multi-arm products exists allowing for easy incorporation of bioactive peptide sequences as well as tethering potentially necessary angiogenic cytokines such as VEGF. The hydrogel at minimum would require the incorporation of degradable peptides for the

endothelium to restructure the network as well as adhesion motifs such as GRGDSPC. Additionally, for use with vitrified collagen membranes the mechanical properties can be tailored with more control.

Although Michael-addition type reactions have been presented throughout this work, the time constraint of the quick maleimide-thiol kinetics would make loading the microfluidic devices difficult, and an acrylate-thiol reaction would be too slow resulting in cells settling during gelation. A light-mediated thiol-ene hydrogel formulation would provide (i) controlled loading to gelation time, (ii) halved cell concentrations (hydrogel, crosslinkers, and cells in one vial) which would in turn also lead to (iii) reduced inter-device inconsistencies caused by mixing the cells/thrombin with the fibrinogen and also potentially lowering cell counting errors.

UV light-mediated systems rely on potentially cytotoxic co-initiators and monomers as well as subjecting the cells to potential damage from the light source itself. A preferred system is the visible light-mediated thiol-ene reaction with Eosin-Y as the initiator. Preliminary testing of a 4 and 6% w/v 10 kDa 4-arm PEG-norbornene (PEG-NB) with the RGD peptide and VPM degradable peptide (gift from the García lab) crosslinked via visible-light by Eosin-Y were successfully gelled in 30 seconds without cells in the individual microfluidic devices. However, the large swelling ratio of the PEG hydrogel caused the ports to bulge out into the media channels which may or may not be detrimental to the cells and vascular formation of the device. Lower molecular weight and higher armed PEG could potentially be tested to reduce the swelling ratios. Additionally, adjusting the percentage of the hydrogel that degrades, potentially designing alternative peptides that are

not as acidic, and titrating the concentration of the RGD adhesive peptide would be necessary to titrate to control the vasculature tubule formation.

Finally, there are several disease-like models that can be tested in the current state of the microphysiologic devices. For the vitrified collagen devices, the 5/0.1 Fibrin/PEG hydrogel could be used to replicate neutrophilic inflammation; the SAECs in the air-lifted airways could be treated with or without inflammatory small molecules such as LPS or LTB4, and neutrophils could be introduced in the vascular portion of the device. Exchanging the hSAECs for CF-derived patient airway epithelial cells would also allow for the creation of a CF-like microphysiologic device that could also be expanded to test neutrophilic transmigration.

For the 0.4 μm PETE based microphysiologic devices, basal to apical transmigration is not possible with the pore size and the few 10 μm pore sized devices tested would not hold the air-liquid interface. However, this microphysiologic device can be used for testing small molecule therapeutics and potential nanoparticle delivery to the apical side of the airway. Preliminary testing of hSAECs with A549s at a 1:40 ratio in the airways showed we could co-culture the adenocarcinoma cell line with the healthy cells for 5 days at ALI, small chemotherapeutics delivery routes media vs airways could be tested. Additionally, the fibrotic model presented in Chapter 5 can be characterized for fibroblast expression of α-SMA, MMP production or other inflammatory cytokines released to determine the extent of fibrosis recapitulated.

This dissertation has investigated a multi-stage system for the delivery of therapeutics to respiratory airways and developed a microphysiologic device to recapitulate

the vascularized epithelium for future use in creating airway disease models to streamline therapeutic testing.

REFERENCES

[1] J. Balhara, A.S. Gounni, The alveolar macrophages in asthma: a double-edged sword, Mucosal Immunol. 5 (2012) 605–609. doi:10.1038/mi.2012.74.

[2] B.N. Lambrecht, H. Hammad, The immunology of asthma, Nat. Immunol. 16 (2015) 45–56. doi:10.1038/ni.3049.

[3] P.J. Barnes, Inflammatory mechanisms in patients with chronic obstructive pulmonary disease, J. Allergy Clin. Immunol. 138 (2016) 16–27. doi:10.1016/J.JACI.2016.05.011.

[4] C. Castellani, B.M. Assael, Cystic fibrosis: a clinical view, Cell. Mol. Life Sci. 74 (2016) 1–12. doi:10.1007/s00018-016-2393-9.

[5] F. Ratjen, S.C. Bell, S.M. Rowe, C.H. Goss, A.L. Quittner, A. Bush, Cystic fibrosis, Nat. Rev. Dis. Prim. 1 (2015) 15010. doi:10.1038/nrdp.2015.10.

[6] I.D. Pavord, P. Chanez, G.J. Criner, H.A.M. Kerstjens, S. Korn, N. Lugogo, J.-B. Martinot, H. Sagara, F.C. Albers, E.S. Bradford, S.S. Harris, B. Mayer, D.B. Rubin, S.W. Yancey, F.C. Sciurba, Mepolizumab for Eosinophilic Chronic Obstructive Pulmonary Disease, N. Engl. J. Med. 377 (2017) 1613–1629. doi:10.1056/NEJMoa1708208.

[7] C.E. Brightling, W. Monteiro, R. Ward, D. Parker, M.D. Morgan, A.J. Wardlaw, I.D. Pavord, Sputum eosinophilia and short-term response to prednisolone in chronic obstructive pulmonary disease: a randomised controlled trial, Lancet. 356 (2000) 1480–1485. doi:10.1016/S0140-6736(00)02872-5.

[8] T.W. Shen, C.A. Fromen, M.P. Kai, J.C. Luft, T.B. Rahhal, G.R. Robbins, J.M. DeSimone, Distribution and Cellular Uptake of PEGylated Polymeric Particles in the Lung Towards Cell-Specific Targeted Delivery, Pharm. Res. 32 (2015) 3248–3260. doi:10.1007/s11095-015-1701-7.

[9] A. Popov, L. Schopf, J. Bourassa, H. Chen, Enhanced pulmonary delivery of fluticasone propionate in rodents by mucus-penetrating nanoparticles, Int. J. Pharm. 502 (2016) 188–197. doi:10.1016/j.ijpharm.2016.02.031.

[10] N. Nafee, A. Husari, C.K. Maurer, C. Lu, C. De Rossi, A. Steinbach, R.W. Hartmann, C.M. Lehr, M. Schneider, Antibiotic-free nanotherapeutics: Ultra-small, mucus-penetrating solid lipid nanoparticles enhance the pulmonary delivery and anti-virulence efficacy of novel quorum sensing inhibitors, J. Control. Release. 192 (2014) 131–140. doi:10.1016/j.jconrel.2014.06.055.

[11] S. Zhang, H. Gao, G. Bao, Physical Principles of Nanoparticle Cellular Endocytosis, ACS Nano. 9 (2015) 8655–8671. doi:10.1021/acsnano.5b03184.

[12] C.S. Schneider, Q. Xu, N.J. Boylan, J. Chisholm, B.C. Tang, B.S. Schuster, A. Henning, L.M. Ensign, E. Lee, P. Adstamongkonkul, B.W. Simons, S.-Y.S. Wang, X. Gong, T. Yu, M.P. Boyle, J.S. Suk, J. Hanes, Nanoparticles that do not adhere to mucus provide uniform and long-lasting drug delivery to airways following inhalation, Sci. Adv. 3 (2017). doi:10.1126/sciadv.1601556.

[13] A. Kolte, S. Patil, P. Lesimple, J.W. Hanrahan, A. Misra, PEGylated composite nanoparticles of PLGA and polyethylenimine for safe and efficient delivery of pDNA to lungs, Int. J. Pharm. 524 (2017) 382–396. doi:10.1016/J.IJPHARM.2017.03.094.

[14] X. Murgia, P. Pawelzyk, U.F. Schaefer, C. Wagner, N. Willenbacher, C.-M. Lehr, Size-Limited Penetration of Nanoparticles into Porcine Respiratory Mucus after Aerosol Deposition, Biomacromolecules. 17 (2016) 1536–1542. doi:10.1021/acs.biomac.6b00164.

[15] J. Heyder, L. Armbruster, J. Gebhart, E. Grein, W. Stahlhofen, Total deposition of aerosol particles in the human respiratory tract for nose and mouth breathing, J. Aerosol Sci. 6 (1975) 311–328. doi:10.1016/0021-8502(75)90020-8.

[16] D.A. Edwards, C. Dunbar, Bioengineering of Therapeutic Aerosols, Annu. Rev. Biomed. Eng. 4 (2002) 93–107. doi:10.1146/annurev.bioeng.4.100101.132311.

[17] B. Patel, N. Gupta, F. Ahsan, Particle engineering to enhance or lessen particle uptake by alveolar macrophages and to influence the therapeutic outcome, Eur. J. Pharm. Biopharm. 89 (2015) 163–174. doi:10.1016/j.ejpb.2014.12.001.

[18] F.J. Martinez, H.R. Collard, A. Pardo, G. Raghu, L. Richeldi, M. Selman, J.J. Swigris, H. Taniguchi, A.U. Wells, Idiopathic pulmonary fibrosis, Nat. Rev. Dis. Prim. 3 (2017) 17074. doi:10.1038/nrdp.2017.74.

[19] J. Tashiro, G.A. Rubio, A.H. Limper, K. Williams, S.J. Elliot, I. Ninou, V. Aidinis, A. Tzouvelekis, M.K. Glassberg, Exploring Animal Models That Resemble Idiopathic Pulmonary Fibrosis., Front. Med. 4 (2017) 118. doi:10.3389/fmed.2017.00118.

[20] J.T. Fisher, Y. Zhang, J.F. Engelhardt, Comparative biology of cystic fibrosis animal models., Methods Mol. Biol. 742 (2011) 311–334. doi:10.1007/978-1-61779-120-8_19.

[21] G.M. Lavelle, M.M. White, N. Browne, N.G. McElvaney, E.P. Reeves, Animal Models of Cystic Fibrosis Pathology: Phenotypic Parallels and Divergences, Biomed Res. Int. 2016 (2016). doi:10.1155/2016/5258727.

[22] Geneva: World Health Organization, Noncommunicable diseases country profiles 2018, World Health Organization, 2018. https://www.who.int/nmh/publications/ncd-profiles-2018/en/.

[23] L. Finney, M. Berry, A. Singanayagam, S.L. Elkin, S.L. Johnston, P. Mallia, Inhaled corticosteroids and pneumonia in chronic obstructive pulmonary disease, Lancet Respir. Med. 2 (2014) 919–932. doi:10.1016/S2213-2600(14)70169-9.

[24] P. Markart, R. Nass, C. Ruppert, L. Hundack, M. Wygrecka, M. Korfei, R.H. Boedeker, G. Staehler, H. Kroll, G. Scheuch, W. Seeger, A. Guenther, Safety and Tolerability of Inhaled Heparin in Idiopathic Pulmonary Fibrosis, J. Aerosol Med. Pulm. Drug Deliv. 23 (2010) 161–172. doi:10.1089/jamp.2009.0780.

[25] M. Cazzola, P. Rogliani, L. Calzetta, M.G. Matera, Triple therapy versus single and dual long-acting bronchodilator therapy in COPD: a systematic review and meta-analysis., Eur. Respir. J. 52 (2018) 1801586. doi:10.1183/13993003.01586-2018.

[26] L. Panda, U. Mabalirajan, Recent Updates on Corticosteroid Resistance in Asthma, n.d. https://emj.europeanmedical-group.com/wp-content/uploads/sites/2/2018/09/Recent-Updates-on....pdf (accessed April 18, 2019).

[27] S. Homma, A. Azuma, H. Taniguchi, T. Ogura, Y. Mochiduki, Y. Sugiyama, K. Nakata, K. Yoshimura, M. Takeuchi, S. Kudoh, Efficacy of inhaled N-acetylcysteine monotherapy in patients with early stage idiopathic pulmonary fibrosis, Respirology. 17 (2012) 467–477. doi:10.1111/j.1440-1843.2012.02132.x.

[28] J.M. Leung, D.D. Sin, Inhaled corticosteroids in COPD: the final verdict is…, Eur. Respir. J. 52 (2018) 1801940. doi:10.1183/13993003.01940-2018.

[29] H. Heijerman, E. Westerman, S. Conway, D. Touw, G. Döring, consensus working group, Inhaled medication and inhalation devices for lung disease in patients with cystic fibrosis: A European consensus, J. Cyst. Fibros. 8 (2009) 295–315. doi:10.1016/j.jcf.2009.04.005.

[30] L. Richeldi, R.M. du Bois, G. Raghu, A. Azuma, K.K. Brown, U. Costabel, V. Cottin, K.R. Flaherty, D.M. Hansell, Y. Inoue, D.S. Kim, M. Kolb, A.G. Nicholson, P.W. Noble, M. Selman, H. Taniguchi, M. Brun, F. Le Maulf, M. Girard, S. Stowasser, R. Schlenker-Herceg, B. Disse, H.R. Collard, Efficacy and Safety of

Nintedanib in Idiopathic Pulmonary Fibrosis, N. Engl. J. Med. 370 (2014) 2071–2082. doi:10.1056/NEJMoa1402584.

[31] K. Ahmad, S.D. Nathan, Novel management strategies for idiopathic pulmonary fibrosis, Expert Rev. Respir. Med. 12 (2018) 831–842. doi:10.1080/17476348.2018.1513332.

[32] H.R. Collard, L. Richeldi, S. Cerri, P. Spagnolo, F. Luppi, G. Sgalla, L. Richeldi, Management of Idiopathic Pulmonary Fibrosis, Interstitial Lung Dis. (2018) 55–63. doi:10.1016/B978-0-323-48024-6.00004-5.

[33] B. Ley, H.R. Collard, T.E. King, Clinical Course and Prediction of Survival in Idiopathic Pulmonary Fibrosis, Am. J. Respir. Crit. Care Med. 183 (2011) 431–440. doi:10.1164/rccm.201006-0894CI.

[34] G. Hughes, H. Toellner, H. Morris, C. Leonard, N. Chaudhuri, G. Hughes, H. Toellner, H. Morris, C. Leonard, N. Chaudhuri, Real World Experiences: Pirfenidone and Nintedanib are Effective and Well Tolerated Treatments for Idiopathic Pulmonary Fibrosis, J. Clin. Med. 5 (2016) 78. doi:10.3390/jcm5090078.

[35] T.E. King, W.Z. Bradford, S. Castro-Bernardini, E.A. Fagan, I. Glaspole, M.K. Glassberg, E. Gorina, P.M. Hopkins, D. Kardatzke, L. Lancaster, D.J. Lederer, S.D. Nathan, C.A. Pereira, S.A. Sahn, R. Sussman, J.J. Swigris, P.W. Noble, A Phase 3 Trial of Pirfenidone in Patients with Idiopathic Pulmonary Fibrosis, N. Engl. J. Med. 370 (2014) 2083–2092. doi:10.1056/NEJMoa1402582.

[36] L. Richeldi, V. Cottin, R.M. du Bois, M. Selman, T. Kimura, Z. Bailes, R. Schlenker-Herceg, S. Stowasser, K.K. Brown, Nintedanib in patients with idiopathic pulmonary fibrosis: Combined evidence from the TOMORROW and INPULSIS® trials, Respir. Med. 113 (2016) 74–79. doi:10.1016/J.RMED.2016.02.001.

[37] J.C. Sung, B.L. Pulliam, D.A. Edwards, Nanoparticles for drug delivery to the lungs, Trends Biotechnol. 25 (2007) 563–570. doi:https://doi.org/10.1016/j.tibtech.2007.09.005.

[38] R.O. Williams, T.C. Carvalho, J.I. Peters, R.O. Williams, T.C. Carvalho, J.I. Peters, Influence of particle size on regional lung deposition - What evidence is there?, Int. J. Pharm. 406 (2011) 1–10. doi:10.1016/j.ijpharm.2010.12.040.

[39] G. Pilcer, K. Amighi, Formulation strategy and use of excipients in pulmonary drug delivery, Int. J. Pharm. 392 (2010) 1–19. doi:10.1016/J.IJPHARM.2010.03.017.

[40] D.A. Edwards, J. Hanes, G. Caponetti, J. Hrkach, A. BenJebria, M. Lou Eskew, J. Mintzes, D. Deaver, N. Lotan, R. Langer, A. Ben-jebria, M. Lou Eskew, J. Mintzes, D. Deaver, N. Lotan, R. Langer, Large Porous Particles for Pulmonary Drug Delivery, Science (80-.). 276 (1997) 1868–1871. doi:10.1126/science.276.5320.1868.

[41] J. Heyder, J. Gebhart, G. Rudolf, C.F. Schiller, W. Stahlhofen, Deposition of particles in the human respiratory tract in the size range 0.005-15 μm, J. Aerosol Sci. 17 (1986) 811–825. doi:10.1016/0021-8502(86)90035-2.

[42] J.S. Brown, D. Ph, K.L. Zeman, W.D. Bennett, Distribution in Healthy Subjects and Patients, 14 (2001) 443–454.

[43] J. Ma, B.K. Rubin, J.A. Voynow, Mucins, Mucus, and Goblet Cells, Chest. 154 (2018) 169–176. doi:10.1016/J.CHEST.2017.11.008.

[44] J.A. Whitsett, T. Alenghat, Respiratory epithelial cells orchestrate pulmonary innate immunity, Nat. Immunol. 16 (2015) 27–35. doi:10.1038/ni.3045.

[45] W.J. Janssen, A.L. Stefanski, B.S. Bochner, C.M. Evans, Control of lung defence by mucins and macrophages: ancient defence mechanisms with modern functions, Eur Respir J. 48 (2016) 1201–1214. doi:10.1183/13993003.00120-2015.

[46] I. Lakshmanan, M.P. Ponnusamy, M.A. Macha, D. Haridas, P.D. Majhi, S. Kaur, M. Jain, S.K. Batra, A.K. Ganti, Mucins in Lung Cancer: Diagnostic, Prognostic, and Therapeutic Implications, J. Thorac. Oncol. 10 (2015) 19–27. doi:10.1097/JTO.0000000000000404.

[47] B. Button, L.-H. Cai, C. Ehre, M. Kesimer, D.B. Hill, J.K. Sheehan, R.C. Boucher, M. Rubinstein, A periciliary brush promotes the lung health by separating the mucus layer from airway epithelia., Science. 337 (2012) 937–41. doi:10.1126/science.1223012.

[48] K.G. Welsh, K. Rousseau, G. Fisher, L.R. Bonser, P. Bradding, C.E. Brightling, D.J. Thornton, E.A. Gaillard, MUC5AC and a Glycosylated Variant of MUC5B Alter Mucin Composition in Children With Acute Asthma, Chest. 152 (2017) 771–779. doi:10.1016/J.CHEST.2017.07.001.

[49] J. Zhao, B. Maskrey, S. Balzar, K. Chibana, A. Mustovich, H. Hu, J.B. Trudeau, V. O'Donnell, S.E. Wenzel, Interleukin-13–induced MUC5AC Is Regulated by 15-Lipoxygenase 1 Pathway in Human Bronchial Epithelial Cells, Am. J. Respir. Crit. Care Med. 179 (2009) 782–790. doi:10.1164/rccm.200811-1744OC.

[50] J.M. Flynn, D. Niccum, J.M. Dunitz, R.C. Hunter, Evidence and Role for Bacterial Mucin Degradation in Cystic Fibrosis Airway Disease, PLOS Pathog. 12 (2016) e1005846. doi:10.1371/journal.ppat.1005846.

[51] Y. Xie, L. Ostedgaard, M.H. Abou Alaiwa, L. Lu, A.J. Fischer, D.A. Stoltz, Mucociliary Transport in Healthy and Cystic Fibrosis Pig Airways, Ann. Am. Thorac. Soc. 15 (2018) S171–S176. doi:10.1513/AnnalsATS.201805-308AW.

[52] G.Z. Ng, P. Sutton, The MUC1 mucin specifically inhibits activation of the NLRP3 inflammasome, Genes Immun. 17 (2016) 203–206. doi:10.1038/gene.2016.10.

[53] W.-C. Huang, M.-L. Chan, M.-J. Chen, T.-H. Tsai, Y.-J. Chen, Modulation of macrophage polarization and lung cancer cell stemness by MUC1 and development of a related small-molecule inhibitor pterostilbene., Oncotarget. 7 (2016) 39363–39375. doi:10.18632/oncotarget.8101.

[54] J. Zhai, M. Insel, K.J. Addison, D.A. Stern, W. Pederson, A. Dy, J. Rojas-Quintero, C.A. Owen, D.L. Sherrill, W. Morgan, A.L. Wright, M. Halonen, F.D. Martinez, M. Kraft, S. Guerra, J.G. Ledford, Club Cell Secretory Protein Deficiency Leads to Altered Lung Function, (2019). doi:10.1164/rccm.201807-1345OC.

[55] M.E. Laucho-Contreras, F. Polverino, K. Gupta, K.L. Taylor, E. Kelly, V. Pinto-Plata, M. Divo, N. Ashfaq, H. Petersen, B. Stripp, A.L. Pilon, Y. Tesfaigzi, B.R. Celli, C.A. Owen, Protective role for club cell secretory protein-16 (CC16) in the development of COPD, Eur Respir J. 45 (2015) 1544–1556. doi:10.1183/09031936.00010515.

[56] H.Y. Park, A. Churg, J.L. Wright, Y. Li, S. Tam, S.F.P. Man, D. Tashkin, R.A. Wise, J.E. Connett, D.D. Sin, Club cell protein 16 and disease progression in chronic obstructive pulmonary disease., Am. J. Respir. Crit. Care Med. 188 (2013) 1413–9. doi:10.1164/rccm.201305-0892OC.

[57] C. Conti, A. Montero-Fernandez, E. Borg, T. Osadolor, P. Viola, A. De Lauretis, C.J. Stock, M. Bonifazi, M. Bonini, G. Caramori, G. Lindahl, F.B. Blasi, A.G. Nicholson, A.U. Wells, P. Sestini, E. Renzoni, Mucins MUC5B and MUC5AC in Distal Airways and Honeycomb Spaces: Comparison among Idiopathic Pulmonary Fibrosis/Usual Interstitial Pneumonia, Fibrotic Nonspecific Interstitial Pneumonitis, and Control Lungs, Am. J. Respir. Crit. Care Med. 193 (2016) 462–464. doi:10.1164/rccm.201507-1322LE.

[58] A. Crabbe, M.A. Ledesma, C.A. Nickerson, Mimicking the host and its microenvironment in vitro for studying mucosal infections by Pseudomonas aeruginosa, Pathog. Dis. 71 (2014) 1–19. doi:10.1111/2049-632X.12180.Mimicking.

[59] F. Taherali, F. Varum, A.W. Basit, A slippery slope: On the origin, role and physiology of mucus, Adv. Drug Deliv. Rev. 124 (2018) 16–33. doi:10.1016/J.ADDR.2017.10.014.

[60] S. Dunnhaupt, O. Kammona, C. Waldner, C. Kiparissides, A. Bernkop-Schnurch, Nano-carrier systems: Strategies to overcome the mucus gel barrier, Eur. J. Pharm. Biopharm. 96 (2015) 447–453. doi:10.1016/j.ejpb.2015.01.022.

[61] B.S. Quon, S.M. Rowe, New and emerging targeted therapies for cystic fibrosis, 352 (2016). doi:10.1136/bmj.i859.

[62] S.D. Sagel, B.D. Wagner, M.M. Anthony, P. Emmett, E.T. Zemanick, Sputum biomarkers of inflammation and lung function decline in children with cystic fibrosis, Am. J. Respir. Crit. Care Med. 186 (2012) 857–865. doi:10.1164/rccm.201203-0507OC.

[63] Y.Y. Wang, S.K. Lai, J.S. Suk, A. Pace, R. Cone, J. Hanes, Addressing the PEG mucoadhesivity paradox to engineer nanoparticles that “slip” through the human mucus barrier, Angew. Chemie - Int. Ed. 47 (2008) 9726–9729. doi:10.1002/anie.200803526.

[64] P. Mastorakos, A.L. da Silva, J. Chisholm, E. Song, W.K. Choi, M.P. Boyle, M.M. Morales, J. Hanes, J.S. Suk, Highly compacted biodegradable DNA nanoparticles capable of overcoming the mucus barrier for inhaled lung gene therapy, Proc. Natl. Acad. Sci. 112 (2015) 201502281. doi:10.1073/pnas.1502281112.

[65] M. Kopf, C. Schneider, S.P. Nobs, The development and function of lung-resident macrophages and dendritic cells, Nat. Immunol. 16 (2015) 36–44. doi:10.1038/ni.3052.

[66] A. Shapouri-Moghaddam, S. Mohammadian, H. Vazini, M. Taghadosi, S.-A. Esmaeili, F. Mardani, B. Seifi, A. Mohammadi, J.T. Afshari, A. Sahebkar, Macrophage plasticity, polarization, and function in health and disease, J. Cell. Physiol. 233 (2018) 6425–6440. doi:10.1002/jcp.26429.

[67] S.Y.S. Tan, M.A. Krasnow, Developmental origin of lung macrophage diversity., Development. 143 (2016) 1318–27. doi:10.1242/dev.129122.

[68] D. Bedoret, H. Wallemacq, T. Marichal, C. Desmet, F.Q. Calvo, E. Henry, R. Closset, B. Dewals, C. Thielen, P. Gustin, L. de Leval, N. Van Rooijen, A. Le Moine, A. Vanderplasschen, D. Cataldo, P.-V. Drion, M. Moser, P. Lekeux, F. Bureau, Lung interstitial macrophages alter dendritic cell functions to prevent airway allergy in mice, J. Clin. Invest. 119 (2009) 3723–3738. doi:10.1172/JCI39717.

[69] J. Hoppstädter, B. Diesel, R. Zarbock, T. Breinig, D. Monz, M. Koch, A. Meyerhans, L. Gortner, C.-M. Lehr, H. Huwer, A.K. Kiemer, Differential cell reaction upon Toll-like receptor 4 and 9 activation in human alveolar and lung interstitial macrophages, Respir. Res. 11 (2010) 124. doi:10.1186/1465-9921-11-124.

[70] G. Franke-Ullmann, C. Pförtner, P. Walter, C. Steinmüller, M.L. Lohmann-Matthes, L. Kobzik, Characterization of murine lung interstitial macrophages in comparison with alveolar macrophages in vitro., J. Immunol. 157 (1996) 3097–104. http://www.ncbi.nlm.nih.gov/pubmed/8816420.

[71] T. Hussell, T.J. Bell, Alveolar macrophages: plasticity in a tissue-specific context, Nat. Rev. Immunol. 14 (2014) 81–93. doi:10.1038/nri3600.

[72] K. Westphalen, G.A. Gusarova, M.N. Islam, M. Subramanian, T.S. Cohen, A.S. Prince, J. Bhattacharya, Sessile alveolar macrophages communicate with alveolar epithelium to modulate immunity, Nature. 506 (2014) 503–506. doi:10.1038/nature12902.

[73] B. Beck-Schimmer, R. Schwendener, T. Pasch, L. Reyes, C. Booy, R.C. Schimmer, Alveolar macrophages regulate neutrophil recruitment in endotoxin-induced lung injury., Respir. Res. 6 (2005) 61. doi:10.1186/1465-9921-6-61.

[74] W.-H. Lee, C.-Y. Loo, D. Traini, P.M. Young, Expert Opinion on Drug Delivery Nano-and micro-based inhaled drug delivery systems for targeting alveolar macrophages, (2015). doi:10.1517/17425247.2015.1039509.

[75] K. Hirota, T. Hasegawa, H. Hinata, F. Ito, H. Inagawa, C. Kochi, G.-I. Soma, K. Makino, H. Terada, Optimum conditions for efficient phagocytosis of rifampicin-loaded PLGA microspheres by alveolar macrophages, (2007). doi:10.1016/j.jconrel.2007.01.013.

[76] A. Garapaty, J.A. Champion, Tunable particles alter macrophage uptake based on combinatorial effects of physical properties, Bioeng. Transl. Med. 2 (2016) 92–101. doi:10.1002/btm2.10047.

[77] I. D'Angelo, B. Perfetto, G. Costabile, V. Ambrosini, P. Caputo, A. Miro, R. D'Emmanuele Di Villa Bianca, R. Sorrentino, G. Donnarumma, F. Quaglia, F. Ungaro, Large Porous Particles for Sustained Release of a Decoy Oligonucelotide and Poly(ethylenimine): Potential for Combined Therapy of Chronic Pseudomonas aeruginosa Lung Infections, Biomacromolecules. 17 (2016) 1561–1571. doi:10.1021/acs.biomac.5b01646.

[78] S. Nishimura, T. Takami, Y. Murakami, Porous PLGA microparticles formed by “one-step” emulsification for pulmonary drug delivery: The surface morphology and the aerodynamic properties, Colloids Surfaces B Biointerfaces. 159 (2017) 318–326. doi:10.1016/j.colsurfb.2017.08.004.

[79] P. Wanakule, G.W. Liu, A.T. Fleury, K. Roy, Nano-inside-micro: Disease-responsive microgels with encapsulated nanoparticles for intracellular drug delivery to the deep lung, J. Control. Release. 162 (2012) 429–437. doi:10.1016/j.jconrel.2012.07.026.

[80] R. Ni, J. Zhao, Q. Liu, Z. Liang, U. Muenster, S. Mao, Nanocrystals embedded in chitosan-based respirable swellable microparticles as dry powder for sustained pulmonary drug delivery, Eur. J. Pharm. Sci. 99 (2017) 137–146. doi:10.1016/j.ejps.2016.12.013.

[81] I.M. El-Sherbiny, H.D.C. Smyth, Biodegradable nano-micro carrier systems for sustained pulmonary drug delivery: (I) Self-assembled nanoparticles encapsulated in respirable/swellable semi-IPN microspheres, Int. J. Pharm. 395 (2010) 132–141. doi:10.1016/j.ijpharm.2010.05.032.

[82] E. Secret, S.J. Kelly, K.E. Crannell, J.S. Andrew, Enzyme-Responsive Hydrogel Microparticles for Pulmonary Drug Delivery, ACS Appl. Mater. Interfaces. 6 (2014) 10313–10321. doi:10.1021/am501754s.

[83] M.D. Bhavsar, M.M. Amiji, Gastrointestinal distribution and in vivo gene transfection studies with nanoparticles-in-microsphere oral system (NiMOS), 119 (2007) 339–348. doi:10.1016/j.jconrel.2007.03.006.

[84] J.C. Imperiale, P. Nejamkin, J. Maria, C.E. Lanusse, A. Sosnik, Biomaterials Novel protease inhibitor-loaded Nanoparticle-in-Microparticle Delivery System leads to a dramatic improvement of the oral pharmacokinetics in dogs, 37 (2015) 383–394.

[85] M.P. Lutolf, J.L. Lauer-Fields, H.G. Schmoekel, A.T. Metters, F.E. Weber, G.B. Fields, J.A. Hubbell, Synthetic matrix metalloproteinase-sensitive hydrogels for the conduction of tissue regeneration: engineering cell-invasion characteristics., Proc. Natl. Acad. Sci. U. S. A. 100 (2003) 5413–8. doi:10.1073/pnas.0737381100.

[86] J. Patterson, J.A. Hubbell, Enhanced proteolytic degradation of molecularly engineered PEG hydrogels in response to MMP-1 and MMP-2, Biomaterials. 31 (2010) 7836–7845. doi:10.1016/J.BIOMATERIALS.2010.06.061.

[87] G.A. Foster, D.M. Headen, C. González-García, M. Salmerón-Sánchez, H. Shirwan, A.J. García, Protease-degradable microgels for protein delivery for

vascularization., Biomaterials. 113 (2017) 170–175. doi:10.1016/j.biomaterials.2016.10.044.

[88] A.A. Aimetti, M.W. Tibbitt, K.S. Anseth, A.A. Aimetti, M.W. Tibbitt, K.S. Anseth, Human Neutrophil Elastase Responsive Delivery from Poly(ethylene glycol) Hydrogels, Biomacromolecules. 10 (2009) 1484–1489.

[89] S. Kolahian, I.E. Fernandez, O. Eickelberg, D. Hartl, Immune mechanisms in pulmonary fibrosis, Am. J. Respir. Cell Mol. Biol. 55 (2016) 309–322. doi:10.1165/rcmb.2016-0121TR.

[90] C.J. Wagner, C. Schultz, M.A. Mall, Neutrophil elastase and matrix metalloproteinase 12 in cystic fibrosis lung disease, Mol. Cell. Pediatr. 3 (2016) 25. doi:10.1186/s40348-016-0053-7.

[91] A.S. Dittrich, I. Kühbandner, S. Gehrig, V. Rickert-Zacharias, M. Twigg, S. Wege, C.C. Taggart, F. Herth, C. Schultz, M.A. Mall, Elastase activity on sputum neutrophils correlates with severity of lung disease in cystic fibrosis, Eur. Respir. J. 51 (2018) 1701910. doi:10.1183/13993003.01910-2017.

[92] K. Hoenderdos, A. Condliffe, The neutrophil in chronic obstructive pulmonary disease, Am J Respir Cell Mol Biol. 48 (2013) 531–539. doi:10.1165/rcmb.2012-0492TR.

[93] M.W. Tibbitt, K.S. Anseth, Hydrogels as extracellular matrix mimics for 3D cell culture., Biotechnol. Bioeng. 103 (2009) 655–63. doi:10.1002/bit.22361.

[94] S.R. Caliari, J.A. Burdick, A practical guide to hydrogels for cell culture, Nat. Methods. 13 (2016) 405–414. doi:10.1038/nmeth.3839.

[95] O. Chaudhuri, L. Gu, D. Klumpers, M. Darnell, S.A. Bencherif, J.C. Weaver, N. Huebsch, H. Lee, E. Lippens, G.N. Duda, D.J. Mooney, Hydrogels with tunable stress relaxation regulate stem cell fate and activity, Nat. Mater. (2015). doi:10.1038/nmat4489.

[96] R.H. Schmedlen, K.S. Masters, J.L. West, Photocrosslinkable polyvinyl alcohol hydrogels that can be modified with cell adhesion peptides for use in tissue engineering, Biomaterials. 23 (2002) 4325–4332. doi:10.1016/S0142-9612(02)00177-1.

[97] C. Arakawa, R. Ng, S. Tan, S. Kim, B. Wu, M. Lee, Photopolymerizable chitosan-collagen hydrogels for bone tissue engineering, J. Tissue Eng. Regen. Med. 11 (2017) 164–174. doi:10.1002/term.1896.

[98] R. Jin, L.S. Moreira Teixeira, P.J. Dijkstra, M. Karperien, C.A. van Blitterswijk, Z.Y. Zhong, J. Feijen, Injectable chitosan-based hydrogels for cartilage tissue engineering, Biomaterials. 30 (2009) 2544–2551. doi:10.1016/J.BIOMATERIALS.2009.01.020.

[99] M.A. Kalam, Development of chitosan nanoparticles coated with hyaluronic acid for topical ocular delivery of dexamethasone, Int. J. Biol. Macromol. 89 (2016) 127–136. doi:10.1016/J.IJBIOMAC.2016.04.070.

[100] A. Trapani, S. Di Gioia, N. Ditaranto, N. Cioffi, F.M. Goycoolea, A. Carbone, M. Garcia-Fuentes, M. Conese, M.J. Alonso, Systemic heparin delivery by the pulmonary route using chitosan and glycol chitosan nanoparticles, Int. J. Pharm. 447 (2013) 115–123. doi:10.1016/J.IJPHARM.2013.02.035.

[101] J. Berger, M. Reist, J.M. Mayer, O. Felt, N.A. Peppas, R. Gurny, Structure and interactions in covalently and ionically crosslinked chitosan hydrogels for biomedical applications, Eur. J. Pharm. Biopharm. 57 (2004) 19–34. doi:10.1016/S0939-6411(03)00161-9.

[102] N.C. Silva, S. Silva, B. Sarmento, M. Pintado, Chitosan nanoparticles for daptomycin delivery in ocular treatment of bacterial endophthalmitis, Drug Deliv. 22 (2015) 885–893. doi:10.3109/10717544.2013.858195.

[103] H.V. Almeida, R. Eswaramoorthy, G.M. Cunniffe, C.T. Buckley, F.J. O'Brien, D.J. Kelly, Fibrin hydrogels functionalized with cartilage extracellular matrix and incorporating freshly isolated stromal cells as an injectable for cartilage regeneration, Acta Biomater. 36 (2016) 55–62. doi:10.1016/J.ACTBIO.2016.03.008.

[104] A.W. Peterson, D.J. Caldwell, A.Y. Rioja, R.R. Rao, A.J. Putnam, J.P. Stegemann, Vasculogenesis and Angiogenesis in Modular Collagen-Fibrin Microtissues, Biomater. Sci. 2 (2014) 1497. doi:10.1039/C4BM00141A.

[105] J.J. Moon, J.E. Saik, R.A. Poché, J.E. Leslie-Barbick, S.-H. Lee, A.A. Smith, M.E. Dickinson, J.L. West, Biomimetic hydrogels with pro-angiogenic properties., Biomaterials. 31 (2010) 3840–7. doi:10.1016/j.biomaterials.2010.01.104.

[106] Y.-B. Lee, S. Polio, W. Lee, G. Dai, L. Menon, R.S. Carroll, S.-S. Yoo, Bio-printing of collagen and VEGF-releasing fibrin gel scaffolds for neural stem cell culture, Exp. Neurol. 223 (2010) 645–652. doi:10.1016/J.EXPNEUROL.2010.02.014.

[107] J.S. Jeon, S. Bersini, J.A. Whisler, M.B. Chen, G. Dubini, J.L. Charest, M. Moretti, R.D. Kamm, Generation of 3D functional microvascular networks with human mesenchymal stem cells in microfluidic systems., Integr. Biol. (Camb). 6 (2014) 555–63. doi:10.1039/c3ib40267c.

[108] R. Narayan, T. Agarwal, D. Mishra, T.K. Maiti, S. Mohanty, Goat tendon collagen-human fibrin hydrogel for comprehensive parametric evaluation of HUVEC microtissue-based angiogenesis, Colloids Surfaces B Biointerfaces. 163 (2018) 291–300. doi:10.1016/J.COLSURFB.2017.12.056.

[109] R.R. Rao, A.W. Peterson, J. Ceccarelli, A.J. Putnam, J.P. Stegemann, Matrix composition regulates three-dimensional network formation by endothelial cells and mesenchymal stem cells in collagen/fibrin materials, Angiogenesis. 15 (2012) 253–264. doi:10.1007/s10456-012-9257-1.

[110] M.A. Ruehle, M.-T.A. Li, A. Cheng, L. Krishnan, N.J. Willett, R.E. Guldberg, Decorin-supplemented collagen hydrogels for the co-delivery of bone morphogenetic protein-2 and microvascular fragments to a composite bone-muscle injury model with impaired vascularization, Acta Biomater. (2019). doi:10.1016/J.ACTBIO.2019.01.045.

[111] T.H. Kim, D.B. An, S.H. Oh, M.K. Kang, H.H. Song, J.H. Lee, Creating stiffness gradient polyvinyl alcohol hydrogel using a simple gradual freezing–thawing method to investigate stem cell differentiation behaviors, Biomaterials. 40 (2015) 51–60. doi:10.1016/J.BIOMATERIALS.2014.11.017.

[112] M. Morille, K. Toupet, C.N. Montero-Menei, C. Jorgensen, D. Noël, PLGA-based microcarriers induce mesenchymal stem cell chondrogenesis and stimulate cartilage repair in osteoarthritis, Biomaterials. 88 (2016) 60–69. doi:10.1016/J.BIOMATERIALS.2016.02.022.

[113] O.M. Benavides, A.R. Brooks, S.K. Cho, J. Petsche Connell, R. Ruano, J.G. Jacot, In situ vascularization of injectable fibrin/poly(ethylene glycol) hydrogels by human amniotic fluid-derived stem cells, J. Biomed. Mater. Res. Part A. 103 (2015) 2645–2653. doi:10.1002/jbm.a.35402.

[114] A. Popov, E. Enlow, J. Bourassa, H. Chen, Mucus-penetrating nanoparticles made with “mucoadhesive” poly(vinyl alcohol), Nanomedicine Nanotechnology, Biol. Med. 12 (2016) 1863–1871. doi:10.1016/J.NANO.2016.04.006.

[115] L.C. Roudsari, S.E. Jeffs, A.S. Witt, B.J. Gill, J.L. West, A 3D Poly(ethylene glycol)-based Tumor Angiogenesis Model to Study the Influence of Vascular Cells on Lung Tumor Cell Behavior, Sci. Rep. 6 (2016) 32726. doi:10.1038/srep32726.

[116] J.L. Drury, D.J. Mooney, Hydrogels for tissue engineering: scaffold design variables and applications, Biomaterials. 24 (2003) 4337–4351. doi:10.1016/S0142-9612(03)00340-5.

[117] † and Andrew Metters*, J. Hubbell‡, Network Formation and Degradation Behavior of Hydrogels Formed by Michael-Type Addition Reactions, (2004). doi:10.1021/BM049607O.

[118] S. Nam, R. Stowers, J. Lou, Y. Xia, O. Chaudhuri, Varying PEG density to control stress relaxation in alginate-PEG hydrogels for 3D cell culture studies, Biomaterials. 200 (2019) 15–24. doi:10.1016/J.BIOMATERIALS.2019.02.004.

[119] M. Fisher, S.D. Nathan, C. Hill, J. Marshall, F. Dejonckheere, P.-O. Thuresson, T.M. Maher, Predicting Life Expectancy for Pirfenidone in Idiopathic Pulmonary Fibrosis, J. Manag. Care Spec. Pharm. 23 (2017) S17–S24. doi:10.18553/jmcp.2017.23.3-b.s17.

[120] Cystic Fibrosis Foundation, 2017 Patient Registry: Annual Data Report, Bethesda, Maryl. (2018) 77. https://www.cff.org/Research/Researcher-Resources/Patient-Registry/2017-Patient-Registry-Annual-Data-Report.pdf.

[121] A.S. Cross Vogel, S.E. Goldblum, W.C. Blackwelder, C. Feng, L. Zhang, C. Nguyen, Acute Lung Injury in Mice Potentiates Lipopolysaccharide-Induced Neuraminidase Reprograms Lung Tissue and, (2013). doi:10.4049/jimmunol.1202673.

[122] C.S. Hahn, D.W. Scott, X. Xu, M.A. Roda, G.A. Payne, J.M. Wells, L. Viera, C.J. Winstead, P. Bratcher, R.W. Sparidans, F.A. Redegeld, P.L. Jackson, G. Folkerts, J.E. Blalock, R.P. Patel, A. Gaggar, The matrikine N-α-PGP couples extracellular matrix fragmentation to endothelial permeability, Sci. Adv. 1 (2015). doi:10.1126/sciadv.1500175.

[123] P.J. Schweiger, K.B. Jensen, Modeling human disease using organotypic cultures, Curr. Opin. Cell Biol. 43 (2016) 22–29. doi:10.1016/j.ceb.2016.07.003.

[124] J.M.S. Sucre, D. Wilkinson, P. Vijayaraj, M.K. Paul, B. Dunn, J.A. Alva-Ornelas, B.N. Gomperts, A 3-Dimensional Human Model of the Fibroblast Activation that Accompanies Bronchopulmonary Dysplasia Identifies Notch-Mediated Pathophysiology., Am. J. Physiol. Lung Cell. Mol. Physiol. (2016) ajplung.00446.2015. doi:10.1152/ajplung.00446.2015.

[125] D.C. Wilkinson, J.A. Alva-Ornelas, J.M.S. Sucre, P. Vijayaraj, A. Durra, W. Richardson, S.J. Jonas, M.K. Paul, S. Karumbayaram, B. Dunn, B.N. Gomperts, Development of a Three-Dimensional Bioengineering Technology to Generate

Lung Tissue for Personalized Disease Modeling, Stem Cells Transl. Med. 6 (2017) 622–633. doi:10.5966/sctm.2016-0192.

[126] B.L.M.H. Christina E. Barkauskas, Mei-I Chung, Bryan Fioret, Xia Gao, Hiroaki Katsura, Lung organoids: current uses and future promise, Development. 144 (2017) 986–997. doi:doi: 10.1242/dev.140103.

[127] M.Z. Nikolić, E.L. Rawlins, Lung Organoids and Their Use To Study Cell-Cell Interaction, Curr. Pathobiol. Rep. 5 (2017) 223–231. doi:10.1007/s40139-017-0137-7.

[128] A. Sundarakrishnan, Y. Chen, L.D. Black, B.B. Aldridge, D.L. Kaplan, Engineered cell and tissue models of pulmonary fibrosis, Adv. Drug Deliv. Rev. 129 (2018) 78–94. doi:10.1016/J.ADDR.2017.12.013.

[129] Y.-W. Chen, S.X. Huang, A.L.R.T. de Carvalho, S.-H. Ho, M.N. Islam, S. Volpi, L.D. Notarangelo, M. Ciancanelli, J.-L. Casanova, J. Bhattacharya, A.F. Liang, L.M. Palermo, M. Porotto, A. Moscona, H.-W. Snoeck, A three-dimensional model of human lung development and disease from pluripotent stem cells, Nat. Cell Biol. 19 (2017) 542–549. doi:10.1038/ncb3510.

[130] O.A. Forrest, S.A. Ingersoll, M.K. Preininger, J. Laval, D.H. Limoli, M.R. Brown, F.E. Lee, B. Bedi, R.T. Sadikot, J.B. Goldberg, V. Tangpricha, A. Gaggar, R. Tirouvanziam, Frontline Science: Pathological conditioning of human neutrophils recruited to the airway milieu in cystic fibrosis, J. Leukoc. Biol. 104 (2018) 665–675. doi:doi:10.1002/JLB.5HI1117-454RR.

[131] A. Jain, R. Barrile, A. van der Meer, A. Mammoto, T. Mammoto, K. De Ceunynck, O. Aisiku, M. Otieno, C. Louden, G. Hamilton, R. Flaumenhaft, D. Ingber, Primary Human Lung Alveolus-on-a-chip Model of Intravascular Thrombosis for Assessment of Therapeutics, Clin. Pharmacol. Ther. 103 (2018) 332–340. doi:10.1002/cpt.742.

[132] K.H. Benam, R. Villenave, C. Lucchesi, A. Varone, C. Hubeau, H.-H. Lee, S.E. Alves, M. Salmon, T.C. Ferrante, J.C. Weaver, A. Bahinski, G.A. Hamilton, D.E. Ingber, Small airway-on-a-chip enables analysis of human lung inflammation and drug responses in vitro, Nat Meth. 13 (2016) 151–157. http://dx.doi.org/10.1038/nmeth.3697.

[133] K.H. Benam, R. Novak, J. Nawroth, M. Hirano-Kobayashi, T.C. Ferrante, Y. Choe, R. Prantil-Baun, J.C. Weaver, A. Bahinski, K.K. Parker, D.E. Ingber, Matched-Comparative Modeling of Normal and Diseased Human Airway Responses Using a Microengineered Breathing Lung Chip, Cell Syst. 3 (2017) 456–466.e4. doi:10.1016/j.cels.2016.10.003.

[134] M. Humayun, C.-W. Chow, E.W.K. Young, Microfluidic lung airway-on-a-chip with arrayable suspended gels for studying epithelial and smooth muscle cell interactions, Lab Chip. 18 (2018) 1298–1309. doi:10.1039/C7LC01357D.

[135] M.M. Silva, R. Calado, J. Marto, A. Bettencourt, A.J. Almeida, L.M.D. Gonçalves, Chitosan Nanoparticles as a Mucoadhesive Drug Delivery System for Ocular Administration., Mar. Drugs. 15 (2017). doi:10.3390/md15120370.

[136] M.-C. Chen, F.-L. Mi, Z.-X. Liao, C.-W. Hsiao, K. Sonaje, M.-F. Chung, L.-W. Hsu, Recent advances in chitosan-based nanoparticles for oral delivery of macromolecules, Adv. Drug Deliv. Rev. 65 (2013) 865–879. doi:10.1016/J.ADDR.2012.10.010.

[137] L. Aragao-Santiago, H. Hillaireau, N. Grabowski, S. Mura, T.L. Nascimento, S. Dufort, J.L. Coll, N. Tsapis, E. Fattal, Compared in vivo toxicity in mice of lung delivered biodegradable and non-biodegradable nanoparticles, Nanotoxicology. 10 (2016) 292–302. doi:10.3109/17435390.2015.1054908.

[138] P.S. Pourshahab, K. Gilani, E. Moazeni, H. Eslahi, M.R. Fazeli, H. Jamalifar, Preparation and characterization of spray dried inhalable powders containing chitosan nanoparticles for pulmonary delivery of isoniazid, J. Microencapsul. 28 (2011) 605–613. doi:10.3109/02652048.2011.599437.

[139] M. Ouellette, F. Masse, M. Lefebvre-Demers, Q. Maestracci, P. Grenier, R. Millar, N. Bertrand, M. Prieto, É. Boisselier, Insights into gold nanoparticles as a mucoadhesive system, Sci. Rep. 8 (2018) 14357. doi:10.1038/s41598-018-32699-2.

[140] B. Ghosn, A.L. van de Ven, J. Tam, A. Gillenwater, K. V Sokolov, R. Richards-Kortum, K. Roy, Efficient mucosal delivery of optical contrast agents using imidazole-modified chitosan, J. Biomed. Opt. 15 (2010) 15003–15011. http://dx.doi.org/10.1117/1.3309739.

[141] B. Ghosn, A. Singh, M. Li, A. V Vlassov, C. Burnett, N. Puri, K. Roy, Efficient gene silencing in lungs and liver using imidazole-modified chitosan as a nanocarrier for small interfering RNA, Oligonucleotides. 20 (2010) 163–172. doi:10.1089/oli.2010.0235.

[142] J. Zabner, P. Karp, M. Seiler, S.L. Phillips, C.J. Mitchell, M. Saavedra, M. Welsh, A.J. Klingelhutz, Development of cystic fibrosis and noncystic fibrosis airway cell lines, Am. J. Physiol. - Lung Cell. Mol. Physiol. 284 (2003) L844 LP-L854. doi:10.1152/ajplung.00355.2002.

[143] C. Cooksley, E. Roscioli, P.J. Wormald, S. Vreugde, TLR response pathways in NuLi-1 cells and primary human nasal epithelial cells, Mol. Immunol. 68 (2015) 476–483. doi:10.1016/j.molimm.2015.09.024.

[144] M. Hasegawa, A. Isogai, F. Onabe, Preparation of low-molecular-weight chitosan using phosphoric acid, Carbohydr. Polym. 20 (1993) 279–283. doi:10.1016/0144-8617(93)90100-I.

[145] J. Li, Y. Du, J. Yang, T. Feng, A. Li, P. Chen, Preparation and characterisation of low molecular weight chitosan and chito-oligomers by a commercial enzyme, Polym. Degrad. Stab. 87 (2005) 441–448. doi:10.1016/J.POLYMDEGRADSTAB.2004.09.008.

[146] Z. Jia, D. Shen, Effect of reaction temperature and reaction time on the preparation of low-molecular-weight chitosan using phosphoric acid, Carbohydr. Polym. 49 (2002) 393–396. doi:10.1016/S0144-8617(02)00026-7.

[147] S.-B. Lin, Y.-C. Lin, H.-H. Chen, Low molecular weight chitosan prepared with the aid of cellulase, lysozyme and chitinase: Characterisation and antibacterial activity, Food Chem. 116 (2009) 47–53. doi:10.1016/J.FOODCHEM.2009.02.002.

[148] K. Hoenderdos, A. Condliffe, The Neutrophil in Chronic Obstructive Pulmonary Disease. Too Little, Too Late or Too Much, Too Soon?, Am. J. Respir. Cell Mol. Biol. 48 (2013) 531–539. doi:10.1165/rcmb.2012-0492TR.

[149] L. Meijer, D.J. Nelson, V. Riazanski, A.G. Gabdoulkhakova, G. Hery-Arnaud, R. Le Berre, N. Loaëc, N. Oumata, H. Galons, E. Nowak, L. Gueganton, G. Dorothée, M. Prochazkova, B. Hall, A.B. Kulkarni, R.D. Gray, A.G. Rossi, V. Witko-Sarsat, C. Norez, F. Becq, D. Ravel, D. Mottier, G. Rault, Modulating Innate and Adaptive Immunity by (R)-Roscovitine: Potential Therapeutic Opportunity in Cystic Fibrosis., J. Innate Immun. 8 (2016) 330–49. doi:10.1159/000444256.

[150] S. Moriceau, G. Lenoir, V. Witko-Sarsat, In cystic fibrosis homozygotes and heterozygotes, neutrophil apoptosis is delayed and modulated by diamide or roscovitine: Evidence for an innate neutrophil disturbance, J. Innate Immun. 2 (2010) 260–266. doi:10.1159/000295791.

[151] H. Tang, H. He, H. Ji, L. Gao, J. Mao, J. Liu, H. Lin, T. Wu, Tanshinone IIA ameliorates bleomycin-induced pulmonary fibrosis and inhibits transforming growth factor-beta-β–dependent epithelial to mesenchymal transition, J. Surg. Res. 197 (2015) 167–175. doi:10.1016/J.JSS.2015.02.062.

[152] M. Xu, F. Cao, Y. Zhang, L. Shan, X. Jiang, X. An, W. Xu, X. Liu, X. Wang, Tanshinone IIA therapeutically reduces LPS-induced acute lung injury by

inhibiting inflammation and apoptosis in mice, Acta Pharmacol. Sin. 36 (2015) 179–187. doi:10.1038/aps.2014.112.

[153] J.L. Johnson, M. Ramadass, J. He, S.J. Brown, J. Zhang, L. Abgaryan, N. Biris, E. Gavathiotis, H. Rosen, S.D. Catz, Identification of Neutrophil Exocytosis Inhibitors (Nexinhibs), Small Molecule Inhibitors of Neutrophil Exocytosis and Inflammation, J. Biol. Chem. 291 (2016) 25965–25982. doi:10.1074/jbc.M116.741884.

[154] K. Chung, C.A. Rivet, M.L. Kemp, H. Lu, Imaging Single-Cell Signaling Dynamics with a Deterministic High-Density Single-Cell Trap Array, Anal. Chem. 83 (2011) 7044–7052. doi:10.1021/ac2011153.

[155] T. Canal, N.A. Peppast, Correlation between mesh size and equilibrium, J. Biomed. Mater. Res. 23 (1989) 1183–1193.

[156] E.A. Phelps, N.O. Enemchukwu, V.F. Fiore, J.C. Sy, N. Murthy, T.A. Sulchek, T.H. Barker, A.J. García, Maleimide cross-linked bioactive PEG hydrogel exhibits improved reaction kinetics and cross-linking for cell encapsulation and in situ delivery, Adv. Mater. 24 (2012) 64–70. doi:10.1002/adma.201103574.

[157] M.C. Ferrall-Fairbanks, Z.T. Barry, M. Affer, M.A. Shuler, E.W. Moomaw, M.O. Platt, PACMANS: A bioinformatically informed algorithm to predict, design, and disrupt protease-on-protease hydrolysis, Protein Sci. 26 (2017) 880–890. doi:10.1002/pro.3113.

[158] J.A. Champion, A. Walker, S. Mitragotri, Role of Particle Size in Phagocytosis of Polymeric Microspheres, Pharm. Res. 25 (2008) 1815–1821. doi:10.1007/s11095-008-9562-y.

[159] A.C. Anselmo, S. Mitragotri, Impact of particle elasticity on particle-based drug delivery systems, Adv. Drug Deliv. Rev. 108 (2017) 51–67. doi:10.1016/J.ADDR.2016.01.007.

[160] A. Gaggar, A. Hector, P.E. Bratcher, M.A. Mall, M. Griese, D. Hartl, The role of matrix metalloproteinases in cystic fibrosis lung disease., Eur. Respir. J. Off. J. Eur. Soc. Clin. Respir. Physiol. 38 (2011) 721–727. doi:10.1183/09031936.00173210.

[161] L.W. Garratt, E.N. Sutanto, K.-M. Ling, K. Looi, T. Iosifidis, K.M. Martinovich, N.C. Shaw, E. Kicic-Starcevich, D.A. Knight, S. Ranganathan, S.M. Stick, A. Kicic, Matrix metalloproteinase activation by free neutrophil elastase contributes to bronchiectasis progression in early cystic fibrosis, Eur Respir J. 46 (2015) 384–394. doi:10.1183/09031936.00212114.

[162] H.L. Wright, R.J. Moots, S.W. Edwards, The multifactorial role of neutrophils in rheumatoid arthritis, Nat Rev Rheumatol. 10 (2014) 593–601. doi:10.1038/nrrheum.2014.80.

[163] M.J. Kaplan, Neutrophils in the pathogenesis and manifestations of SLE, Nat Rev Rheumatol. 7 (2011) 691–699. doi:10.1038/nrrheum.2011.132.

[164] J. Grommes, O. Soehnlein, Contribution of neutrophils to acute lung injury, Mol Med. 17 (2011) 293–307. doi:10.2119/molmed.2010.00138.

[165] H. Gao, S. Ying, Y. Dai, Pathological Roles of Neutrophil-Mediated Inflammation in Asthma and Its Potential for Therapy as a Target, J Immunol Res. 2017 (2017) 3743048. doi:10.1155/2017/3743048.

[166] C. Margaroli, R. Tirouvanziam, Neutrophil plasticity enables the development of pathological microenvironments: implications for cystic fibrosis airway disease, Mol Cell Pediatr. 3 (2016) 38. doi:10.1186/s40348-016-0066-2.

[167] A.D. Chiara, M. Pederzoli-Ribeil, P.R. Burgel, C. Danel, V. Witko-Sarsat, Targeting cytosolic proliferating cell nuclear antigen in neutrophil-dominated inflammation, Front Immunol. 3 (2012) 311. doi:10.3389/fimmu.2012.00311.

[168] S. Moriceau, C. Kantari, J. Mocek, N. Davezac, J. Gabillet, I.C. Guerrera, F. Brouillard, D. Tondelier, I. Sermet-Gaudelus, C. Danel, G. Lenoir, S. Daniel, A. Edelman, V. Witko-Sarsat, Coronin-1 is associated with neutrophil survival and is cleaved during apoptosis: potential implication in neutrophils from cystic fibrosis patients, J Immunol. 182 (2009) 7254–7263. doi:10.4049/jimmunol.0803312.

[169] A. Mocsai, Diverse novel functions of neutrophils in immunity, inflammation, and beyond, J Exp Med. 210 (2013) 1283–1299. doi:10.1084/jem.20122220.

[170] M. Griese, M. Kappler, A. Gaggar, D. Hartl, Inhibition of airway proteases in cystic fibrosis lung disease., Eur. Respir. J. 32 (2008) 783–95. doi:10.1183/09031936.00146807.

[171] G. Brigden, P. du Cros, S. Wong, Barriers to new drug development in respiratory disease, Eur. Respir. J. 47 (2016) 356. http://erj.ersjournals.com/content/47/1/356.abstract.

[172] J.D. Chalmers, M. Loebinger, S. Aliberti, Challenges in the development of new therapies for bronchiectasis, Expert Opin. Pharmacother. 16 (2015) 833–850. doi:10.1517/14656566.2015.1019863.

[173] B.M. Ibrahim, M.D. Tsifansky, Y. Yang, Y. Yeo, Challenges and advances in the development of inhalable drug formulations for cystic fibrosis lung disease, Expert Opin. Drug Deliv. 8 (2011) 451–466. doi:10.1517/17425247.2011.561310.

[174] J. Reutershan, A. Basit, E. V. Galkina, K. Ley, Sequential recruitment of neutrophils into lung and bronchoalveolar lavage fluid in LPS-induced acute lung injury, Am. J. Physiol. Cell. Mol. Physiol. 289 (2005) L807–L815. doi:10.1152/ajplung.00477.2004.

[175] R. Corteling, D. Wyss, A. Trifilieff, In vivo models of lung neutrophil activation. Comparison of mice and hamsters, BMC Pharmacol. 2 (2002) 1. doi:10.1186/1471-2210-2-1.

[176] A. V. Misharin, L. Morales-Nebreda, G.M. Mutlu, G.R.S. Budinger, H. Perlman, Flow cytometric analysis of macrophages and dendritic cell subsets in the mouse lung, Am. J. Respir. Cell Mol. Biol. 49 (2013) 503–510. doi:10.1165/rcmb.2013-0086MA.

[177] N. Doshi, A.S. Zahr, S. Bhaskar, J. Lahann, S. Mitragotri, Red blood cell-mimicking synthetic biomaterial particles, Proc. Natl. Acad. Sci. 106 (2009) 21495–21499. doi:10.1073/PNAS.0907127106.

[178] A.M. Fitzpatrick, F. Holguin, W.G. Teague, L.A.S. Brown, Alveolar macrophage phagocytosis is impaired in children with poorly controlled asthma, J. Allergy Clin. Immunol. 121 (2008) 1372–1378.e3. doi:10.1016/j.jaci.2008.03.008.

[179] N.E. Alexis, M.S. Muhlebach, D.B. Peden, T.L. Noah, Attenuation of host defense function of lung phagocytes in young cystic fibrosis patients., J. Cyst. Fibros. 5 (2006) 17–25. doi:10.1016/j.jcf.2005.11.001.

[180] M. Lévêque, S. Le Trionnaire, P. Del Porto, C. Martin-Chouly, The impact of impaired macrophage functions in cystic fibrosis disease progression, J. Cyst. Fibros. 16 (2017) 443–453. doi:10.1016/J.JCF.2016.10.011.

[181] Z. Liang, Q. Zhang, C.M. Thomas, K.K. Chana, D. Gibeon, P.J. Barnes, K.F. Chung, P.K. Bhavsar, L.E. Donnelly, Impaired macrophage phagocytosis of bacteria in severe asthma, Respir. Res. 15 (2014) 72. doi:10.1186/1465-9921-15-72.

[182] A.L. Robertson, G.R. Holmes, A.N. Bojarczuk, J. Burgon, C.A. Loynes, M. Chimen, A.K. Sawtell, B. Hamza, J. Willson, S.R. Walmsley, S.R. Anderson, M.C. Coles, S.N. Farrow, R. Solari, S. Jones, L.R. Prince, D. Irimia, G.E. Rainger, V. Kadirkamanathan, M.K.B. Whyte, S.A. Renshaw, A zebrafish compound screen reveals modulation of neutrophil reverse migration as an anti-inflammatory

mechanism., Sci. Transl. Med. 6 (2014) 225ra29. doi:10.1126/scitranslmed.3007672.

[183] C. Jiang, W. Zhu, X. Yan, Q. Shao, B. Xu, M. Zhang, R. Gong, Rescue therapy with Tanshinone IIA hinders transition of acute kidney injury to chronic kidney disease via targeting GSK3β, Sci. Rep. 6 (2016) 36698. doi:10.1038/srep36698.

[184] D. Li, J. Wang, D. Sun, X. Gong, H. Jiang, J. Shu, Z. Wang, Z. Long, Y. Chen, Z. Zhang, L. Yuan, R. Guan, X. Liang, Z. Li, H. Yao, N. Zhong, W. Lu, Tanshinone IIA sulfonate protects against cigarette smoke-induced COPD and down-regulation of CFTR in mice, Sci. Rep. 8 (2018) 376. doi:10.1038/s41598-017-18745-5.

[185] K.R. Genschmer, D.W. Russell, C. Lal, T. Szul, P.E. Bratcher, B.D. Noerager, M. Abdul Roda, X. Xu, G. Rezonzew, L. Viera, B.S. Dobosh, C. Margaroli, T.H. Abdalla, R.W. King, C.M. McNicholas, J.M. Wells, M.T. Dransfield, R. Tirouvanziam, A. Gaggar, J.E. Blalock, Activated PMN Exosomes: Pathogenic Entities Causing Matrix Destruction and Disease in the Lung, Cell. 176 (2019) 113–126.e15. doi:10.1016/j.cell.2018.12.002.

[186] M.B. Chen, J.A. Whisler, J. Fröse, C. Yu, Y. Shin, R.D. Kamm, On-chip human microvasculature assay for visualization and quantification of tumor cell extravasation dynamics, Nat. Protoc. (2017). doi:10.1038/nprot.2017.018.

[187] S. Kim, H. Lee, M. Chung, N.L. Jeon, Engineering of functional, perfusable 3D microvascular networks on a chip, Lab Chip. 13 (2013) 1489. doi:10.1039/c3lc41320a.

[188] S. Kim, W. Kim, S. Lim, J.S. Jeon, Vasculature-On-A-Chip for In Vitro Disease Models., Bioeng. (Basel, Switzerland). 4 (2017). doi:10.3390/bioengineering4010008.

[189] S. Oh, H. Ryu, D. Tahk, J. Ko, Y. Chung, H.K. Lee, T.R. Lee, N.L. Jeon, "Open-top" microfluidic device for in vitro three-dimensional capillary beds, Lab Chip. 17 (2017) 3405–3414. doi:10.1039/C7LC00646B.

[190] M.J. Mondrinos, Y.-S. Yi, N.-K. Wu, X. Ding, D. Huh, Native extracellular matrix-derived semipermeable, optically transparent, and inexpensive membrane inserts for microfluidic cell culture, Lab Chip. (2017). doi:10.1039/C7LC00317J.

[191] S. Prasad, C.M. Hogaboam, G. Jarai, Deficient repair response of IPF fibroblasts in a co-culture model of epithelial injury and repair., Fibrogenesis Tissue Repair. 7 (2014) 7. doi:10.1186/1755-1536-7-7.

[192] M.J. Schafer, T.A. White, K. Iijima, A.J. Haak, G. Ligresti, E.J. Atkinson, A.L. Oberg, J. Birch, H. Salmonowicz, Y. Zhu, D.L. Mazula, R.W. Brooks, H. Fuhrmann-Stroissnigg, T. Pirtskhalava, Y.S. Prakash, T. Tchkonia, P.D. Robbins, M.C. Aubry, J.F. Passos, J.L. Kirkland, D.J. Tschumperlin, H. Kita, N.K. LeBrasseur, Cellular senescence mediates fibrotic pulmonary disease, Nat. Commun. 8 (2017) 14532. doi:10.1038/ncomms14532.

[193] D.W. Waters, K.E.C. Blokland, P.S. Pathinayake, J.K. Burgess, S.E. Mutsaers, C.M. Prele, M. Schuliga, C.L. Grainge, D.A. Knight, Fibroblast senescence in the pathology of idiopathic pulmonary fibrosis, Am. J. Physiol. Cell. Mol. Physiol. 315 (2018) L162–L172. doi:10.1152/ajplung.00037.2018.

[194] K. Aran, L.A. Sasso, N. Kamdar, J.D. Zahn, Irreversible, direct bonding of nanoporous polymer membranes to PDMS or glass microdevices, Lab Chip. 10 (2010) 548. doi:10.1039/b924816a.

[195] D.T.T. Phan, X. Wang, B.M. Craver, A. Sobrino, D. Zhao, J.C. Chen, L.Y.N. Lee, S.C. George, A.P. Lee, C.C.W. Hughes, A vascularized and perfused organ-on-a-chip platform for large-scale drug screening applications, Lab Chip. 17 (2017). doi:10.1039/C6LC01422D.

[196] J.A. Rytlewski, M.A. Aldon, E.W. Lewis, L.J. Suggs, Mechanisms of Tubulogenesis and Endothelial Phenotype Expression by MSCs, Microvasc. Res. 99 (2015) 26. doi:10.1016/J.MVR.2015.02.005.

[197] O.M. Benavides, J.P. Quinn, S. Pok, J. Petsche Connell, R. Ruano, J.G. Jacot, Capillary-Like Network Formation by Human Amniotic Fluid-Derived Stem Cells Within Fibrin/Poly(Ethylene Glycol) Hydrogels, Tissue Eng. Part A. 21 (2015) 1185–1194. doi:10.1089/ten.tea.2014.0288.

[198] C.A. Schneider, W.S. Rasband, K.W. Eliceiri, NIH Image to ImageJ: 25 years of image analysis., Nat. Methods. 9 (2012) 671–5. http://www.ncbi.nlm.nih.gov/pubmed/22930834.

[199] A.Y. Rioja, R. Tiruvannamalai Annamalai, S. Paris, A.J. Putnam, J.P. Stegemann, Endothelial sprouting and network formation in collagen- and fibrin-based modular microbeads., Acta Biomater. 29 (2016) 33–41. doi:10.1016/j.actbio.2015.10.022.

[200] B. Hinz, G. Celetta, J.J. Tomasek, G. Gabbiani, C. Chaponnier, Alpha-smooth muscle actin expression upregulates fibroblast contractile activity., Mol. Biol. Cell. 12 (2001) 2730–41. doi:10.1091/mbc.12.9.2730.

[201] B. Li, J.H.-C. Wang, Fibroblasts and myofibroblasts in wound healing: force generation and measurement., J. Tissue Viability. 20 (2011) 108–20. doi:10.1016/j.jtv.2009.11.004.

[202] M. Asmani, S. Velumani, Y. Li, N. Wawrzyniak, Z. Chen, B. Hinz, R. Zhao, I. Hsia, Z. Chen, B. Hinz, R. Zhao, Fibrotic microtissue array to predict anti-fibrosis drug efficacy, Nat. Commun. 9 (2018). doi:10.1038/s41467-018-04336-z.

[203] E. Amstad, S.S. Datta, D.A. Weitz, The microfluidic post-array device: high throughput production of single emulsion drops, Lab Chip. 14 (2014) 705–709. doi:10.1039/C3LC51213D.